UNIVERSITÉ DE STRASBOURG

ÉCOLE DOCTORALE DE PHYSIQUE ET CHIMIE-PHYSIQUE

Thèse présentée par :
Tuerhong ROUZHAJI

Soutenue le 05 Juillet 2017

POUR OBTENIR LE GRADE DE :

Docteur de l'université de Strasbourg

Discipline : Physique

Effect of the environment on the electronic and magnetic properties of transition metals and rare-earth complexes

Membres du Jury :

Prof. Jean-Pierre Bucher	**Directeur de thèse**
Prof. Mathieu Abel	**Rapporteur externe**
Dr. Joachim Bansmann	**Rapporteur externe**
Prof. Mebarek Alouani	**Examinateur interne**

**Institut de Physique et Chimie des Matériaux de Strasbourg,
UMR 7504, France**

Résumé

L'histoire de la technologie des semi-conducteurs montre que les semiconducteurs traditionnels ont été et sont encore largement utilisés dans une grande variété de dispositifs microélectroniques. Bien que leur miniaturisation représente un défi technologique pour la production à grande échelle, elle approche les limites physiques de la technologie des semiconducteurs. Une solution alternative possible pour surmonter ces limites est l'utilisation de molécules semi-conductrices organiques comme des composants électroniques simples dans la technologie future en raison de leurs fonctionnalités uniques ainsi que de leur petite taille intrinsèque (~ nm). En outre, les molécules organiques offrent plusieurs avantages, comme un traitement simple et peu coûteux, la possibilité d'une modification chimique et la capacité d'auto-assemblage en structures fonctionnelles ordonnées. Par conséquent, les molécules semi-conductrices organiques attirent de plus en plus d'intérêt dans la recherche en nanosciences pour leurs applications technologiques potentielles dans les futurs appareils électroniques moléculaires [1-2] et spintroniques [3-4].

Les phtalocyanines métalliques représentent une classe bien connue de molécules avec des propriétés semi-conductrices organiques à l'état massif et sont déjà utilisées dans des applications industrielles comprenant des transistors à effet de champ, des détecteurs de gaz et des cellules solaires [5]. La molécule de phtalocyanine métallique dénommée MPc de son appellation anglaise « Metal-phthalocyanine » se compose d'un anneau de phtalocyanine (Pc) qui entoure un ion métallique (M) en son centre (voir la figure 1). Ces molécules sont caractérisées par une structure moléculaire assez simple et stable avec la symétrie planaire carrée D_{4h}.

- ● Metal
- ● Nitrogen
- ● Carbon
- ● Hydrogen

Figure 1 Structure schématique de la molécule de phtalocyanine métallique. L'atome de métal central (rouge) réside dans un environnement de symétrie D_{4h}.

Récemment, les molécules de MPc ont suscité un grand intérêt de recherche en raison de la configuration de bande interdite modulable et de la configuration de spin selon les espèces chimiques de l'ion métallique central. En outre, leur structure relativement simple et robuste en fait un système modèle pour étudier l'interaction des complexes métal-organique avec les surfaces métalliques. Ces fonctionnalités intéressantes des molécules MPc en font des candidats prometteurs pour les applications potentielles dans les futurs appareils électroniques à base de molécules [6-7].

 Pour de nombreuses applications technologiques, il est nécessaire de contacter la molécule MPc avec des électrodes métalliques ou de les placer sur des substrats (voir la figure 2). Cependant, de nombreuses propriétés moléculaires intéressantes et utiles, exhibées par ces molécules dans leur état massif, peuvent, une fois en solution ou en phase gazeuse, être détruites ou fortement modifiées du fait de l'interaction de ces molécules avec le substrat ainsi qu'avec les molécules voisines. Cependant, de nouvelles propriétés peuvent émerger de ces interactions. Par conséquent, l'utilisation possible de molécules MPc comme unités fonctionnelles individuelles ou une structure fonctionnelle auto-assemblée ordonnée dans les dispositifs électroniques organiques dépend crucialement de la compréhension et du contrôle de l'interaction de la molécule avec le substrat ainsi que de l'interaction entre les molécules elles-mêmes.
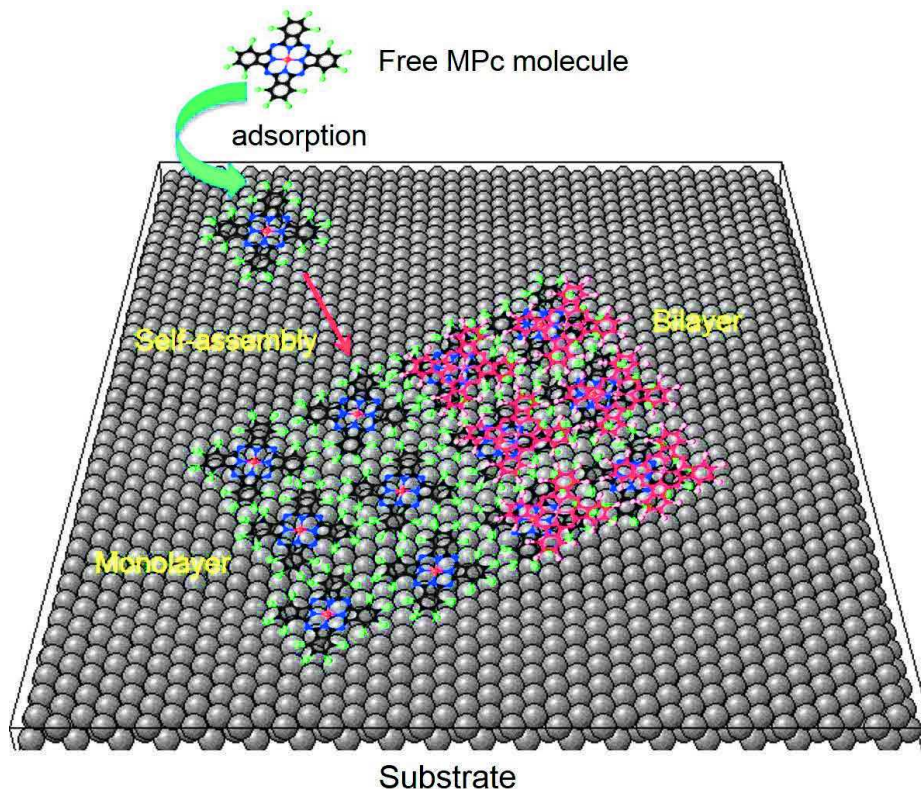

Figure 2 Dessin schématique des processus favorables à la croissance auto-assemblée de la mono et bi-couche de molécules MPc sur le substrat.

L'invention de la microscopie à effet tunnel (STM) [8-9] a permis d'étudier la matière à l'échelle nanométrique et même atomique. Depuis lors, le STM est devenu un outil puissant pour l'étude et le contrôle des propriétés physiques des atomes et molécules uniques, ainsi que leur interaction avec le substrat et avec d'autres molécules voisines. En particulier, les mesures STM à basse température nous permettent de combiner les capacités d'imagerie haute résolution spatiale du STM avec l'analyse spectroscopique à haute résolution énergétique, avec la manipulation locale et les modifications chimiques sur la molécule unique ou une couche moléculaire auto-assemblée à la surface. Cela offre la possibilité de lever le voile sur les processus en surface et de fournir une base pour la compréhension de la physique à l'interface molécule-métal.

L'étude STM des molécules MPc sur surface métallique a commencé dans les années 1987 [10]. Depuis lors, une grande variété de molécules MPc adsorbées sur des surfaces a été étudiée par STM [11-17] et d'autres techniques sensibles à la surface [18-21] et par des calculs de la théorie fonctionnelle de densité (DFT) [22-25]. La plupart des recherches sur les molécules de MPc se sont concentrées sur les phtalocyanines de manganèse (MnPc) [25-26], de fer (FePc) [14, 27] et de cobalt (CoPc) [17-18, 23-24] pour lesquelles Il a été montré que l'adsorption sur une surface métallique tend à réduire ou à totalement annihiler le moment magnétique moléculaire intrinsèque induit par les électrons non appariés résidant dans la couche électronique 3d de l'ion du métal transition central.

Dans les études STM sur les molécules MPc adsorbées sur les surfaces, une attention particulière a été accordée à une compréhension approfondie de l'interaction des molécules MPc avec les surfaces métalliques, des propriétés électroniques et de la densité des états près du niveau de Fermi. L'effet Kondo en particulier a été intensément étudié récemment. L'effet de Kondo est un écrantage cohérent du moment magnétique de spin des impuretés par les électrons de conduction de l'hôte métallique. Cet écrantage conduit à la formation d'un état singlet à 'plusieurs corps' et donne ainsi naissance à un état de résonance proche du niveau de Fermi dans le spectre énergétique du système.

L'effet Kondo étant une signature caractéristique de l'impureté magnétique dans un hôte métallique non magnétique, il fournit une méthode prometteuse pour sonder par STM le moment magnétique local de la molécule adsorbée sur une surface métallique. Dans les expériences STM, l'effet Kondo est détecté comme un état de résonance bien marqué au niveau de Fermi. En sondant l'effet Kondo dans la molécule MPc par STM avec une résolution spatiale/énergétique élevée, l'influence de l'interaction molécule-substrat sur les propriétés magnétiques des molécules MPc a été étudié dans une grande variété de systèmes MPc/substrats-métallique. Ainsi, un certain nombre résultats expérimentaux fascinantes ont été présentés. Sur un substrat d'Au (111), les molécules MnPc et FePc présentent tous deux une résonance Kondo des centres métalliques de Mn et Fe 3d respectivement [28-30]. Par contre, l'effet Kondo est absent sur le centre métallique de Co dans le cas du CoPc malgré son adsorption sur le même substrat Au (111) [31]. De plus, ni FePc ni CoPc sur Ag (100) ne présentent la résonance de Kondo sur leurs ions métalliques 3d centraux [32], alors qu'un pic Kondo très marqué est observé sur l'ion Mn de MnPc sur une surface Ag (100) [33]. Les comportements de Kondo des molécules

MnPc, FePc et CoPc sur Au (111) par rapport à celle du substrat Ag (100) impliquent que l'occupation des orbitales d de l'ion de métal de transition central semble un facteur important qui détermine l'état de rotation de la Molécule MPc adsorbée sur une surface métallique, et donc de la formation de l'interaction Kondo entre la molécule MPc et l'hôte métallique. Parmi les molécules de MPc étudiées, la molécule de MnPc présente la résonance de Kondo sur son site ionique central de Mn lorsqu'elle est adsorbée sur de nombreuses surfaces de métal noble telles que : Au (111) [28], Ag (100) [33] et Pb (111) [26]. En revanche, la molécule FePc montre une résonance Kondo uniquement lorsqu'elle est adsorbée sur la surface Au (111) [30]. La molécule de CoPc par contre, ne présente de résonance Kondo sur aucun de ces substrats métalliques. Les comportements de Kondo observés sur l'ion métallique central des molécules MnPc, FePc et CoPc sur les surfaces métalliques nous donnent l'indication que l'état de spin de la molécule MPc adsorbée est déterminé non seulement par l'occupation des orbitales d de l'ion métallique central mais aussi par les interactions molécule-substrat.

 De plus, une étude STM récente sur les molécules CuPc et NiPc adsorbées sur Ag (100) a mis en évidence la possibilité d'induire un moment magnétique délocalisé sur le ligand organique Pc. Ceci affecte la dégénérescence de spin et la symétrie de l'état fondamental moléculaire ainsi que la conductance électrique mesurée à différents endroits de la molécule [34]. En outre, Minamitani et al [35] ont également signalé un résultat expérimental très intéressant pour la molécule de MnPc adsorbée sur le substrat Pb (111). Ils ont montré que la résonance Kondo dans le système MnPc/Pb (111) est non seulement localisée sur l'ion Mn central, mais s'étend également sur le cycle pyrrole dans le ligand Pc. Ils ont conclu qu'un état de spin unique induit par la forte interaction π-d est responsable de l'extension spatiale de l'effet Kondo.

 En outre, Chen et ses collaborateurs [36] ont observé que les spectres dI/dV des super-réseaux moléculaires CoPc multicouches formés sur les îlots Pb (111) dépendent fortement du nombre de couches d'empilage. En particulier, ni la séparation Zeeman ni la résonance de Kondo n'ont été observées pour la monocouche de CoPc, ce qui suggère que le moment magnétique des molécules de CoPc dans la première couche est complètement étouffé par l'adsorption directe sur la surface métallique grâce à une forte interaction de la molécule de CoPc avec la Substrat Pb. En revanche, le super-réseau CoPc bi-couche présente des pics de résonance Kondo proéminents dans les spectres dI/dV mesurés, et le composite tri-couche présente un pic sous forme de marche dans les spectres dI/dV en l'absence de champ magnétique externe. Cette dernière caractéristique a été attribuée à l'excitation de transition de spin d'un état fondamental singlet à un état excité triplet dans les systèmes moléculaires CoPc multicouches.

 En résumé, les précédentes études STM nous fournissent des informations utiles pour comprendre le magnétisme du MPc adsorbé sur des surfaces métalliques. Il est évident que la structure magnétique des molécules de MPc est profondément modifiée par l'interaction avec des substrats métalliques [28-35]. Même si le moment magnétique localisé sur l'ion métal 3d central est protégé par les ligands organiques, il peut être sévèrement réduit ou absent dans les molécules potentiellement magnétiques.

Inversement, un moment magnétique supplémentaire peut être induit sur les ligands organiques non magnétiques à travers les interactions molécules-substrat. Il est évident que la molécule MPc doit être considérée comme un système entier, c'est-à-dire l'ion métallique central, le ligand organique, les molécules voisines les plus proches et le substrat sous-jacent, pour comprendre la structure magnétique complète de la molécule adsorbée.

Les études STM antérieures sur l'effet Kondo de MPc se limitent jusqu'à présent aux molécules en surface fortement couplées au substrat métallique. A l'exception d'un seul travail [36], aucune étude STM systématique pour les molécules MPc fortement découplées du substrat n'a été effectuée. D'autre part, bien que le magnétisme des molécules MPc adsorbées sur des surfaces métalliques soit relativement bien étudié en termes d'effet Kondo, de nombreuses questions concernant l'influence de l'interaction molécule-substrat ainsi que l'interaction entre les molécules voisines sur les propriétés électroniques et magnétiques des molécules MPc dans les multicouches restent ouvertes. Ainsi, les recherches plus systématiques et approfondies sont nécessaires pour déterminer l'influence des interactions molécule-substrat et molécule-molécule sur la structure électronique et magnétique des molécules. En particulier la façon dont le découplage molécule-substrat et, à son tour, le couplage moléculaire-moléculaire affectent le magnétisme des molécules de MPc dans la structure multicouche? Ici, le problème le plus important est de comprendre la façon dont le couplage magnétique intermoléculaire influence le comportement Kondo des molécules dans une structure multicouches, où un grand intérêt est le couplage magnétique entre les moments de spin moléculaire. Un problème supplémentaire est l'interaction entre le champ magnétique externe et la molécule MPc. En particulier, le couplage magnétique entre une molécule unique de MPc et un atome magnétique supplémentaire doit être établi dans un seul environnement moléculaire.

Cette thèse présente les résultats de mesures expérimentales effectuées à basse température par les techniques de microscopie tunnel à balayage et de la spectroscopie par tunnel à balayage (STS) sur les molécules de MPc déposées sur les surfaces de métaux nobles. Les mesures STM/STS ont été effectuées pour les molécules MnPc et CuPc adsorbées sur les surfaces Ag (111) et Au (111) à la température expérimentale de travail de 4,5 K. Ces deux types de molécules présentent une différence substantielle de configuration d'adsorption, des comportements électroniques et magnétiques et de structure vibrationnelle. Les études STM/STS ont principalement porté sur les propriétés magnétiques de ces molécules et une attention particulière a été accordée à la molécule de MnPc en raison de son comportement magnétique plus intéressant issu de l'atome Mn central. En particulier, nous avons étudié l'évolution spectrale des structures électroniques et magnétiques du MnPc partant d'une molécule unique jusqu'à la structure bicouche ordonnée sur la surface Ag (111). En outre, les études STM/STS ont montré une preuve de couplage magnétique entre les moments magnétiques de l'atome de Co et de la molécule de MnPc ainsi que sa forte dépendance vis-à-vis du site d'adsorption de l'atome de Co. Ces études STM/STS sur ce système nous ont permis de comprendre l'effet des

interactions molécule-substrat, molécule-molécule et molécule-atome sur les propriétés électroniques et magnétiques des molécules de MnPc.

 Dans la première partie de ce travail de thèse, nous avons étudié les configurations d'adsorption, les propriétés électroniques et magnétiques des molécules MnPc et CuPc co-adsorbées sur Ag (111) au moyen des mesures STM/STS à haute résolution spatiale/énergie. Nous avons montré que les molécules de MnPc et de CuPc apparaissaient comme des motifs à quatre lobes dans l'image STM, mais avec une hauteur apparente distincte dans les centres moléculaires : MnPc présente un spot brillant au centre, alors qu'une petite dépression est observée pour la molécule CuPc (voir la Figure 3 (a) et (b)). Nous avons montré l'image STM de la résolution atomique de la surface Ag (111) avec le MnPc adsorbé ainsi que les molécules CuPc (voir la Figure 3 (c) et (d)) et déterminé la configuration d'adsorption exacte de ces molécules par des mesures STM indépendamment des résultats de calcul théoriques.
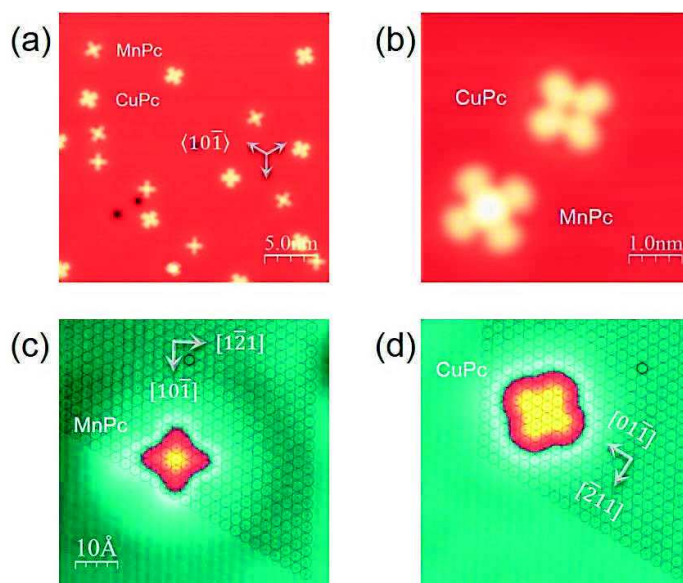

Figure 3 (a) Image STM des molécules de MnPc et CuPc co-déposées sur la surface Ag (111). L'un des axes moléculaires est aligné avec la direction de symétrie haute direction ⟨10$\bar{1}$⟩ du substrat sous-jacent. (b) l'image STM haute résolution de la molécule MnPc et CuPc sur la surface Ag (111). Image STM de résolution atomique de surface d'Ag (111) après adsorption de (c) MnPc et (d) molécules de CuPc. Les cercles représentent un réseau bidimensionnel superposé sur le réseau de substrat.

Nous avons constaté que les deux types de molécules s'adsorbent avec le plan moléculaire parallèle à la surface et les axes moléculaires sont alignés selon les directions de surface [10$\bar{1}$] et [1$\bar{2}$1] du substrat Ag (111) (voir la figure 3). En particulier, l'image STM à résolution atomique nous a permis de déterminer que l'ion Mn central est situé sur un site 'on-top' de la surface d'argent, tandis que l'ion Cu de CuPc est situé sur un site 'hollow' de la surface Ag (111). La configuration d'adsorption de MnPc sur Ag (111) observée expérimentalement a aussi été vérifiée par les calculs de la théorie de la densité fonctionnelle (DFT).

Par l'usage de STS, nous avons étudié la structure électronique des molécules MnPc et CuPc adsorbées sur la surface Ag (111). Les mesures de spectroscopie tunnel pour ces molécules directement adsorbées sur Ag (111) indiquent que la structure électronique des molécules de MnPc et CuPc est fortement influencée par l'interaction avec le substrat. Par contre, dans les spectres STS des films bicouches des molécules MnPc sur la surface Ag(111), cependant, les différentes structures électroniques caractéristiques ont été identifiées comme provenant de l'orbital moléculaire occupée la plus élevée/l'orbital moléculaire inoccupée la plus basse (HOMO/LUMO) et une orbitale moléculaire individuelle occupé (SOMO) en raison de l'hybridation des orbitales Mn 3d avec les orbitales π du ligand dans la molécule de MnPc.

Nous avons mis l'accent sur la recherche des propriétés magnétiques des molécules de MnPc et CuPc sur les surfaces métalliques au moyen de l'effet Kondo. Il fournit une preuve directe de l'existence d'un moment magnétique examiné par un nuage d'électrons itinérants du substrat. Nous avons observé l'effet de Kondo sur la molécule de MnPc adsorbée sur les surfaces Ag (111) et Au (111) avec la température Kondo de $T_K = 160 \pm 10$ K et 80 ± 10 K respectivement, et s'étendant spatialement du centre Mn au ligand Pc. Par contre, dans le système CuPc/Ag (111), la résonance Kondo a été observée sur les ligands Pc de la molécule avec la température Kondo $T_K = 45 \pm 5$ K. Nous avons également démontré que la résonance Kondo dans CuPc pourrait être désactivée/activée en déplaçant la molécule d'une/vers marche monatomique avec une pointe STM. En conclusion des, on peut affirmer que la contribution au magnétisme dans les molécules de phtalocyanine métallique provient non seulement des spins localisés dans les orbitales 3d du métal, mais aussi du spin délocalisé dans l'orbitale π du ligand organique. En outre, nous avons constaté que la présence des moments magnétiques dans le ligand Pc organique et sur l'ion Cu de la molécule de CuPc conduit à un état fondamental triplet, en raison du couplage d'échange intra-moléculaire entre le spin-π et le spin-d. Le déplacement tunnel inélastique d'un électron de la pointe STM au substrat à travers une molécule CuPc induit une excitation de cette dernière de l'état fondamental triplet à l'état excité d'un singlet, comme en témoignent les deux pics latéraux positionnés à des tensions fines. En résumé, nous avons étudié la physique complexe de Kondo des molécules de phtalocyanine métallique déposées sur les surfaces métalliques.

La deuxième partie du travail de thèse a été consacré à l'étude des mécanismes d'auto-assemblage et de croissance du film mince des molécules de MnPc sur le substrat Ag (111) ainsi que l'influence des interactions molécule-substrat et molécule-molécule sur la structure électronique et le magnétisme des molécules de MnPc. À faible taux de couverture, les molécules de MnPc sont adsorbées de façon dispersée sur la surface d'Ag (111) en raison des interactions molécule-molécules répulsives à longue portée. Au cours de l'augmentation progressive de la couverture moléculaire jusqu'à l'obtention d'une monocouche, on observe initialement que les molécules MnPc forment de petis amas, puis elles s'accumulent automatiquement en domaines ordonnés à longue distance et finalement forment une structure monocouche compacte. Une évaporation

supplémentaire de la molécule MnPc conduit à la formation d'une deuxième ou une troisième couche au-dessus de la première couche mouillante.

 Nous avons trouvé par les mesures STM à haute résolution spatiale (voir la Figure 4) les trois configurations distinctes pour les molécules de MnPc isolées dans la deuxième couche, c'est-à-dire les configurations ″on-top″, ″Shifted″ et ″Bridge″. Dans le cas ″on-top″, la molécule MnPc de deuxième couche est adsorbée au-dessus d'une molécule de première couche, et les ions Mn centraux des molécules de premières et deuxièmes couches sont alignés verticalement, mais les axes moléculaires du plan MnPc de la deuxième couche sont tournés de 45° autour de l'axe perpendiculaire à la surface. Dans le cas ″Shifted″, la molécule MnPc de deuxième couche est décalée latéralement et son ion Mn central est assis au-dessus de l'atome d'azote d'une molécule MnPc de première couche, tandis que l'orientation moléculaire reste alignée avec celle de la première couche. Dans la configuration ″Bridge″, la molécule MnPc de la deuxième couche est adsorbée à entre deux molécules voisines de la première couche et forme ainsi un pont bien que les axes moléculaires du plan MnPc de la deuxième couche soient tournés de 30 ° par rapport à la molécule MnPc de la première couche.

 A l'étape suivante nous avons montré que le mécanisme de croissance des îles auto-assemblées de la seconde couche de molécules MnPc est dominé par les interactions molécule-molécule, car l'interaction avec le substrat Ag (111) sous-jacent est alors écrantée par la première monocouche. Ce mécanisme est mis en évidence par une évolution complexe de la structure électronique vers un comportement semiconducteur. Les interactions inter-molécules conduisent à la formation d'îlots auto-assemblés méta-stables de molécules de MnPc de deuxième couche avec une configuration d'adsorption parallèle. Alors qu'un recuit thermique ultérieur à une température d'environ 100 °C conduit à la formation d'îlots de deuxième couche plus stables avec une adsorption moléculaire non-planaire et une différence de phase variable des molécules de la deuxième couche par rapport à la première couche. La configuration d'adsorption modulée avec décalage de phase des molécules de MnPc à l'intérieur des îlots de la deuxième couche est une conséquence directe de l'augmentation des interactions inter-molécules induite par la température.
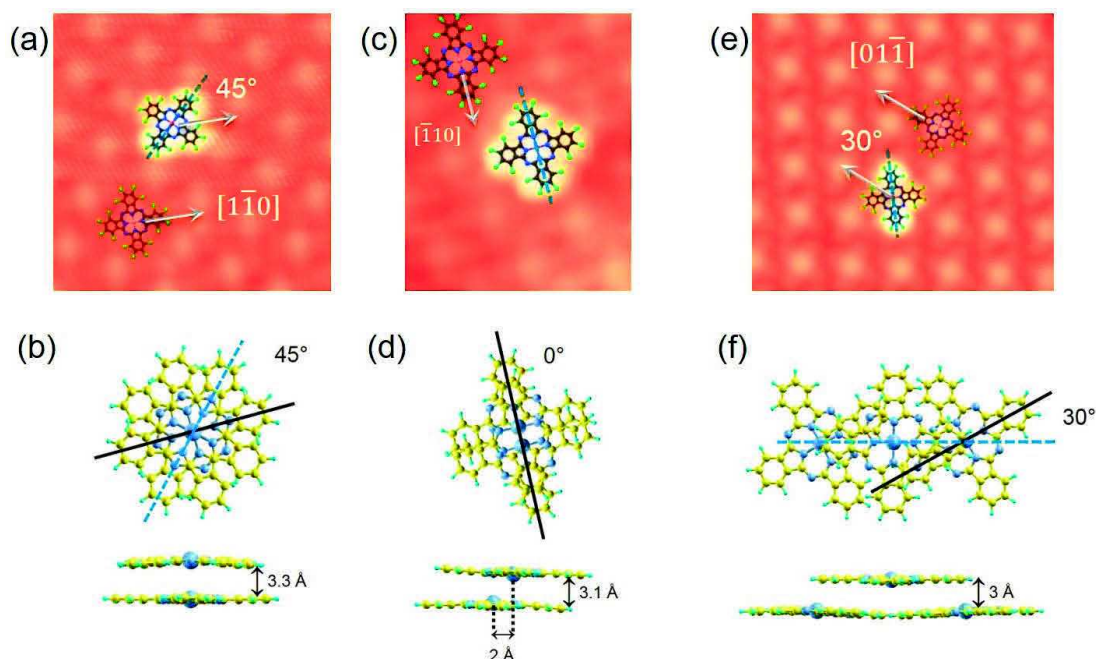
Figure 4 Images STM et les représentations schématiques (vues de dessus et de profil) d'une seule molécule MnPc adsorbée avec (a, b) les configurations de ″on-top″, (c, d) ″Shifted″ et (e, f) et ″Bridge″ de sur la Monocouche de MnPc sur surface Ag (111).

Plus important encore, le sondage de l'effet Kondo par STM haute résolution spatiale/énergétique, nous avons étudié l'influence du site d'adsorption de la molécule sur la résonance Kondo dans la deuxième couche moléculaire : la température de Kondo est passée de T_K = 75 ± 2 K à 105 ± 3 K et 140 ± 5 K lorsque l'on passe d'une configuration ″on-top″ à la configuration ″Bridge″ et ″Shifted″ respectivement pour les molécules MnPc isolées dans la deuxième couche (voir tableau 1). Plus intéressant encore, la tendance de la variation de la température Kondo est en accord avec les constantes de couplage d'échange anti-ferromagnétique précédemment calculées (AFM) pour les molécules MnPc bicouches : J_{on-top} > J_{bridge} > $J_{shifted}$ qui suivent une loi inverse. L'un des résultats centraux de ce travail de thèse est que l'effet Kondo est en compétition avec le couplage d'échange inter-couche AFM dans le système MnPc/Ag (111) bicouches: plus l'échange est fort, plus la température Kondo est basse.

Table 1. Temperature Kondo (T_K) pour la molecule de MnPc sur Ag(111)

Molecule de MnPc	Première couche	Seconde couche		
Configuration	En surface	Shifted	Bridge	On-top
$T_K(K)$	160 ± 10	140 ± 5	105 ± 3	75 ± 2

Pour les molécules de MnPc des amas de la deuxième couche, nous avons constaté que le comportement de Kondo est fortement affecté par les molécules voisines, comme en

témoigne l'évolution complexe du pic Kondo à zéro volt. Contrairement au MnPc isolé, les interactions inter-couches et les interactions magnétiques molécule-molécule intra-couche conduisent à une modification de la résonance Kondo de la molécule MnPc à l'intérieur de l'île de la deuxième couche. Ainsi, nous avons trouvé un comportement oscillatoire de la température de Kondo pour les molécules de MnPc à l'intérieur de l'amas de la deuxième couche à la suite d'un changement de la force de couplage d'échange AFM induite par la modulation de phase.

 Dans la troisième partie de cette thèse, nous avons étudié les possibilités de manipulation du magnétisme de la molécule de MnPc par dopage avec l'atome de Co. Nous avons trouvé par les mesures STM à haute résolution spatiale (voir la figure 5) les trois sites d'adsorption distincts pour l'atome de Co dans la molécule de MnPc, c'est-à-dire le site interstitiel, les sites de benzène sur les axes moléculaires 1 et 2. Dans le cas interstitiel, l'atome de Co est adsorbé entre deux molécules de MnPc et est directement en contact avec le substrat d'Ag (111). Sur les sites de benzène, l'atome de Co est pris en sandwich entre la molécule de MnPc et la surface d'Ag (111). En surveillant l'évolution de l'effet de Kondo avec le site d'adsorption de l'atome de Co dans la molécule de MnPc, nous avons constaté que le site d'adsorption d'atome de Co joue un rôle important dans la modulation du couplage d'échange entre les moments magnétiques de la molécule de MnPc et l'atome de Co.
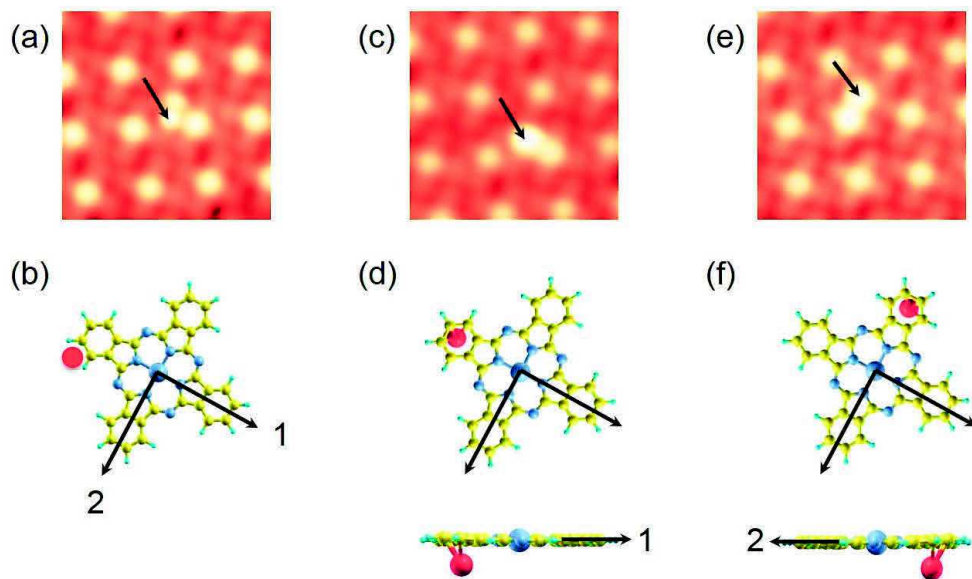

Figure 5: Les images STM et les représentations schématiques (vues supérieures et latérales) de la molécule MnPc dopée avec l'atome de Co (boules rouges) aux positions (a, b) le site interstitiel, les sites de benzène (c, d) sur l'axe 1 et (e, f) Sur l'axe 2 sur la surface Ag (111).

 Dans la dernière partie de cette thèse, en utilisant la capacité pour le STM de détecter l'excitation vibratoire des molécules à travers la spectroscopie de tunnel d'électrons inélastique (IETS), nous avons constaté que l'effet Kondo et le mode vibration étaient

simultanément actifs pour une seule molécule MnPc piégée dans la jonction du tunnel STM. Avec la même technique de spectroscopie STM-IETS, nous avons également démontré que les amas de cérium (Ce) peuvent efficacement collecter et piéger les molécules d'hydrogène (H2). La conductance des objets résultants dans la jonction STM est alors régie par une charge et une transition déterminées par le mode inélastique spécifique de l'hydrogène piégé.

Dans l'ensemble, les résultats de ce travail de thèse pourraient constituer une étape importante dans la compréhension des structures électroniques, magnétiques et vibratoires des molécules de phtalocyanine-métal sur les surfaces métalliques. En particulier, l'étude étape par étape et systématique de MnPc à partir d'une seule molécule jusqu'à la structure bicouche ordonnée nous a permis d'éclairer l'évolution des structures électroniques et magnétiques. En outre, les complexes métal-organiques manipulés localement sur la surface nous ont permis de contrôler la conductance de la jonction en modifiant simplement la résistance du gap. Ce type de contrôle pourrait être un pas en avant pour les applications futures des complexes métal-organique dans les dispositifs nano-électroniques.

References

[1] C. Joachim, J. K. Gimzewski and A. Aviram. *Nature* **408**, 541 (2000)

[2] J. K. Gimzewski and C. Joachim. *Science* **283**, 1683 (1999)

[3] S. A. Wolf, D. D. Awschalom, R. A. Buhrman, et al *Science* **294**, 1488 (2001)

[4] A. J. Heinrich, J. A. Gupta, C. P. Lutz, et al *Science* **306**, 466 (2004)

[5] O. Bekaroglu, Y. Bian, G. Bottari, X. Cai, U. Hahn, N. Ishikawa, J. Jiang, N. Kobayashi et al, Functional Phthalocyanines Molecular Materials (Springer, Berlin, 2010)

[6] L. Bognani and W. Wernesdorfer, Nature Mater. 7, 179 (2008)

[7] K. Moth-Poulsen and T. Bjornholm, Nat. Naotechnol. 4, 551 (2009)

[8] G. Binnig, H. Rohrer, C. Gerber and E. Weibel. *Phys. Rev. Lett.* **49**, 57 (1982)

[9] G. Binnig, H. Rohrer, C. Gerber and E. Weibel. *Appl. Phys. Lett.* **40**, 178 (1982)

[10] J. K. Gimzewski, E. Stoll and R. R. Schlittler. *Surf. Sci.* **181**, 267 (1987)

[11] A. Mugarza, N. Lorente, P. Ordejon, et al Phys. Rev. Lett. 105, 115702 (2010)

[12] S.-H. Chang, S. Kuck, J. Brede, et al Phys. Rev. B 78, 233409 (2008).

[13] M. Kanai, T. Kawai, K. Motai, X. Wang, et al Surf. Sci. 329, L619 (1995)

[14] N. Tsukahara, K. ichi Noto, M. Ohara, et al Phys. Rev. Lett. 102, 167203 (2009)

[15] B. W. Heinrich, C. Iacovita, T. Brumme, et al J. Phys. Chem. Lett.1, 1517 (2010)

[16] C. Iacovita, M. V. Rastei, B. W. Heinrich, et al Phys. Rev. Lett. 101, 116602 (2008)

[17] J. Brede, N. Atodiresei, S. Kuck, et al Phys. Rev. Lett. 105, 047204 (2010)

[18] P. Gargiani, M. Angelucci, C. Mariani, et al Phys. Rev. B 81, 085412 (2010).

[19] H. Peisert, M. Knupfer, and J. Fink, Surf. Sci. 515, 491 (2002)

[20] E. Annese, J. Fujii, I. Vobornik, G. Panaccione, et al Phys. Rev. B 84, 174443 (2011)

[21] S. Stepanow, A. Mugarza, G. Ceballos, et al Phys. Rev. B 82, 014405 (2010).

[22] Y. Y. Zhang, S. X. Du, and H.-J. Gao, Phys. Rev. B 84, 125446 (2011)

[23] X. Chen and M. Alouani, Phys. Rev. B 82, 094443 (2010)

[24] J. D. Baran, J. A. Larsson, R. A. J. Woolley, et al Phys. Rev. B 81, 075413 (2010)

[25] Z. Hu, B. Li, A. Zhao, J. Yang, and J. G. Hou, J. Phys. Chem. C112, 13650 (2008)

[26] Y.-S. Fu, S.-H. Ji, X. Chen, X.-C. Ma, R. et al. Phys. Rev. Lett. 99, 256601 (2007).

[27] L. Gao, W. Ji, Y. B. Hu, Z. H. Cheng, et al Phys. Rev. Lett. 99, 106402 (2007)

[28] Liwei Liu, Kai Yang, Yuhang Jiang, et al Physic. Rev. Lett. 114, 126601 (2015)

[29] Liwei Liu, Kai Yang, Yuhang Jiang, et al Scientific Reports 3, 01210 (2013)

[30] N. Tsukahara, S. Shiraki, S. Itou, et al Phys. Rev. Lett. 106, 187201 (2011)

[31] A. Zhao, Q. Li, L. Chen, H. Xiang, W. Wang, et al Science 309, 1542 (2005).

[32] A. Mugarza, R. Robles, C. Krull, et al Phys. Rev. B 85, 155437 (2012)

[33] K.Jens, K. Michael, S. Jacob, H. Pin-Jui, et al Nano. Lett. 14, 3895 (2014)

[34] A. Mugarza, C. Krull, R. Robles, et al Nat. Commun. 2, 490 (2011)

[35] E. Minamitani, Y. S. Fu, Q. K. Xue, et al Phys. Rev. B 92, 075144 (2015)

[36] X. Chen, Y.-S. Fu, S.-H. Ji, et al Phys. Rev. Lett. 101, 197208 (2008)

Contents

Chapter 1

Introduction to the Kondo effect

When a magnetic impurity is present in a non-magnetic host metal, the low-temperature transport properties of this system are closely related to a phenomenon known as the Kondo effect. This effect leads to anomalous transport properties in the magnetic impurity-host metal systems such as the diluted magnetic alloys and magnetic atoms/molecules on the metal surface. Essentially the Kondo effect is screening of impurity moment by the conduction electrons of the host metal. This screening is related to a coherent spin-flip scattering process between the impurity spin and conduction electrons, thereby gives rise to a sharp resonance at the Fermi level in the energy spectrum of the system. Therefore, the important hallmark of the Kondo effect is the appearance of a resonance state near the Fermi level, which can be detected experimentally by scanning tunneling spectroscopy (STS) measurements. Since the Kondo effect is a characteristic signature of the magnetic impurity in a non-magnetic metal host, it provides a method for scanning tunneling microscopy (STM) measurements to probe the magnetic moments of atoms/molecules on the metal surface.

Since Kondo physics is intrinsically a many-body problem and rather complicated subject, its mathematical descriptions are also relatively complex. In this chapter, therefore, we will present a basic concept of the Kondo effect in a more descriptive way to understand the underlying physical mechanisms involved. The more complete and detailed theoretical treatments on Kondo physics can be found in Ref. [1-4].

1.1 The Kondo effect

The electrical resistivity of a pure metal usually decreases in a monotonous manner with the decreasing of its temperature. This can be well understood in the context of conduction electron scattering due to the lattice vibrations, which are gradually frozen out when reducing the temperature. However, as far back as the 1930s it was observed that the electrical resistivity of some metals exhibited an unusual effect at low temperatures, which would puzzle physicists for over 30 years. For the first time Meissner et al [5] and then de Haas et al [6] experimentally discovered that the electrical resistivity of the magnesium (Mg) sample as well as some other metals firstly decreased with the temperature down to a minimum resistivity at a certain temperature of about 0(10 K) and then increased again as $-ln(T)$ when the temperature was lowered further. This upturning behavior of the electrical resistivity at low temperature was called *resistance minimum phenomenon,* which opened a new window for many-body condensed matter physics to study the low

temperature behavior of the electron systems. As an example, a typical resistance minimum phenomenon was observed in the dilute copper-iron alloys prepared by dissolving a few amounts of magnetic iron (Fe) impurities into the copper (Cu) crystal shown in Figure 1.1.
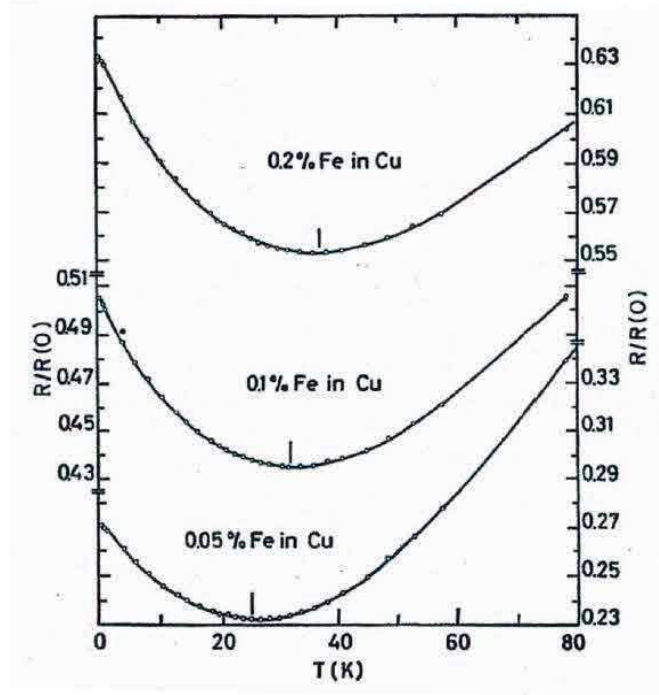

Figure 1.1 The resistance minimum as a function of temperature for the copper (Cu) crystal with different concentration of iron (Fe) impurities. Figure from Ref.[7].

In the case of pure metal, it is well-known from solid-state physics that the electrical resistivity of metals is caused by the (back) scattering of conduction electrons from the crystal lattice vibrations (i.e. phonons) and the static structural defects in the lattice itself, which effectively hinders the motion of conduction electrons through crystal metal. As the sample temperature lowers towards absolute zero, the lattice vibrations are gradually frozen out and the phonon contribution to the resistivity drops monotonically as fast as $\propto T^5$. However, the contribution of the static defects is essentially temperature independent and only appears as a finite residual resistivity at low temperature. Therefore the total resistivity of pure metal usually monotonically decreases with temperature and finally saturates at low temperatures rather than increase again after reaching down to the minimum at a certain temperature. On the other hand, this theory for the electrical resistivity of pure metal cannot explain the observed logarithmic increasing of electrical resistance in the dilute magnetic alloys at low temperatures (see Figure 1.1).

Later it was experimentally confirmed that the *resistance minimum phenomenon* occurs only if the metal sample contains dilute magnetic impurities, such as iron (Fe) or cobalt (Co) atoms. In addition, the scaling of the low-temperature resistance with impurity

concentration indicates that the temperature of minimum resistance is weakly depending on the magnetic impurity concentration (see Figure 1.1). This behavior revealed that the anomalous effect in electrical resistivity essentially arises from the interaction of the conduction electrons in the host metal with individual magnetic impurity atoms embedded in the metal matrix, and not from the interactions between those magnetic impurities.
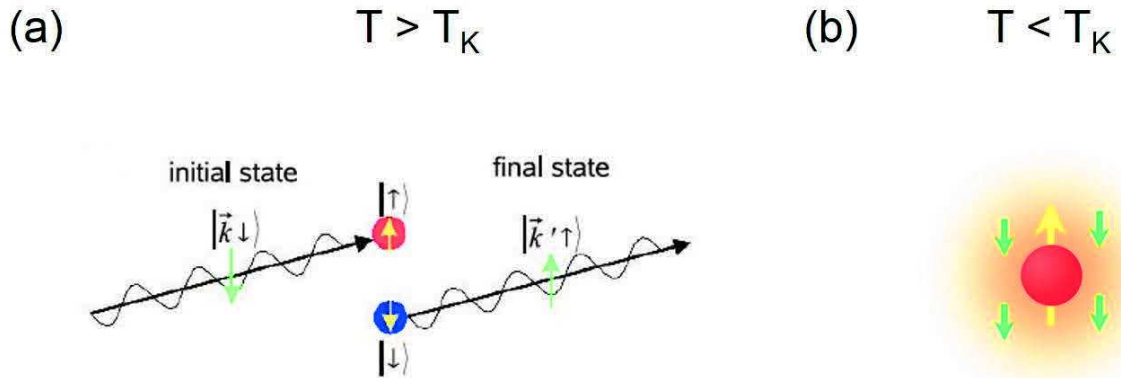
(a)   T > T$_K$ (b)   T < T$_K$

Figure 1.2 (a) Kondo scattering on a single magnetic impurity just above the Kondo temperature T_K. The conduction electron in an initial state $|\vec{k}\downarrow\rangle$ can be scattered at the single magnetic impurity into a new state $|\vec{k'}\uparrow\rangle$ through spin exchange with the spin moment of impurity atom, while simultaneously the localized spin moment of impurity is flipped from the "up" to "down" state. While in (a) the dynamic state of the spin-flip scattering process is shown, (b) Kondo screening of the impurity moment by the conduction electrons of host metal. Below the Kondo temperature T_K, the localized moment of impurity permanently falls into a many-body singlet ground state. Figure from Ref.[8].

The upturning behavior of electrical resistivity observed in the dilute magnetic alloys was explained theoretically, at a satisfactory level, by Jun Kondo [9-10] in the 1960s, by considering an additional low energy scattering mechanism for the conduction electrons. In the perturbation theory J. Kondo takes explicitly into account the spin-flip scattering processes between the spin of the conduction electrons in the host metal and the spin of localized magnetic impurities through the spin exchange mechanism (see Figure 1.2(a)). He described the spin-flip scattering processes in the s-d exchange interaction model or so-called Kondo model. The Kondo Hamiltonian is written as following:

$$H = H_{Bloch} + H_{s-d} \qquad (1.1)$$

$$H_{s-d} = -J\vec{S}\cdot\vec{s} \qquad (1.2)$$

The first term H_{Bloch} describes the non-interacting conduction electrons in a Bloch model, while the second term H_{s-d} describes the s-d exchange interaction which couples the spin $\vec{S}$ of the impurity to the spin $\vec{s}$ of the conduction electrons through the exchange coupling constant J.

The calculation of electrical resistivity for this s-d exchange model using perturbation theory up to the second order term gives essentially the same results as those for purely potential (phonon) scattering, while the perturbation theory calculations up to the third

order term give a logarithmic contribution to the electrical resistivity at low temperatures. When this logarithmic term is added to the phonon contribution of electrical resistivity, it provides satisfactory explanation for the experimentally observed resistance minimum in the dilute magnetic alloys (see Figure 1.1). The total electrical resistivity derived by J. Kondo is as follows [10]:

$$\rho(T) = \rho_0 + aT^5 + bJln(\frac{T}{c}) \qquad (1.3)$$

where ρ_0 is the residual resistance; a, b and c are constants. The second term (i.e. aT^5) is the contribution from the lattice vibrations, while the third logarithmic term is the contribution from the magnetic impurities. The functional expression of the electrical resistance in Eq(1.3) indicates that at any temperature both the lattice vibrations as well as the magnetic impurities could contribute simultaneously to the electrical resistivity but with dramatically different temperature-dependent dominance. At high temperatures the phonon contribution dominates with T^5, while the logarithmic dependence due to the magnetic impurities only dominates at low temperatures. The increasing of electrical resistance at low temperatures (see Figure 1.1) can be explained by the means of Kondo solution in Eq(1.3) when only the sign of exchange coupling constant J is negative (i.e. $J < 0$). This negative coupling sign is the most important necessary condition for the Kondo solution to produce the correct results. On the other hand, the Kondo perturbation calculation predicts the presence of an anti-ferromagnetic exchange coupling between the impurity spin and the spin of conduction electrons in the metal host (see Figure 1.2(a)).

Although Kondo's theory correctly describes the observed upturning of the electrical resistance at low temperatures, the $-ln(T)$ term diverges as $T \rightarrow 0\ K$ and also gives the unphysical prediction that the resistivity will be infinite even at very low temperatures. Thus Kondo's solution in Eq(1.3) is correct only above a certain temperature below which the Kondo model will be broken down. This critical temperature is known as the Kondo temperature T_K:

$$k_B T_K \cong Dexp(-1/2J\rho_0) \qquad (1.4)$$

where D is the half-width of the conduction band of the host metal, J is the s-d exchange coupling constant, and ρ_0 is the density of state at the Fermi level.

Due to this limitation of Kondo model, a more sophisticated and comprehensive theory was needed to explain the actual low temperature behavior or ground state of the electron systems of the diluted magnetic alloys. The search for such a theory opened a new and fascinating field of research for many-body condensed matter physics, and became known as the Kondo problem [1,11-13].

The magnetic susceptibility measurements on the dilute magnetic alloys [14] revealed another low-temperature anomalous behavior in this electron system showing minimum resistance. The magnetic susceptibility of the dilute magnetic alloy ceases to follow the Curie–Weiss law and saturates to a constant value at temperatures below the Kondo temperature T_K , where the electrical resistance increases logarithmically with the

decreasing of the temperature. This experimental observation indicates that the magnetic moment of impurity is completely quenched at low temperatures below T_K as if the impurity spin moment had disappeared. This behavior can be understood by the formation of a many-body singlet ground state below the Kondo temperature T_K [15-16] due to the screening of the impurity spin moment by the conduction electrons in the metal host through an anti-ferromagnetic exchange coupling (see Figure 1.2(b)). Furthermore, this result concluded that the reason why the Kondo perturbation calculations gave the unphysical results at the temperatures below T_K - the logarithmic divergence of the electrical resistance - was because the Kondo model disregarded the existence of a many-body singlet bound state and, instead, started with degenerate localized spin state.

1.2 The Anderson model

In the Kondo model for the dilute magnetic alloys, the low-temperature increase in the electrical resistance was interpreted by the means of dynamical spin-flip scattering processes between the spin moment of impurity and the spins of conduction electrons in the metal host. In the following we will give a description of the Kondo problem by means of the Anderson model that illustrates the interaction between a single magnetic impurity and the metal host in a more physical way. This intuitive model for describing a magnetic impurity inside a conducting metal was introduced by P. W. Anderson [17]. Compared to the Kondo model, the Anderson model provides a very physical description of the single magnetic impurity interacting with the conduction electrons of the host metal, and thus helps us to understand much more deeply Kondo physics in the dilute magnetic alloys.

The so-called single-impurity Anderson model assumes that the magnetic impurity atom can be described by a localized state which can be either singly or doubly occupied. A transition metal impurity (e.g. Co atom) has unpaired electrons in the $3d$ orbital, and therefore the localized state has a $3d$ character. The energy level $\mathcal{E}_d$ of the localized state occupied by a single electron is located below the Fermi level of the host metal. This singly occupied $3d^1$ state is separated by the Coulomb repulsion energy U from the $3d^2$ state occupied by two electrons with opposite spins which is called doubly occupied state (see the figure 1.3(a)). The host metal is represented by a continuum of states (i.e. energy band) filled with the non-interacting conduction electrons up to the Fermi level E_F. The hybridization between the impurity $3d$ states and the continuum conduction band states in the host metal leads to a broadening of the $3d$ states by $\Delta = \rho_0 |V|^2$ where ρ_0 is the density of state at E_F in the host metal and V is the hybridization matrix element that describes coupling between the localized state and the continuum of band states at E_F.

As we have seen in the Kondo model, the conduction electrons of the host metal can be scattered on the magnetic impurity, and thus the spin exchange process takes place between the spin moment of impurity and the spins of surrounding conduction electrons. This spin exchange process can flip the spin moment of the impurity from the "up" to the

"down" state, or vice versa, while simultaneously a spin excited conduction electron state around the magnetic impurity is created (see Figure 1.2(a)).
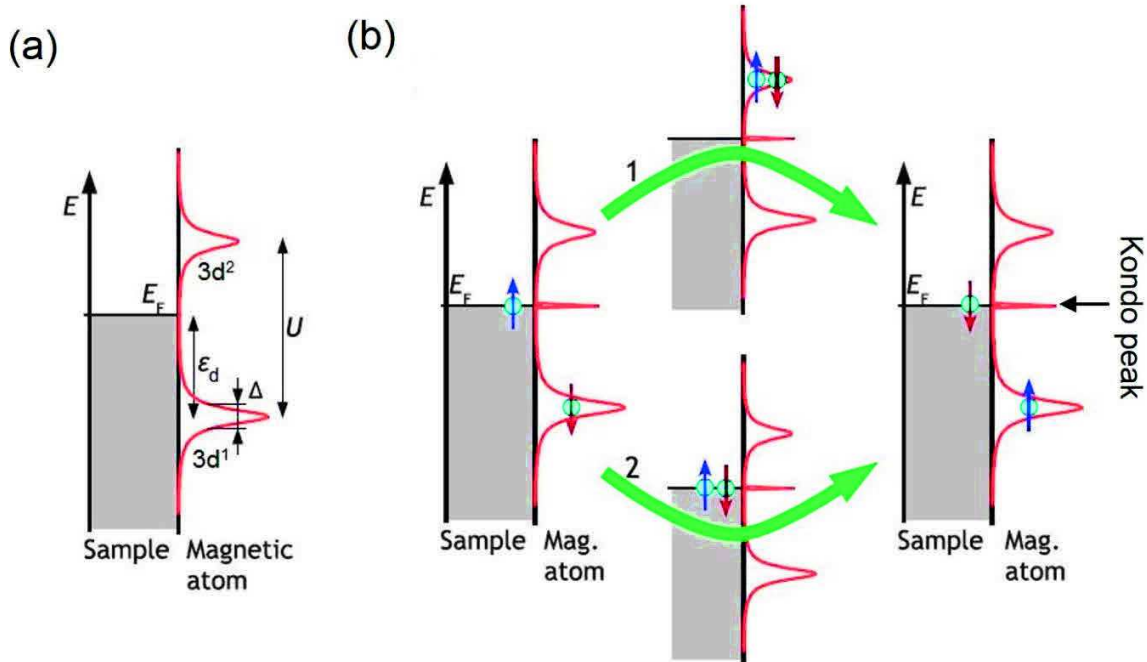

Figure 1.3 (a) Schematic drawing of energy diagram for the Kondo system within a single impurity Anderson model. The singly occupied state $3d^1$ is located below the Fermi level at an energy ε_d, and separated by the Coulomb repulsion energy U from the doubly occupied state $3d^2$. (b) Spin-flip process in the Anderson model. The $3d$ orbital is initially occupied by a single electron with spin ($\downarrow$). The two virtual processes can flip the spin of the singly-occupied orbital, either through process (1) or process (2). The conduction electron at the Fermi level involved in the spin-flip process form a new resonance at the Fermi level. The Figure from Ref.[8].

In the framework of the Anderson model this spin-flip process can also be realized in two different virtual excitation processes: either by first emptying the singly occupied $3d$ state ($3d^1 \to 3d^0$), and then refilling it ($3d^0 \to 3d^1$), or by first putting a second electron into the singly occupied $3d$ state ($3d^1 \to 3d^2$) and successively removing one electron ($3d^2 \to 3d^1$). The final $3d^1$ state, however, can be in the opposite spin state as compared to the initial one. These two processes are schematically drawn in Figure 1.3(b) and will be discussed in detail below.

Let's assume that the temperature is sufficiently low ($T \ll T_K$) to exclude thermal excitations and any possible influence of temperature on the system. An electron removing from the localized $3d$ state to an empty state at E_F of the metal requires at least an energy of $|\varepsilon_d|$. It is classically forbidden to take an electron from the localized impurity state without feeding energy into the system although in quantum mechanics the Heisenberg uncertainty principle allows such excitation as a virtual process for a very short time in the order of $h/|\varepsilon_d| \sim 10^{-15}\,s$, where h is Planck constant. Thus, the spin-

down electron initially occupying the energy level $\mathcal{E}_d$ may tunnel out of the impurity site to briefly occupy a classically forbidden intermediate conduction band state at E_F outside of the impurity atom. Within this short timescale, another electron must tunnel from the occupied Fermi sea back into the impurity atom. However, the spin of this new electron may point in the opposite direction as compared to the initial one. Thus, the impurity spin is effectively flipped from the spin-down (↓) state to the spin-up (↑) state without any energy cost, while simultaneously the spin of conduction electron at E_F is flipped from the spin-up (↑) state to the spin-down (↓) state by this virtual excitation process (see the spin-flip process (2) in Figure 1.3 (b)).

Applying the same arguments such a spin-flip is also possible via another virtual excitation process. As shown by the process (1) in Figure 1.3(b), an electron from the conduction band state may tunnel into the impurity atom, and temporarily doubly occupy it within a short timescale in the order of $h/|\mathcal{E}_d + U| \sim 10^{-15}\ s$. According to the Pauli principle, the spin of the incoming electron has to be opposite to the one of the impurity electron. If now the original localized spin-down electron tunnels out, the new spin-up electron is kept in the impurity atom, thus the impurity spin is flipped again from the spin-down (↓) to the spin-up (↑) state, and this spin-flip process takes place at zero-energy cost as well. It must be emphasized that the spin of conduction electron at E_F is simultaneously flipped from the spin-up (↑) to the spin-down (↓) state.

One of the important conclusions here is that the spin exchange process between the spin of localized impurity and the spin of conduction electrons is a coherent spin-flip scattering process which takes place at an instant time. Moreover, if we take as a whole the Kondo system which consists of a magnetic impurity interacting with the conduction electrons in the host metal, the spin-flip scattering from the initial singlet configuration of the system to the final singlet configuration, or vice versa, takes place at zero energy cost. Indeed, there is no exchange of energy between the initial and final singlet configurations of the Kondo system (see Figure 1.3(b)). Thus, the ground state of the Kondo system is the two-fold degenerate singlet state. Therefore, the coherent spin-flip scattering processes between two degenerate Kondo singlet states qualitatively change the energy spectrum of the system. The Kondo effect is thus produced by a combination of many such spin-flip scattering events taken together, and this phenomenon results in the appearance of a new resonance state at the Fermi level in the energy spectrum, which is commonly known as the Kondo resonance (see Figure 13(b)). The half-width at half-maximum (Γ) of the Kondo resonance is related to a characteristic temperature, so-called Kondo temperature T_K. Within the Anderson model, the characteristic Kondo temperature T_K can be described by the parameters of the system [1]:

$$k_B T_K \cong \sqrt{2\Delta \frac{U}{\pi}} \exp\left[-\frac{\pi}{2\Delta} \left(\left| \frac{1}{\mathcal{E}_d} \right| + \left| \frac{1}{\mathcal{E}_{d+U}} \right| \right)^{-1} \right]$$ (1.5)

Where Δ is energy width of the localized state $\mathcal{E}_d$ below the Fermi energy, U is the Coulomb repulsion energy.

It should be note that there is one very important difference between the Kondo singlet ground state simply described above and the real ground state of the Kondo system. As shown in Figure 1.3(b), the formation of Kondo singlet state is simply described by the single impurity spin and a single conduction electron. Indeed, the true Kondo singlet state would be formed by the screening of the impurity spin moment by all of the conduction electrons close to E_F at the local site of impurity (see Figure 1.2(b)). Therefore, the Kondo resonance is intrinsically a consequence of collective interaction of a many-body system. If we take the Kondo system as a whole which consists of a magnetic impurity and the conduction electrons in the host metal interacting with it, they form a non-magnetic many-body singlet state in which the impurity spin is paired up with many conduction electron spins from the host metal (see Figure 1.2(b)).

1.3 The detection of Kondo effect with STM

The Kondo effect has been studied in the variety of different Kondo systems by many experimental techniques including scanning tunneling microscopy (STM) [18-19], ultra-violet and x-ray photoelectron spectroscopy [20-21], mechanically controllable break junction [22-23]. Compared with other techniques, the high spatial and high energy resolution ability of STM makes it a promising tool to study the Kondo effect in the smallest conceivable Kondo systems, such as a single magnetic atom/molecule on metal surface. In the STM spectroscopy measurement on a magnetic atom/molecule on metal surface, however, the Kondo resonance is generally not detected as a resonance peak at the Fermi level, but rather a dip-like structure.
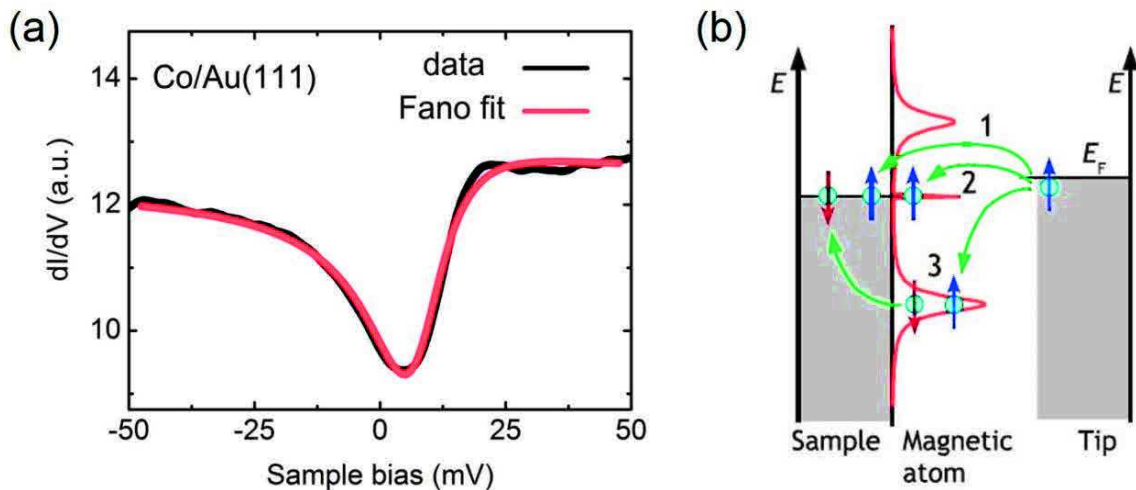
Figure 1.4 (a) dI/dV spectrum measured above a Co atom adsorbed on Au(111). (b) Schematics of the tunneling paths for the electron from a probe tip to the magnetic impurity. Figure from Ref.[8]. Path 1 represents the electron tunneling into the conduction band state of substrate. Path 2 describes the electron tunneling into the Kondo resonance state. In these two paths the electron spin conserves and no spin flipping is expected. Path 3 describes an indirect tunneling via a spin-flip process on the magnetic impurity.

The pioneering observations of the Kondo effect with STM on the single magnetic atoms adsorbed on metal surfaces, like Co/Au(111) and Ce/Ag(111), were reported in 1998 by Madhavan et al [18] and Li et al [19], respectively. Madhavan and his co-workers used STM to perform spectroscopic measurement on a single Co atom on Au(111) surface. The scanning tunneling spectroscopy (dI/dV versus V) measured on the Co adatom on Au(111) displays a characteristic asymmetric dip feature around the zero bias which is absent for non-magnetic atoms (see Figure 1.4(a)). This spectroscopic feature at zero bias was identified as the Kondo resonance of Co atom on Au(111) and we reproduced a similar Kondo dip feature for this system as shown by the black curve in Figure 1.4(a). The line shape of this feature was interpreted as a quantum Fano interference between the Co 3d orbital and the conduction electron channels for an electron tunneling from the probe tip into a magnetic Co atom on Au(111) surface (see Figure 1.4(b)).

Below, we will explain this Fano interference between the different electron tunneling channels with a well-known example of STS measurement on the Co atom on Au(111). The electrons originating from the probing tip have three possible pathways to tunnel into Co adatom on Au(111) surface. The first pathway is direct tunneling into the empty bulk states above E_F of Au(111) substrate. The second pathway is directly tunneling into the Kondo resonance near the Fermi level. The third possible pathway is indirectly tunneling into the hybridized and localized 3d state of the magnetic Co impurity. In this third tunneling process, the electron has its spin flipped and is located at E_F in its final state. The first and second tunneling paths conserve the spin orientation and these two coherent electron tunneling channels interfere with each other. This interference, known as Fano interference, is responsible for determining the line shape of Kondo resonance in STS spectrum. The Fano resonance exhibits different asymmetric profiles due to the interference between the resonant state and continuum state electron tunneling with different probabilities. U. Fano showed that the interference between two electron pathways leads to an energy spectrum which is described by the so-called Fano equation [24].

$$\rho(\epsilon) \propto \rho_0 + \frac{(q+\epsilon)^2}{(1+\varepsilon^2)} \tag{1.6}$$

where ε is the normalized energy: $\varepsilon = \frac{E-E_K}{\Gamma}$, Γ is half width at half maximum, E_K is position of resonance. q is the line shape parameter. The Fano line shape is Lorentzian peak for $q = \infty$, while it is a Lorentzian dip for $q = 0$. For the intermediate values of q, the Fano function gives a S-like curve as shown in Figure 1.5.

To determine the characteristic Kondo temperature of Co/Au(111) system (see Figure 1.4(a)), the Fano line shape is fitted to the characteristic dip-like Kondo resonance thereby we obtain the uncorrected value of $T_K = 80 \pm 10\ K$ which is close to the $T_K = 70 \pm 5\ K$ found by Madhavan and his co-workers [18].
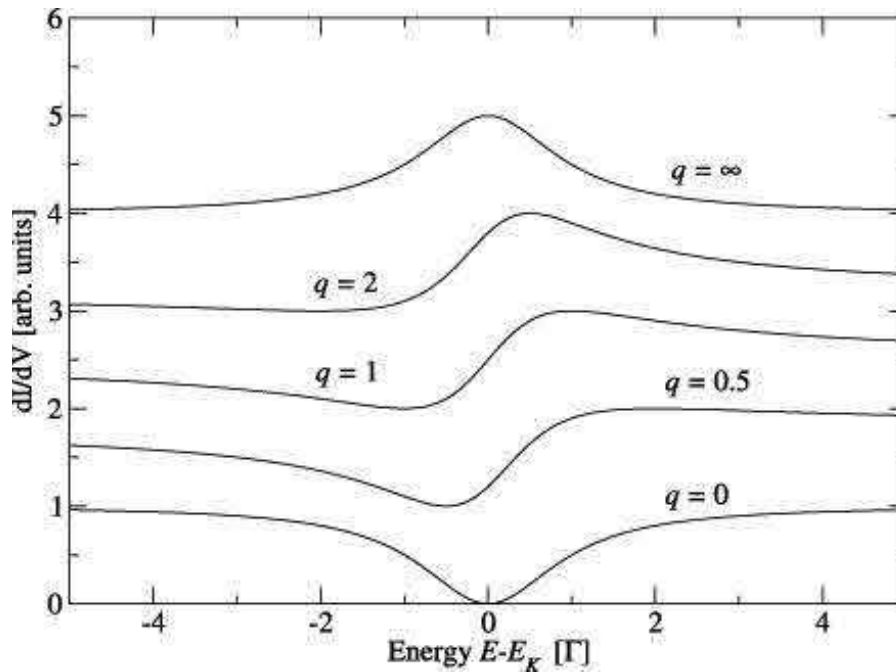
Figure 1.5 Simulated Fano line shapes for different q values: a Lorentzian dip for $q = 0$ which corresponds to tunneling mainly by path 1. In the limit large q a Lorentzian peak is formed due to tunneling by path 2. The intermediate values of q gives the s-like curves. Figure from Ref.[8].

1.4 The external parameter dependence of Kondo effect

 Usually the Kondo resonance measurement requires a complete characterization of the Kondo peak. The important hallmarks of the Kondo effect are: (i) the characteristic broadening and reduction of the Kondo resonance at increased temperatures, and (ii) the splitting of the Kondo resonance under the external applied magnetic field. These unique characteristics make the Kondo resonance totally different from any other source of zero-bias anomaly such as for example a low energy (3-4 meV) excitation of vibration mode at the Fermi level due to the presence of hydrogen on the substrate [25].

 The full characterizations of Kondo resonance can be achieved by STM technique through changing experimental parameters such as the temperature and magnetic fields. The temperature and magnetic field-dependent measurements of Kondo resonance can be done controllably using the Zener heating diode and the built-in magnetic field of STM. However, due to the small Bohr magneton value ($\sim 57.9 \mu eV/T$), usually a large magnetic field is mandatory to detect the splitting of the Kondo peak.

1.4.1 The temperature dependence

 At the absolute zero temperature, i.e. at zero thermal energy $k_B T = 0$, the Kondo system consisting of a magnetic impurity interacting with the host metal stays in its ground state.

Thus the Kondo ground state is a spin-singlet and two-fold degenerate state. The spin-flip scattering process between these two degenerate Kondo states is a coherent scattering which leads to a new resonance at E_F, which we called Kondo resonance in Section 1.2. It has a half-width at half-maximum $\Gamma(\text{T} = 0\text{K})$ is equal to $k_B T_K$ which is a characteristic energy of the Kondo system gained by the formation of the singlet ground state when temperature is lowered down to the absolute zero temperature.

While at the finite temperature, i.e. $0 < T < T_K$, the thermal energy $k_B T$ induces the excitation of electron-hole pairs at E_F of the metal. Thus, the Kondo system stays in its excited state, and the Kondo state is no longer spin-singlet and but keeps its two-fold degeneracy. Although the electron-hole pair excitations lead to a decoherent spin scattering, at finite temperature of $0 < T < T_K$ the thermally excited electron-hole pairs could not completely destroy the coherent spin-flip scattering between these two degenerate Kondo states. The coherent as well as decoherent spin-flip scattering processes lead to a broadened Kondo resonance at the Fermi level. The temperature dependent width of the Kondo resonance is given by the Fermi-liquid treatment of Kondo effect [26]:

$$\Gamma(T) = \frac{1}{2}\sqrt{(\alpha k_B T)^2 + (2 k_B T_K)^2} \tag{1.7}$$

In addition, the numerical renormalization group (NRG) result [27] for the conductance in the Kondo regime shows that the height of Kondo peak strongly depends on temperature described by the following expression [28]:

$$G(T) = \bar{G}\left[1 + \left(\frac{T}{T_K}\right)^2 \left(2^{1/s} - 1\right)\right]^{-s} + C \tag{1.8}$$

where $s = 0.22$ for the spin S=1/2 impurity, and $\bar{G}$ and C are free parameters

When the temperature is increased above the Kondo temperatures, i.e. $T > T_K$, the thermal energy $k_B T$ excites a lot of electron-hole pairs at E_F in the metal. Thus the Kondo singlet state is destroyed and the impurity spin moment is fully recovered due to the out of screening from the conduction electrons. In other words, the electron-hole pair excitations at the thermal energy of $k_B T > k_B T_K$ lead to the complete destruction of the coherent spin-flip scattering. Thus, the spin scattering is completely random in the same way as the free electron gas and the Kondo resonance state at E_F is switched off.

1.4.2 The magnetic field dependence

As mentioned above, at the absolute zero temperature the ground state of the Kondo system is the two-fold degenerate state. When an external magnetic field is applied, the Kondo system stays in its excited state and the two-fold degeneracy is split due to the Zeeman effect. Thus the spin-up scattering is no longer degenerate with the spin-down scattering and the Kondo scattering is destroyed.

 However, under a weak magnetic field meets the condition of $B < k_B T_K / g\mu_B$, where μ_B is the Bohr magneton and g the Landé factor, the destruction is not complete and the electrons of higher energy can interfere with opposite spin electrons if their energy difference is exactly equal to the Zeeman splitting energy $\Delta z = g\mu_B B$. Indeed, this is an inelastic effect and at the threshold energy of this inelastic effect the electrons can spin-flip coherently recovering the Kondo peak, but instead of being centered at E_F, the new peak is centered at the energy of the inelastic excitation. Since the electrons above E_F and the holes below E_F can produce this inelastic effect, there are two new peaks that appear replacing the initial Kondo peak when the magnetic field is switched on. In general, under the external magnetic field B, the Kondo peak at E_F is split into two peaks at $E_F \pm g\mu_B B$ due to the Zeeman splitting of the two-fold degenerate Kondo state. These two peaks are separated by the two times of Zeeman energy for a spin-1/2 impurity:

$$\Delta E = 2g\mu_B B \tag{1.9}$$

 While under the strong magnetic field of $B > k_B T_K / g\mu_B$, the Kondo scattering is neither degenerate nor coherent, thus all peaks disappear. On the other hand, the impurity moment cannot be screened by conduction electrons under the large magnetic field. Then the Kondo resonance is switched off.

References

[1] A. C. Hewson, The Kondo problem to heavy Fermions, Cambridge University press, Cambridge, MA, (1993)

[2] P. Fulde, Electron correlations in molecules and solids, Springer (1993)

[3] G. Grosso and G. P. Parravicini, Solid State Physics, Academic Press, 1st edition (2000)

[4] P. Phillips, Advanced Solid State Physics, Westview Press, 1st edition (2002)

[5] W. Meissner and B. Voigt, Messungen mit Hilfe von flussigem Helium XI Widerstand der reinen Metalle in tiefen temperaturen Annalen der Physik, 399, 892 (1930).

[6] W. J. de Haas, J. de Boer, G. J. van den Berg, The electrical resistance of gold, copper and lead at low temperatures. Physica 1, 1115 (1934)

[7] J. P. Franck, F. D. Manchester, D. L. Martin, The specific heat of pure copper and of some dilute copper + iron alloys showing a minimum in the electrical resistance at low temperatures, Proc. R. Soc. (London) A 263, 494 (1930).

[8] M. Terns, A. J. Heinrich, W. D. Schneider, J. Phys.: Condens. Matter 21, 053001 (2009).

[9] Jun Kondo, Prog. Theor. Phys. 34, 37 (1964)

[10] Jun Kondo, Phys. Rev. 169, 437 (1968)

[11] K. G. Wilson, Rev. Mod. Phys. 47, 773 (1975)

[12] J. Kondo, the physics of dilute magnetic alloys, Syokabo, Tokyo (1983)

[13] N. Andrei, K. Furuya, J. Lowenstein, Rev. Mod. Phys. 55, 331 (1983)

[14] C. M. Hurd, Phys. Rev. Lett. 18, 1127 (1967)

[15] K. Yosida, Phys. Rev. 147, 223 (1966)

[16] A. Okiji, Prog. Theor. Phys. 36, 712 (1966)

[17] P. W. Anderson, Phys. Rev. 124, 41 (1961)

[18] V. Madhavan, W. Chen, T. Jamneala, M. F. Crommie et al Science 280 567 (1998)

[19] J. T. Li, W-D. Schneider, R. Berndt and B. Delley, Phys.Rev. Lett. 80, 2893 (1998).

[20] F. Patthey, B. Delley, W-D. Schneider and Y. Baer, Phys. Rev. Lett. 55, 1518 (1985)

[21] F. Patthey, J-M. Imer, W-D. Schneider, H. Beck, et al Phys. Rev. B 42, 8864 (1990)

[22] W. Liang, M. P. Shores, M. Bockrath, J. R. Long and H. Park, Nature 417, 725 (2002)

[23] S. Wagner, F. Kisslinger, S. Ballmann, et al <u>Nat. Nanotechnol. 8, 575 (2013)</u>

[24] U. Fano, <u>Phys. Rev. 124 1866 (1986)</u>

[25] W. A. Hofer, G. Teobaldi, and N. Lorente, <u>Nanotechnology 19, 305701 (2008)</u>

[26] K. Nagaoka, T. Jamneala, et al <u>*Phys. Rev. Lett.* **88**, 077205 (**2002**)</u>

[27] T. A. Costi, A. C. Hewson et al <u>J. Phys. Condens. Matter 6, 2519 (1994)</u>

[28] D. Goldhaber-Gordon, et al <u>Phys. Rev. Lett. 81, 5225 (1998)</u>

Chapter 2

Scanning tunneling microscopy and spectroscopy

In this chapter, we will briefly introduce the physical principles of scanning tunneling microscopy (STM), scanning tunneling spectroscopy (STS) and inelastic electron tunneling spectroscopy (IETS) which are the experimental techniques used in this thesis work. Then we will give a short description of the ultra-high vacuum (UHV) and low-temperature STM setup and the sample preparation procedures.

2.1 The operating principle

The basic operation principle of scanning tunneling microscopy (STM) is based on the concept of quantum tunneling effect, which allows the electron tunneling through a vacuum potential barrier between two metal electrodes. In an STM configuration the tip and sample represents these two electrodes. It is known from quantum mechanics that the electron wave functions can exceeds the geometrical boundary of a metal surface and its amplitude exponentially decay into the vacuum over a few atomic dimensions [1]. When a sharp tip approaches very closely to the metal surface and held it at a distance of several Angstrom (Å) above the surface, at these distances, the tip's and surface's electron wave functions are overlap with each other, and built a quantum contact between the tip and sample. This is equivalent to opening of a channel for the electron tunneling through the vacuum potential barrier between the tip and sample. Thus, there is a finite transfer probability for the electron to tunnel from tip to the sample or vice versa.

In the absence of the applied bias voltage, the tunneling probability for the electron transfer from tip to the sample is equal to that for the electron tunneling from sample to the tip, and hence no net tunneling current would be detectable. Once a bias voltage is applied between the tip and sample, one tunneling direction is more favored and induces a net tunneling current to flow through the vacuum gap between them. This tunneling current can be measured, and it depends on the bias voltage and the distance between the tip and sample.

In the below, we will give a theoretical description for the tunneling current which flows between the tip and the sample. If the sample is biased by a positive voltage ($V > 0$) with respect to the tip, this effectively lowers the Fermi level of the sample with respect that of the tip (see Figure 2.1 (b)). As a result the electrons will tend to flow out of the filled states of the tip into the empty states of the sample, and hence gives a net tunneling current flow

from sample to tip (note that the tunneling current follows in opposite direction to that of the electron tunneling).
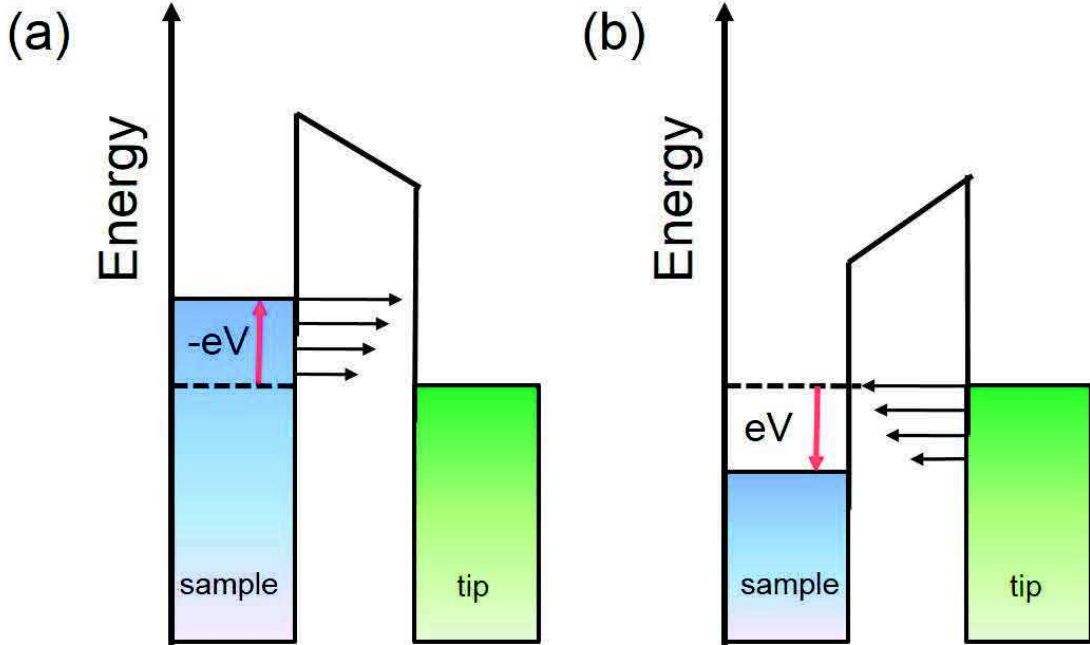

Figure 2.1 Scheme of the STM tunneling junction. (a) Negative sample bias: the electrons tunnel from filled sample states into the empty tip states. (b) Positive sample bias: the electrons tunnel from filled tip states into empty sample states. Figure are adapted from Ref.[2].

Although the tunneling current for a positive sample bias (V > 0) is dominated by a current flow from sample to tip, there will also be a small tunneling current from tip to sample. Within Tersoff and Hamann [3-4] model, the total tunneling current from sample to the tip can be evaluated by summing over all the relevant electronic states [5]:

$$I = \frac{4\pi e}{\hbar} \int_{-\infty}^{+\infty} \rho_t(\epsilon - eV)\rho_s(\epsilon)(f_t(\epsilon - eV) - f_s(\epsilon)) \times |M|^2 d\epsilon \qquad (2.1)$$

where $f(\epsilon)$ is the Fermi-Dirac distribution defined as $f(\epsilon) = (1 + \exp(\epsilon/k_B T))^{-1}$, $\rho_s(\epsilon)$ and $\rho_t(\epsilon)$ are the local density of states (LDOS) of sample and tip, respectively. M is the tunneling matrix element and determined by the overlap of the wave functions of the tip and sample according to the Bardeen formalism [6] as following:

$$M = -\frac{\hbar^2}{2m} \int d\vec{S} (\psi^* \nabla \chi - \psi \Delta \chi^*) \qquad (2.2)$$

The integral is done on the separation surface S between the tip and sample, ψ and χ are the wave functions of the tip and sample. For a trapezoidal tunneling barrier, the simplified one-dimensional form of the tunneling matrix Equation (2.2) is given by Wentzel-Kramer-Brillouin (WKB) approximation [7]:

$$|M(\epsilon, eV, z)|^2 = exp\left[-2z\sqrt{\frac{m_e}{\hbar^2}(\Phi_t + \Phi_s - eV + 2\epsilon)}\right] \tag{2.3}$$

where Φ_t, Φ_s are the work functions of the tip and sample, and z is the tip-sample distance. Note that the expression of tunneling matrix element in Equation (2.3) indicates that the highest contribution in the tunneling current Equation (2.1) comes from the electronic states close to the Fermi energy of sample (V < 0) or the tip (V > 0) as shown by the schematic representation in Figure 2.1(a) and (b).

The tunneling current Equation (2.1) can be simplified in the several ways. First, if the measurements are made at low temperature meets the condition of $K_B T \ll |eV|$, i.e. the thermal broadening of the Fermi level is sufficiently small compared to the energy of electron with respect to the Fermi level, the Fermi-Dirac distribution $f(\epsilon)$ is then approximated by a step function. Thus the tunneling current Equation (2.1) becomes

$$I = \frac{4\pi e}{\hbar}\int_0^{eV} \rho_s(\epsilon)\rho_t(\epsilon - eV)|M|^2 d\epsilon \tag{2.4}$$

Assuming further that the tunneling matrix element $|M|$ does not change significantly with the sample bias voltage meets the condition of $|eV| \ll \Phi_s, \Phi_t$, we obtain following relation:

$$I \cong \frac{4\pi e}{\hbar}|M|^2\int_0^{eV} \rho_s(\epsilon)\rho_t(\epsilon - eV)d\epsilon$$

$$\propto |M|^2\int_0^{eV} \rho_s(\epsilon)\rho_t(\epsilon - eV)d\epsilon \tag{2.5}$$

As seen from the Equation (2.5), the tunneling current is actually determined by the convolution of the density of states of tip and sample. Since both $\rho_t(\epsilon)$ and $\rho_s(\epsilon)$ are in the formula Eq(2.5), the tunneling current is equally determined by the electronic structure of the sample as well as the tip.

Since the main purpose in STM to obtain the topography image of the sample surface, it is very important to find a configuration where the tip density of state $\rho_t(\epsilon)$ can be neglected. But unfortunately, in most cases the actual geometric structure of the tip is unknown leading to an unknown tip density of state. In 1983, Tersoff and Hamann reported a calculation using first-order perturbation theory [8] which gave an analytical result for the matrix element [3-4] for a heavily simplified tunneling system as a representation of the STM. In particular, they solved the problem for an atomically sharp tip which is terminated by one single atom at the end. This last atom, i.e. the one closest to the sample surface, mainly contributes to the tunneling process. The wave function of this atom is therefore described by a locally spherical s-type wave function. Thus the tip density of states near to the Fermi level is assumed to be constant, i.e. $\rho_t \cong const$.
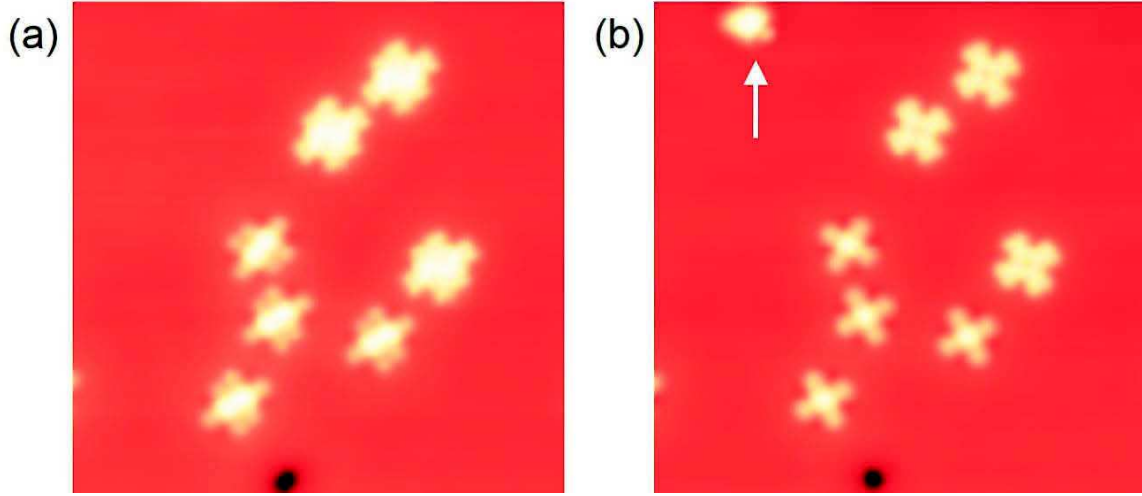
Figure 2.2 STM images of transition-metal phthalocyanines molecules on Ag(111) before (a) and after (b) modify the tip structure upon indentation on surface. These two images showing the influence of the tip structure on the sample topography image. STM image (a) is due to the convolution between the geometric structure of tip and molecules. While (b) is STM image of the adsorbed molecules taken by a sharp tip which is obtained by indentation on surface where indicated by the white arrow in (b).

In the limit of low-temperature and low-voltage: $k_B T \ll |eV| \ll \Phi_t$, Φ_s, and together with the approximation of tip as a tip of flat density of states, the Equation (2.5) for the tunneling current in STM becomes

$$I \propto |M|^2 \rho_t(0) \int_0^{eV} \rho_s(\epsilon) d\epsilon \qquad (2.6)$$

From the Equation (2.6) we can see that the tunneling current is determined by the integrated density of states, i.e. the total density of electrons, on the sample surface within the energy range $E_F < \epsilon < E_F + |eV|$. For a negative sample bias voltage ($V < 0$), the electrons tunneling from sample to the tip, the tunneling current measures the total filled states down to -eV below the Fermi level in the sample (see figure 2.1 (a)). For a positive sample bias ($V > 0$), the electrons tunneling from tip to sample, and the tunneling current measures the total empty states up to eV above the Fermi level in the sample (see Figure 2.1 (b)). In other words, the constant- current STM topography image measured at a fixed sample bias V can be thought as a contour of the local density of state $\rho_s(\epsilon)$ of the sample near the Fermi level rather than the real space topographic map of the surface.

2.2 Constant-current imaging mode

In this section we will explain how STM can measure the topography image of the sample surface based on the principle of tunneling current discussed above. By combining the tunneling current Equation (2.6) with the tunneling matrix expression in Equation (2.3), we find that the tunneling current I depends exponentially on the tip-sample distance z:

$$I(z) \propto e^{-2kz} \qquad (2.7)$$

where $k = \sqrt{2m\overline{\Phi}/\hbar^2}$ is an inverse of decay length and $\overline{\Phi} = \frac{\Phi_t + \Phi_s}{2} - \frac{eV}{2}$ is the mean barrier height. Typically 1 Å displacement in the tip-sample distance z yields one order of the magnitude change in the tunneling current $I(z)$, which corresponds to the decay length of $k \approx 1\,\text{Å}^{-1}$. With this level of sensitivity, the tunneling current can be used to control the tip-sample separation with the very high vertical resolution down to picometer (pm) precision.

When the sharp tip is scanned over the sample surface using a piezo actuator at a constant height, the surface topographic corrugations are reflected as changes in the tunneling current. This is called constant height imaging mode. There are some disadvantages of this constant-height mode. For example, the higher surface corrugations or even a small mechanical instability will lead to crash of the tip into surface. Thus, the constant-height imaging mode is only applicable for the extremely flat surface. A more commonly used imaging mode is constant-current mode. In this mode, during the tip scans over the sample surface, the feedback mechanism constantly adjusts the tip height, by approaching/withdrawing the tip towards/away from the sample, so that the tunneling current remains constant. The record of the feedback signal, as a function of the lateral position of the tip, gives a map of surface topography in real space. This way of imaging is called a constant-current topography mode.
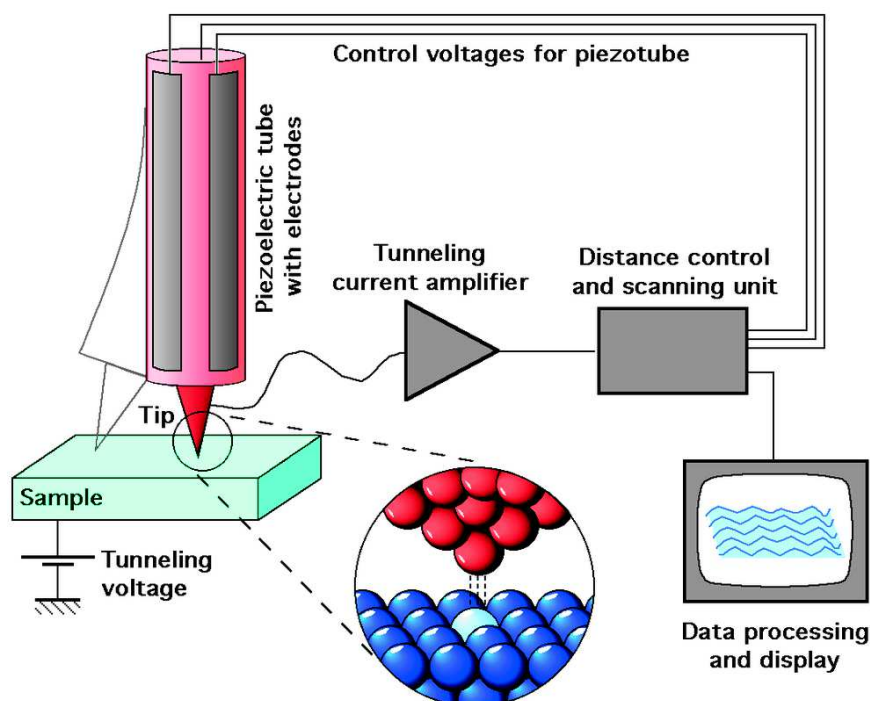

Figure 2.3 The scanning tunneling microscope: A sharp conducting tip is approached very close to the sample surface. Due to a bias voltage between tip and sample a tunneling current can be detected. Using a piezo electric scanner the tip is moved over the sample surface, resulting in a topographic image of the surface, based on the tunneling current signal.
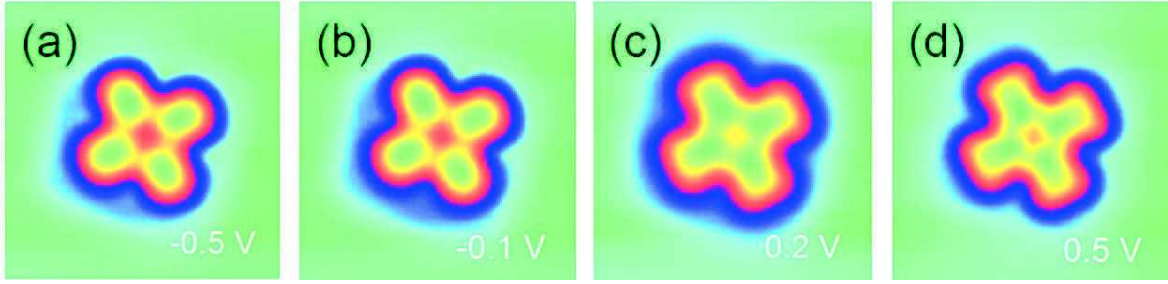
Figure 2.4 (a)-(d) Constant-current mode STM topographic images of a single CuPc molecule on Ag(111) at the indicated sample bias voltages.

2.3 Scanning tunneling spectroscopy

One of the most fascinating advantages of the STM is its capability to directly probe the electronic states of the sample [9-10], locally at the position of the tip. This technique which allows the local spectroscopic analysis of the adsorbates on surface is called scanning tunneling spectroscopy. In the below we will briefly review theoretical background of the scanning tunneling spectroscopy technique in STM.

As we seen in Section 2.1, the tunneling current in STM is mainly determined by the density of electronic states on the sample. Inversely, the information about the local density of states (LDOS) of the sample can be deduced from the current-voltage characteristics of STM tunneling junction. Since the tunneling current Equation (2.4) involves the integration over all the electronic states between the Fermi level and the applied bias voltage, the derivative of the tunneling current should be determined to get the electronic states at a given energy. More precisely, the relation between the differential conductance (dI/dV) and LDOS of the surface can be found by calculating the first-derivatives of tunneling current Equation (2.4) with respect to the applied bias voltage V. Assuming the tunneling matrix element $|M|^2$ stays constant in energy near the Fermi level (i.e. when $|eV| \ll \Phi_s, \Phi_t$, the tunneling matrix element changes negligibly) and denoting the mean transmission rate at the tip-sample distance z as $M(z) = \langle |M(z, \epsilon, V)|^2 \rangle$, we can rewrite the tunneling current Equation (2.4) as

$$I \propto M(z) \int_0^{eV} \rho_s(\epsilon) \rho_t(\epsilon - eV) d\epsilon \qquad (2.7)$$

Taking the first-derivative with respect to the bias voltage leads to

$$\frac{dI}{dV}(V) \propto \rho_s(eV)\rho_t(0)M(z) + M(z) \int_0^{eV} \rho_s(\epsilon) \rho_t'(\epsilon - eV) d\epsilon \qquad (2.8)$$

Here $\rho_t'(\epsilon - eV)$ is the first derivatives of the tip LDOS. The Equation (2.8) can be simplified by further assuming that the tip density of states $\rho_t(\epsilon)$ is constant in energy near the Fermi level (see Section 2.1). With this assumptions, the last integral term in thr

Equation (2.8) vanishes and only first term is left, then the differential conductance dI/dV become as following:

$$\frac{dI}{dV}(V) \propto \rho_s(eV)\rho_t(0)M(z) \propto \rho_s(eV) \tag{2.9}$$

Thus, the differential conductance dI/dV is proportional to the density of states $\rho_s(eV)$ of the sample. In other words, by recording the differential conductance dI/dV as a function of the sample bias voltage V, we can obtain the information about the local density of states $\rho_s(eV)$ on the sample. This operation mode of STM is called scanning tunneling spectroscopy (STS).

In principle the sample local density of states (LDOS) can be calculated numerically from the tunneling current in STM. However, the tunneling current is often too noisy to obtain a reasonable LDOS data with this numerical method. In most scanning tunneling spectroscopy experiments, therefore, the differential conductance dI/dV signal is detected with help of a lock-in amplifier, using AC modulation technique. To obtain the spectroscopic data with high signal over noise ratio, a small voltage modulation $V_{mod}\cos(\omega t)$ applied to the tunneling voltage V and it induces an in-phase modulated contribution to the tunneling current. This signal can be detected by lock-in amplifier and its amplitude for small modulation voltage is proportional to the first-derivative of tunneling current. This can be clearly seen from a Taylor series expansion of the tunneling current [3-4]:

$$I(V_0 + V_{mod}\cos(\omega t)) = I_0 + \underbrace{\frac{dI(V_0)}{dV}V_{mod}}_{lock-in\ signal}\cos(\omega t) + \frac{d^2I(V_0)}{dV^2}V_{mod}^2\cos^2(\omega t) + \ ... \tag{2.10}$$

From this equation it can be known that in a first approximation the amplitude of the current modulation with a frequency $f = \omega/2\pi$ at the tunneling voltage V_0 is proportional to the differential conductance dI/dV and therefore proportional to the LDOS on the sample. The second derivative d^2I/dV^2 is also important for studying the inelastic electron tunneling processes, e.g., excitations of vibration modes of the molecules [11] or spin flip of atoms [12]. The inelastic electron tunneling spectroscopy will be explained in detail in the next section.

Technically, the differential conductance dI/dV spectrum is acquired using the following method: the probe tip is positioned over the point of interest on the sample with chosen set point tunneling parameters (I, V) which determine the tip-sample distance z; then the tunneling voltage is ramped while the feedback loop is opened, i.e. the tip-sample distance z is kept constant; and the dI/dV signal is recorded over the desired range of voltages.

Another important point to should be mention here is that the role of the density of states on the probe tip. The sample spectra obtained with STM technique usually contain information about the electronic states of the probe tip. The STS spectrum would be a good approximation for the sample density of state only for the tip with a flat featureless density of states which has negligible contribution to the spectra measured on the sample.

In the STM experiments, the tip density of states is not always flat and constant, and thus it needs to perform a special indentation procedure over the clean surface area to control the condition of the probe tip. For the spectroscopic studies on the molecule or atom adsorbed on the noble metal surface, e.g. Ag(111) surface, the surface state measured on the clean surface can be used as a reference spectrum for the tip with flat density of state. Only the tip showing the expected surface state spectrum of bare noble metal surface can be used for probing the density of states of molecule/atom on the surface.
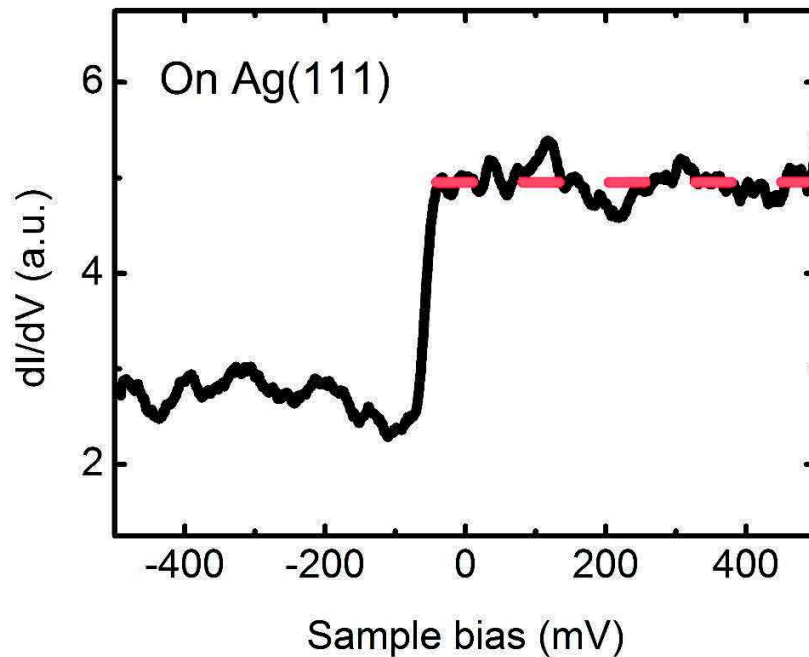

Figure 2.5 The surface state observed with scanning tunneling spectroscopy on a clean Ag(111) terrace at a temperature of T = 5K. The step-like increase is clearly visible in the local density of states at energies above the surface-state onset at ≈ 60 meV.

2.4 Inelastic electron tunneling spectroscopy

The STM is a technique not only capable to probe the local density of states of molecule/atom on surface, but also has ability to detect the excitation of vibration modes and spin-flip events in the molecule/atom [13-16], by the means of inelastic electron tunneling spectroscopy (IETS) [17]. For a review about the development of the inelastic electron tunneling spectroscopy with scanning tunneling microscopy (IETS-STM) see Refs.[15-16, 18]. In the below, we briefly introduce the principle of IETS-STM.

Usually, the energy of electrons is conserved during the tunneling process between the tip and a molecule adsorbed on surface. This elastic electron tunneling process probes the LDOS of molecule on a surface. More interesting, the tunneling electrons are also able to excite the vibration modes of molecule in the tunnel junction [14]. In the inelastic

electron tunneling process, the tunneling electrons loose partly its kinetic energy to excite the vibration modes of molecule and their final state is at a lower energy. Thus, there are two channels for the electron tunneling between tip and sample: one is the elastic channel with initial and final states at identical energies, and other one is the inelastic channel where the final state is at lower energy as shown in the Figure 2.6(a).
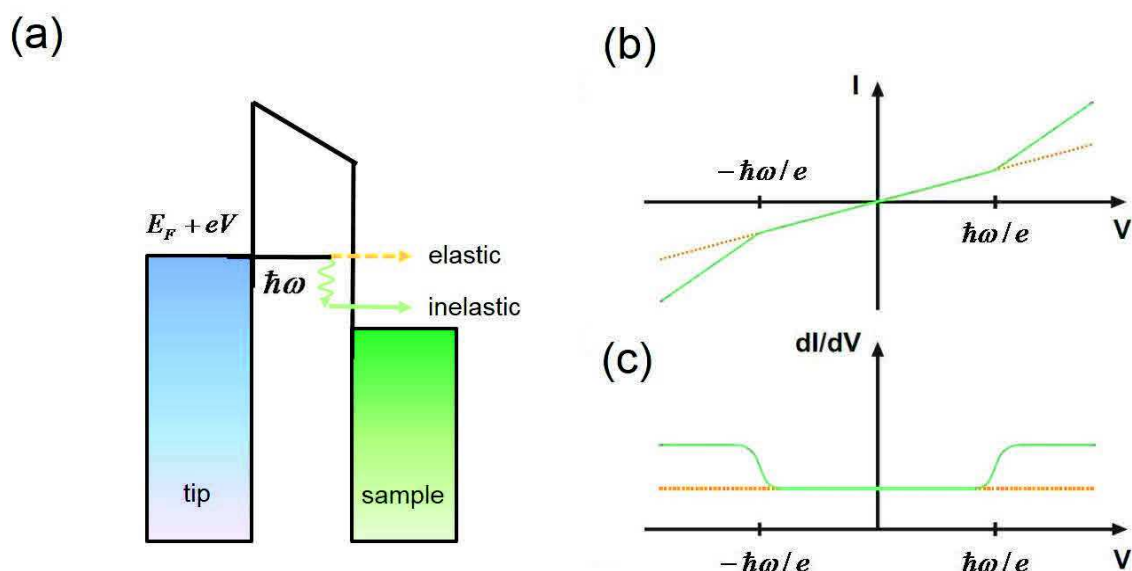

Figure 2.6 (a) Schematic drawing of the potential diagram of the STM junction illustrating the principle of the inelastic electron tunneling spectroscopy. Molecule vibration modes are excited by the inelastically tunneled electrons. the inelastic channel opens when the bias voltage reaches the threshold corresponding to the energy of vibration mode $\hbar\omega$. (b) the effect of the inelastic process on the current-voltage characteristics. The total current consists of inelastic and elastic contribution. The inelastic channel opens at the threshold voltage $V \geq \hbar\omega/e$. This is result in a step-like increase in the differential conductance dI/dV curve in (c). Figures are adapted from Ref.[19-20].

 The excitations of molecular vibration modes happen only when the energy of the tunneling electrons reaches to the energy of the vibration, i.e. when it meets the condition of $|eV| > \hbar\omega$, where $\hbar\omega$ is the energy of the molecular vibration mode. At this threshold energy, a new additional inelastic electron tunneling channel opens. This new inelastic channel leads to a step-like change in the differential conductance dI/dV signal at the threshold voltage $V = \hbar\omega/e$. Since the molecule vibration mode can be excited by the electron tunneling in both directions, another step occurs in the negative bias voltage symmetrically to the step in the positive bias (see Figure1(c)). In some case the change in dI/dV is usually too small to be detected, so that the information about molecule vibrations is extracted from the second derivative d^2I/dV^2 signal, where a clear peak ($V > 0$) and dip ($V < 0$) appears at the threshold voltages. In this thesis work, the observed molecule vibration signals are strong enough to detect with the differential conductance dI/dV measurements only, here we will not be going into details about the second derivative d^2I/dV^2 signal.

The influence of additional inelastic electron tunneling channel on the differential conductance dI/dV spectrum can be understood by considering a simple model of the tunneling current [17, 21-22]. Within this model we can describe the position of the inelastic conductance steps at the finite temperature, treating the electron-vibration interaction as a parameter. In the Section 2.1 (see equation (2.5)) it has been shown that the elastic tunneling current I_e linearly change with the applied bias voltage: $I_e = \sigma_e V$ in the limit of low-temperature and low-voltage. Above the threshold bias voltage of $V_{th} = \hbar\omega/e$, the excitation of vibration mode gives rise to the inelastic contribution to the tunneling current. The additional inelastic current I_i can be evaluated by considering the electron tunneling associated with releasing an energy of $E_i = \hbar\omega$, taking into account the Fermi-Dirac distribution for the electrons on the tip and sample. Then the total tunneling current [22] will be as following:

$$I = I_e + I_i = \sigma_e V + \frac{\sigma_i}{e}\int_{-\infty}^{+\infty}[\underbrace{f(\epsilon - eV + E_i)\big(1 - f(\epsilon)\big)}_{t \to s} + \underbrace{f(\epsilon)\big(1 - f(\epsilon - eV - E_i)\big)}_{s \to t}]\,d\epsilon \qquad (2.11)$$

where σ_e and σ_i are stand for the elastic and inelastic linear conductance, respectively, $f(\epsilon)$ is Fermi-Dirac distribution function as already defined in Section 2.1. The first term of the inelastic contribution describes the electron tunneling from tip to the sample ($t \to s$), and the second term corresponds to the tunneling from sample to the tip ($s \to t$). The inelastic linear conductance σ_i defines the strength of the molecule vibration and determined by the electron-vibration interactions.

Here we cannot use simplification as like we did in Section 2.1 and the integral expression in Equation (2.11) must should be solve analytically [17, 21] and we get:

$$I = \sigma_e V + \frac{\sigma_i}{e}\left(\frac{(eV - E_i)g(eV - E_i)}{g(eV - E_i) - 1} + \frac{(eV + E_i)g(-eV - E_i)}{g(-eV - E_i) - 1}\right) \qquad (2.12)$$

where function $g(\epsilon)$ denotes for $g(\epsilon) = exp(\epsilon/k_B T)$. The current-voltage curve for Equation (2.12) in the zero-temperature limit is shown in Figure 2.6(b).

The calculation of the first-derivative with respect to the tunneling voltage results in:

$$\frac{dI}{dV} = \sigma_e + \sigma_i\left(\frac{g(eV - E_i)\left(g(eV - E_i) - 1 - \frac{eV - E_i}{k_B T}\right)}{(g(eV - E_i) - 1)^2} + \frac{g(-eV - E_i)\left(g(-eV - E_i) + 1 + \frac{eV + E_i}{k_B T}\right)}{(g(-eV - E_i) - 1)^2}\right) \qquad (2.13)$$

This complex equation can be simplified to a more handy formula as following:

$$\frac{dI}{dV} = \sigma_e + \sigma_i\left(\hat{f}(-eV + E_i) + \hat{f}(eV - E_i)\right) \qquad (2.14)$$

where $\hat{f}$ is a modified Fermi-Dirac distribution: $\hat{f}(\epsilon) = (1 + \exp(\epsilon/1.46k_B T))^{-1}$. The resulting dI/dV curve exhibits a step-like increase in the conductivity symmetrically around E_F at $|V_{th}| = E_i/e = \hbar\omega/e$, as schematically shown in Figure 2.6(c).

2.5 Manipulation of single adsorbate

In the above we have considered the topographic and spectroscopic capabilities of STM for the investigation of atom/molecule on surface. Another important advantage of STM is the possibility to locally manipulate atoms or molecules by moving them with the tip. The idea using STM tip to move the single atoms was first introduced by Eigler and Schweizer [23], and realized by manipulation of the Xe atoms on Ni(110) surface. Since then STM becomes a powerful tool for the scientific research as it allows researcher to control the locations of single atoms and molecules, and most importantly to build the new artificial nanostructures with atomic precision [24-26]. The STM manipulation experiments are usually performed at low temperature, at which the thermal diffusion of atom/molecule over the surface is dramatically prohibited and it is possible to move single atom/molecule in a controllable way.

There are two methods for STM manipulation: the lateral manipulation and the vertical manipulation (see Figure 2.7(a) and (b)). In the vertical manipulation mode, the atom/molecule on the surface is transferred to the tip, then released in a desired position on the surface [27]. In the lateral manipulation, the tip is approached towards to atom/molecule and during movement the atom/molecule stays all the time on bounded to the surface.
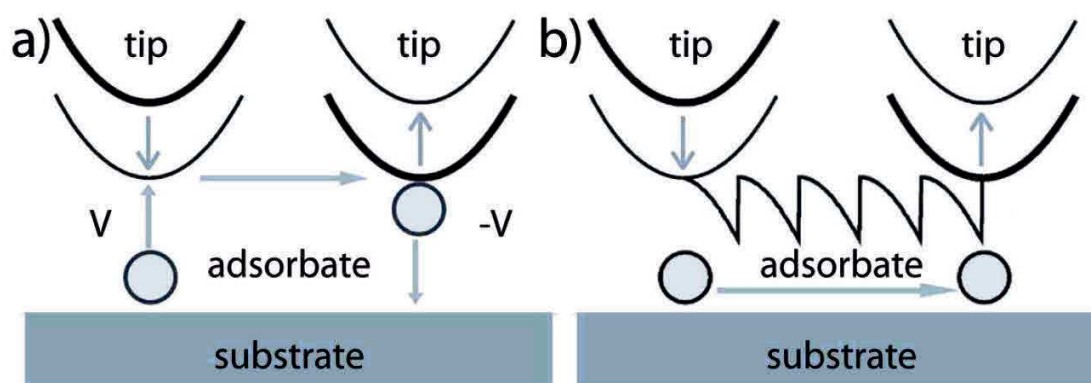

Figure 2.7 (a) Schematic view of the lateral manipulation procedure: firstly the tip placed above the atom/molecule to transfer it to the tip by a positive voltage pulse (V > 0) and release it in the final position by applying a negative voltage pulse (V < 0). (b) Schematic view of the lateral manipulation procedure: as a first step the tip is approached towards to the manipulated atom to increase tip-adsorbate interaction. In the second step the tip is moved parallel to the surface where the atom moves under the influence of the tip. At the final step the tip is retracted back to the normal image height thereby leaving the atom at the final location on the surface. Figures adapted from Ref.[28].

In the below, the lateral manipulation method will be discussed with an exemplary experiment done in this thesis work. A typical process for the lateral manipulation of a single atom is shown schematically in Figure 2.7(b) and an exemplary experiment for this is shown in Figure 2.8(a) and (b). The lateral manipulation with STM is performed by the following procedures: i) the set point voltage is decreased and simultaneously the set point

current is increased, so that tunneling gap resistance is reduced and the STM tip approaches to the atom/molecule that has to be moved. ii) then the feedback is turned off and the tip moves along the desired pathway (see the arrow in Figure 2.8(a)), so the atom/molecule moves along surface due to the interaction with the tip and continues up to the final chosen position. iii) the tip is retracted to a height characteristic to the normal imaging mode.
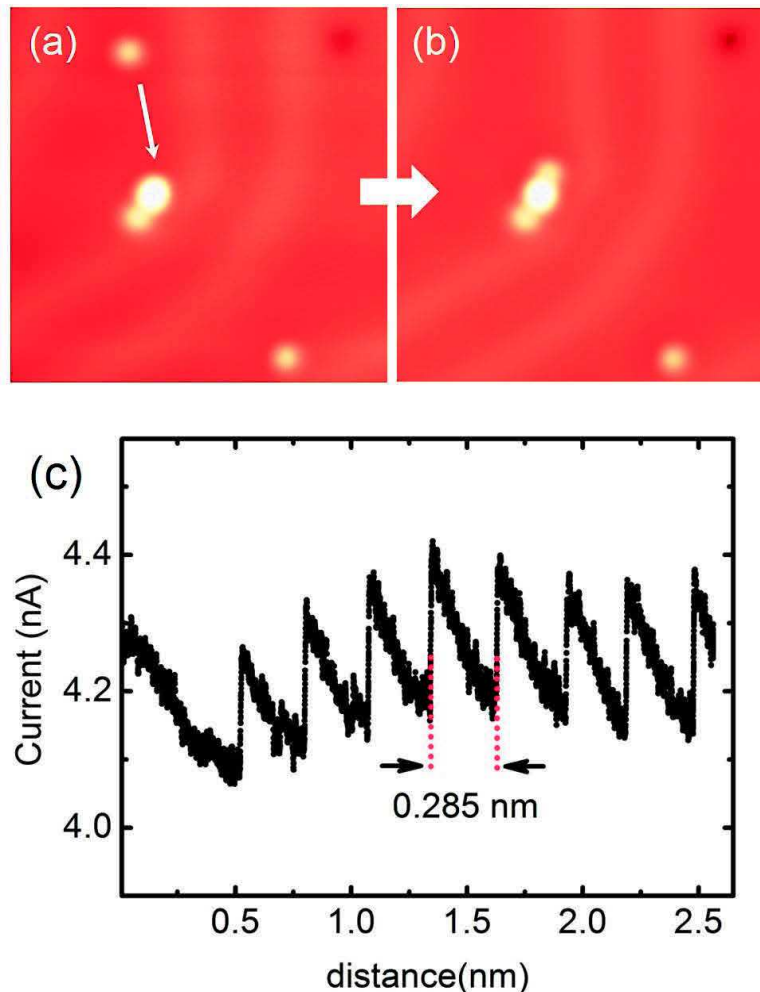
Figure 2.8 STM images before (a) and after (b) moving a single Cerium atom on Au(111) with an STM tip. (c) The lateral manipulation signal during the movement of a single Cerium atom along direction shown by the white arrow in (a). The periodic change of current signal as a function distance corresponding to the jump of the Cerium atom from one lattice site to the next separated by a distance of about 0.285 nm.

As we can see from Figure 2.8(c), the lateral manipulation signal is periodically changing with distance, this corresponding to the jump of Cerium atom from one lattice site to next site on Au(111) surface. Such a movement of atom is driven by the tip-atom interaction, such as van-der-Waals, chemical forces or the electric field, which are strong enough to move the atom/molecule along with the tip. The depending on nature of the tip-atom

interaction, three different lateral manipulation processes are possible: pushing, pulling and sliding. During a pulling process, the atom is situated just behind tip apex with respect to manipulation direction. The atom is manipulated via an attractive tip-atom interaction and follows the tip discontinuously by hoping from one site to next. During the sliding process, the atom remains bound under the tip apex without escaping from the defined trajectory. In this case, the tip-atom interaction so strong that tip and atom form a composed system, which scans the corrugation of the surface. During a pushing process, the atom is in front of the tip and it is pushed by the advancement of the tip apex due to a repulsive interaction. It is important to note that in the attractive manipulation mode like the pulling and sliding processes the atom first moves towards to the tip and then follows it, while in the repulsive mode like the pushing process the atom performs hopes away from the tip.

2.6 Experimental setup

 The experimental setup used in this thesis work is a low temperature STM designed by Createc Fischer & Co GmbH, Berlin, Germany [29]. The system operates in ultra-high vacuum (UHV) environment ($p < 1 \times 10^{-10}\,mbar$), and at the temperature conditions achieved with help of the liquid nitrogen and helium cryostats. Figure 2.9 shows the vacuum chambers of STM instrument. It consists of four chambers: preparation chamber, molecule evaporation chamber, a load-lock chamber and STM chamber. The UHV is achieved by an array of pumps: two primary and two turbo-molecular pumps connected to the load-lock and molecule evaporation chambers, two ionic and two titan sublimation pumps in STM and preparation chambers, and finally the cryostats in the STM chamber are acting as a cryogenic-pump.
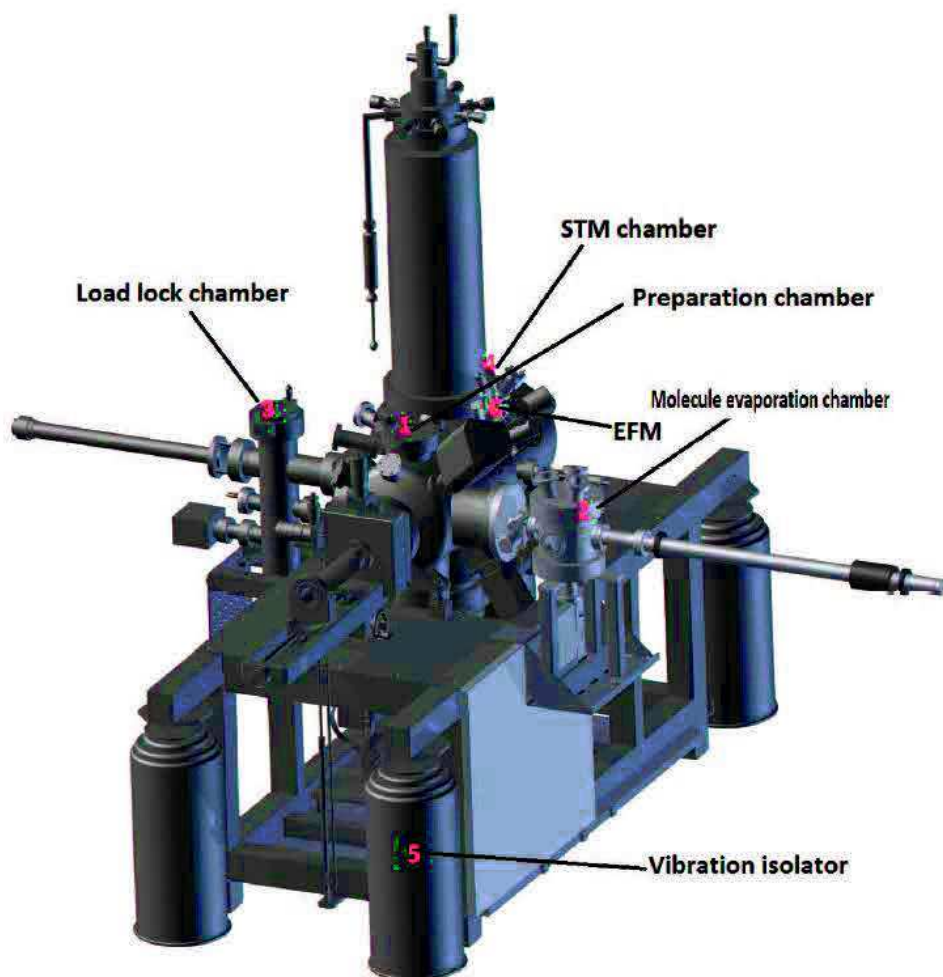

Figure 2.9 Perspective view of the UHV system with its components: (1) preparation chamber, (2) molecule evaporation chamber, (3) load-lock chamber and (4) STM chamber, (5) vibration dampers, (6) electron-beam evaporator.

The load-lock chamber is used to introduce the samples and tips from ambient pressure to UHV and vice versa. The evaporation chamber is specially used to the molecule evaporation. The preparation chamber is mainly used to the sample and tip preparations. This chamber is equipped with a sputtering ion gun used to sample cleaning, electron beam evaporator for the metal evaporation and manipulator for transferring and preparing of the sample. The STM chamber is the most important place where the STM head was mounted at the bottom of the cryostats and separated from the preparation chamber by a gate valve to keep clean it at a base pressure as low as $p = 1 \times 10^{-11} \, mbar$.

All the measurements in this thesis work were carried out with the low-temperature operating STM at liquid helium temperature i.e. 4.5 K. Such a low temperature operations are achieved by the use of a bath cryostat consists of two tanks. The outer tank can be filled up to 15 liters of liquid nitrogen, while the inner one is filled with 4 liter of liquid nitrogen or liquid helium. Both inner and outer cooling stages have radiation shields that enclose the STM head within it. Using this method the STM can be kept cold and perform measurements for the sample for 48 hours per refill of liquid nitrogen/helium on the outer/inner tank.

2.6.1 Tip and sample preparation

A metallic tip was used as a probe in this thesis work. Firstly the tungsten (W) wire was etched NaOH solution to make a tip apex with a small radius of curvature ($< 1\mu m$). Then it is fixed to the tip holder and transferred to the preparation chamber. The tip is cleaned by neon-ion bombardment and flashed up to about $500 \, °C$ in order to remove oxides from tip apex. After the tip was fixed to the piezo scanner of STM, it was further treated by the soft indentation on the crystal surface until to get a sharp tip terminated with a single atom. Such a tip can be confirmed by imaging of sharp features on surface, such a single atom and monatomic steps. For example when a single atom on surface is imaged as a perfectly circular shape, we can say that the tip is also terminated by a single atom.

Prior to the spectroscopic measurements on the interested objects on surface, it is necessary to conditioning the tip on the clean surface and the quality of tip should be verified by detection of the surface state. Only the tip showing the expected surface state spectrum of bare metal surface can be used as a probe for STS of adsorbates on surface.

Crystal preparation

Au(111) and Ag(111) the single crystals substrates were used in this thesis work. To achieve atomically clean metal surfaces the substrates were bombarded with Ne+ ion, which removes the impurities and adsorbates. Subsequently the surface roughness is smoothed by annealed up to 500 °C and cooled to room temperature. Such a several repeated cycles can efficiently remove contaminants on surface.

Molecule evaporation

 The homemade evaporator (see figure 2.10) is used to evaporate the molecules what we studied in this thesis wok. The manganese-phthalocyanines (MnPc) powders (purity $>$ 95%) is placed in a ceramic crucible, which can be heated by a tantalum filaments. The crucible temperature can be controlled with help of the K-type thermocouple fixed on the crucible. Before molecule deposition, the powder is degassed at least 24 hours. This molecule evaporator was calibrated at the evaporation rate of 0.2 ML/min at the evaporation temperature of 250 °C.
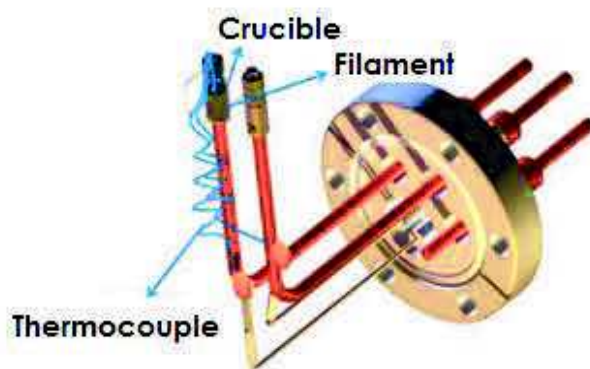

Figure 2.10 the homemade evaporator for the metal and molecule evaporations.

Atom evaporation

 Since the atom has higher kinetic energy, it easily diffuses to step edges or defect points on surface. To minimize the thermal diffusion of atoms, the atoms must be deposited on the cold sample. Thus we fixed the atomic evaporator at the cold stage evaporation position. With such a low temperature deposition method, we obayined isolated single atom on metal surface.

 Sample preparation

 In order to investigate the MnPc and CuPc molecule adsorbed on Au(111) and Ag(111) substrates we prepared several samples of varying molecular coverage. To avoid contaminations all samples are prepared in UHV condition ($p < 1\times10^{-9}\,mbar$). The molecules were deposited on the clean surfaces while kept at room temperature. The crucible evaporator was heated to $250℃$, which yields a deposition rate of approximately 0.1 monolayer per minute. In this way the samples with different coverage were prepared. All the STM measurement for these samples were performed at 5 K. The doping of molecules was prepared by deposition of cobalt atoms on the molecular monolayer, as a second step after molecule deposition. The cobalt atom was evaporated using an electron beam evaporator.

References

[1] C. J. Chen. Introduction to Scanning Tunneling Microscopy. Oxford University Press, New York, Oxford, 1993.

[2] C. Iacovita, Spin-dependent tunneling into single cobalt phthalocyanine molecules. PhD thesis, Universite de Strasbourg, 2009.

[3] J. Tersoff and D. Hamann. Phys. Rev. Lett. 50, 1998 (1983)

[4] J. Tersoff and D. Hamann. Phys. Rev. B 31, 805 (1985)

[5] N. D. Lang. Phys. Rev. B 34, 5947 (1986)

[6] J. Bardeen. Phys. Rev. Lett. 6,57 (1961)

[7] C. J. Chen. Introduction to Scanning Tunneling Microscopy. Oxford University Press, New York, Oxford, 1993.

[8] J. Bardeen. Phys. Rev. Lett. 6,57 (1961)

[9] R. M. Feenstra, J. A. Stroscio and A. P. Fein Sur. Sci. 181, 295 (1987)

[10] J. A. Stroscio and R. M. Feenstra Scanning tunneling microscopy, edited by J. A. Stroscio and W. J. Kaiser (Academic Press, San Diego, 1993).

[11] B. N. J. Persson, A. Baratoff, Phys. Rev. Lett. 59, 339 (1987)

[12] C. F. Hirjibehedin, C.-Y. Lin, M. Ternes et al, Science 317, 5842 (2007)

[13] G. Binning, N. Garcia and H. Rohrer, Phys. Rev. B 32, 1336 (1985)

[14] B. C. Stip, M. A. Rezaei, W. Ho, Science 280, 1732 (1998)

[15] W. Ho, J. Chem. Phys. 117, 11033 (2002)

[16] T. Komeda, Prog. Surf. Sci. 78, 41 (2005)

[17] R. C. Jacklevic and J. Lambe, Phys. Rev. Lett. 17, 1139 (1966)

[18] F. Moresco, Scanning probe microscopies beyond imaging, edited by P. Samori (Jhon Wiley & Sons, New York, (2005)

[19] M. Terns, Scanning tunneling spectroscopy at the single atom scale, PhD thesis, Ecole Polytechnique Federale de Lausanne, 2006.

[20] A. Strozecka, Electronic and vibrational properties of fullerenes and metallofullerenes studied by STM and STS, PhD thesis, Rheinisch-Westfalischen Technischen Hochschule Aechen, 2007.

[21] J. Lambe and R. C. Jaklevic, Phys. Rev. 165, 821 (1968)

[22] B. N. J. Persson, Phys. Scr. 38, 282 (1988)

[23] D. M. Eigler and E. K. Schweizer, Nature 334, 524 (1990)

[24] E. J. Heller, M. F. Crommie, C. P. Lutz, D. M. Eigler, Nature 369, 464 (1994)

[25] K. F. Braun, K. H. Reider, Phys. Rev. Lett. 88, 096801 (2002)

[26] H. C. Manoharan, C. P. Lutz, D. M. Eigler, Nature 403, 512 (2000)

[27] D. M. Eigler, C. P. Lutz, W. E. Rudge, Nature 352, 600 (1991)

[28] F. Moresco, Physics Reports 399, 175 (2004)

[29] http://www.createc.de

Chapter 3

Metal phthalocyanines on metal surfaces

Metal phthalocyanines are a family of molecules in which a central metal ion is surrounded by a planar macro-cyclic framework. They have attracted a great interest due to their unique functionalities which have potential applications in the future molecular electronic devices. In addition, their relatively simple and robust structure makes them a model system to study the interaction of metal-organic complexes with metal surfaces. Upon adsorption on a surface, the interaction of molecule with the metal surface tunes the electronic ground state of the molecules and governs all electronic and magnetic properties of molecule-metal interface. In this Chapter, we will present the adsorption configurations, the electronic and magnetic properties of individual manganese-phthalocyanine (MnPc) and copper-phthalocyanine (CuPc) molecules on Ag(111) surface by means of the low-temperature scanning tunneling microscopy and scanning tunneling spectroscopy (STM/STS) measurements.

3.1 Pristine metal phthalocyanine molecules

Metal phthalocyanines represents a well-known class of molecules with the organic semiconducting properties in the bulk and already used in industrial applications that includes the filed-effect transistors, gas sensors and solar cells [1]. They are also of particularly interest due to their unique functionalities which have potential applications in the future molecule-based electronic devices [2-3].

Metal phthalocyanines (MPc) consists of a phthalocyanines (Pc) ring that surrounding a metal (M) ion in its center (see Figure 3.1). These molecules are characterized by a rather simple and stable molecular structure with the square planar D_{4h} symmetry. Their electronic and magnetic properties are determined by the valence and spin state of the central metal ion. Therefore, these properties can be varied by the substitution of different metal atoms: M = Mn, Fe, Co, Ni and Cu. In the present chapter only the MnPc and CuPc compounds are will be reviewed since they are most interesting MPc molecules in the field of molecular magnetism.

Figure 3.1 Scheme of the metal-phthalocyanines molecular structure. The central metal atom (red) residing an environment of D4h symmetry.
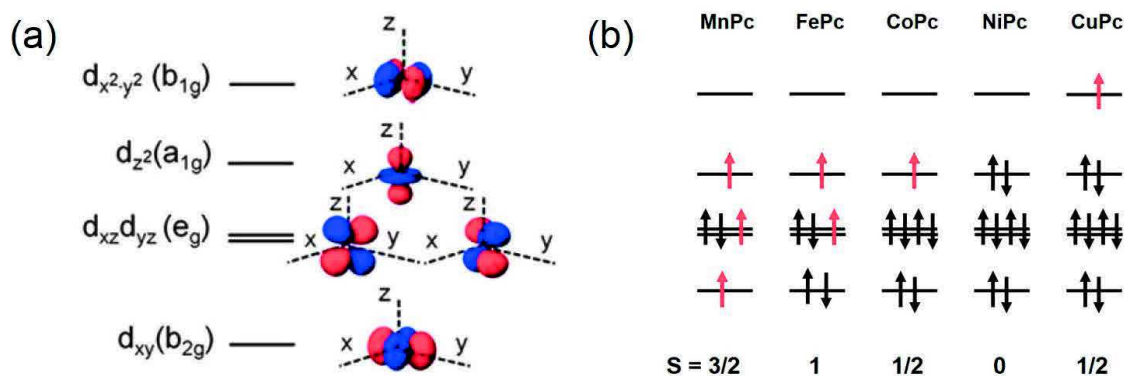

Figure 3.2 (a) The transition metal 3d orbitals with respect to the molecule axes. (b) The electron filling scheme for MPc molecules where the black arrows represent the paired electron spins and the red ones for the unpaired electron spin. In the below, the total spin due to the unpaired 3d electrons are indicated.

More precisely saying that the electronic and magnetic properties of MPc molecules depends basically on the electronic ground state of the central metal (M) ion. Since the molecular structure of MPc have a square planar D4h symmetry, under this symmetry group the M 3d states transform as b_{2g} (d_{xy}), b_{1g} ($d_{x^2-y^2}$), a_{1g} (d_{z^2}), e_g ($d_{xz}, d_{yz} = d_\pi$) (see Figure 3.2(a)). The different M atom substitutions supply the electrons that fill consecutively these orbital states (see Figure 3.2(b)). Depending on the symmetry and energy position, these electronic states of the central metal are hybridized with 2p states of the carbon and nitrogen atoms and generating the total molecular orbital (MO). The highest occupied and lowest unoccupied molecular orbitals (HOMO and LUMO) of the Pc ring are represented by delocalized a_{1u} and $2e_g$ π orbitals, respectively, with marginal contribution from the metal 3d states. The metal-related MO can be classified into two groups according to their parallel ($b_{2g}, b_{1g} = b_{\parallel}$) or perpendicular ($a_{1g}, e_g = d_{\perp}$) orientation with respect to the molecular plane, and, hence, to the substrate.

3.2 Adsorption of MnPc and CuPc molecules

The Figure 3.3(b) shows a large-scale overview STM topographic image of MnPc and CuPc molecules co-deposited on a Ag(111) surface. These phthalocyanine molecules are randomly distributed over the terrace at the low coverage and adsorbed on surface in the form of isolated molecule. In the STM image shown in Figure 3.3(b), the MnPc and CuPc molecules clearly appear as four-lobe patterns, but with distinctly different apparent heights at the molecule center. The MnPc molecule exhibit a bright protrusion at its center, while a small depression is found at the center of CuPc molecule as shown by the high-resolution STM image in the Figure 3.3(c). The difference between the adsorptions of MnPc and CuPc molecules on Ag(100) has been reported previously [4]. In addition, a different apparent height has also been observed in the previous STM studies on the other phthalocyanine molecule like cobalt-phthalocyanine (CoPc) and nickle-phthalocyanine (NiPc) [5].
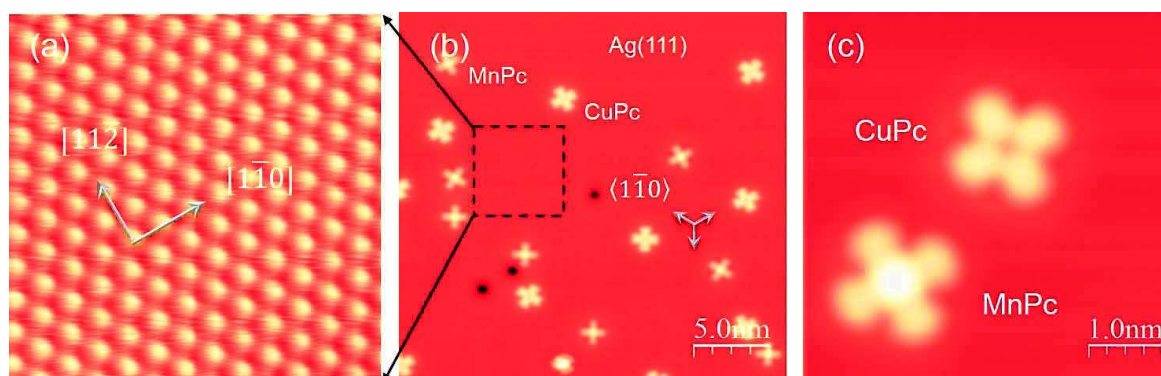

Figure 3.3 (a) Atomic resolution STM image of a free Ag(111) surface area, and the main crystallographic $[1\bar{1}0]$ and $[11\bar{2}]$ directions are shown by the arrows. This surface has a three-fold rotational symmetry. (b) STM image of MnPc and CuPc molecules co-deposited on Ag(111) surface. One of the molecular axes is aligned with the high symmetry direction $\langle 10\bar{1} \rangle$ direction of the underlying Ag(111) substrate. (c) The high resolution STM image of MnPc and CuPc molecules on Ag(111) surface.

Since these two species have identical molecular structure, the difference between adsorption is not related to the structure. Instead, it reflects the large or small degree of coupling between the central metal d orbital near the Fermi level and the substrate. The most probable metal d-orbital component contribute to the tunneling current at the central metal ion is the out-of-plane $d_{\perp}$ orbital due to their relatively large overlap with the tip wave functions. As we will show latter, the Mn $d_{\perp}$ orbital of MnPc is located just below the Fermi level and the electron tunneling through this orbital into the silver substrate is dramatically enhanced and leads to the appearance of a clearly visible protrusion over the Mn ion of MnPc molecule. On the contrary, the Cu $d_{\perp}$ orbital of CuPc is located more than 2 eV below the Fermi level [5]. This orbital is unable to participate in the tunneling current and the Cu ion appears as a small hole in the center of CuPc molecule as shown in Figure 3.3(c).

The four-lobe structure of the molecules in the STM topographic image (see Figure 3.3(c)) indicates that both, MnPc and CuPc molecules adsorb with the molecular plane parallel to the surface. This flat adsorption geometry of the molecules facilitates the bonding of both the central metal ion and the organic ligand to the substrate. From the STM image in Figure 3.3(b), we can identify three distinct molecular orientations rotated by 120° from each other for both, MnPc and CuPc molecules, which is consistent with the three-fold rotational symmetry of the Ag(111) surface. Moreover, the atomic resolution image of the bare Ag(111) surface, shown in Figure 3.3(a), reveals that the molecular axes are aligned along $[10\bar{1}]$ and $[1\bar{2}1]$ surface directions of the underlying Ag(111) substrate as shown in Figure 3.3(b).

The atomically resolved STM image of the surface after adsorption of the molecules enables us to determine more precisely the adsorption configuration of MnPc and CuPc molecules on Ag(111) surface. The superposition of a two-dimensional (2D) lattice with the atomically resolved substrate suggests that the MnPc molecule adsorbs with its central Mn ion on top of Ag atom, while the central Cu ion of CuPc is located on a hollow site of Ag(111) as shown in Figure 3.4(b) and (a), respectively. As mentioned above, the molecular axes are aligned with the high-symmetry $\langle 10\bar{1} \rangle$ and $\langle 1\bar{2}1 \rangle$ directions of Ag(111) surface. These adsorption configurations of the molecules correspond to the energetically most favorable interaction of MnPc and CuPc molecules with Ag(111) substrate at the experimental temperature of 4.5 K. The experimentally observed adsorption configuration of MnPc molecule was further confirmed by the density functional theory (DFT) calculation (see Figure 3.4(c)).
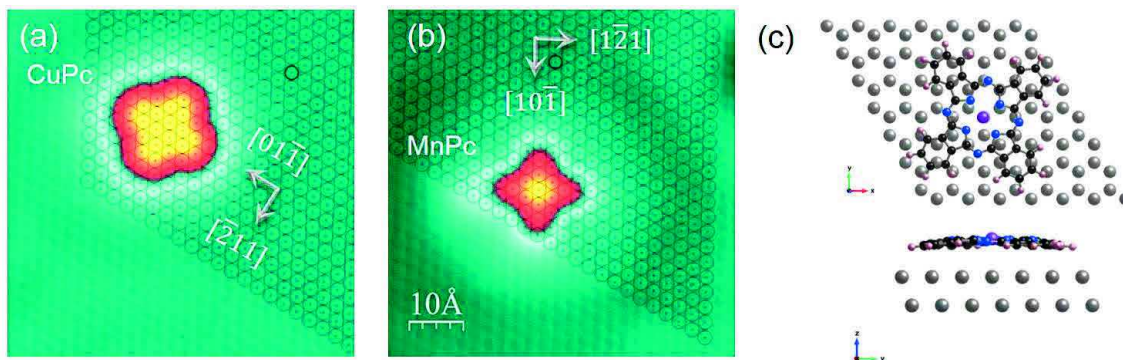
Figure 3.4 Atomic resolution STM of Ag(111) surface after adsorption of (a) CuPc and (b) MnPc molecules. The molecular axes are aligned with the high symmetry direction $\langle 10\bar{1} \rangle$ and $\langle 1\bar{2}1 \rangle$ directions of the underlying substrate. The circles represent a two-dimensional lattice super-positioned on the substrate surface. (c) Adsorption geometry (top and side views) of MnPc on Ag(111) calculated by the density functional theory.

A similar adsorption site has been found for MnPc on Pb(111), while the molecular axes are rotated by 15° with respect to the high-symmetry $\langle 10\bar{1} \rangle$ surface direction [6]. On Au(111), the molecular axes of MnPc are aligned with $\langle 10\bar{1} \rangle$ and $\langle 1\bar{2}1 \rangle$ surface directions,

while the metal center resides on a bridge site of the surface lattice [7]. However, our experimental observation is different from the recently published results for the same molecules adsorbed on Ag(100) [4]. In this publication, both MnPc and CuPc molecules are shown to adsorb to high symmetry positions of Ag(100) lattice, that is, the central metal ion is located on the Ag hollow site. While the molecular axes are rotated by ± 30° with respect to the substrate's ⟨110⟩ direction.

3.3 Spectroscopy of single molecules

The different adsorption behavior of MnPc and CuPc molecules hints a very different interaction with the substrate. In this section, we will therefore investigate the electronic structure of MnPc and CuPc molecules adsorbed on Ag(111) by the scanning tunneling spectroscopy (STS) measurements.

The dI/dV spectra of MnPc and CuPc molecules recorded by positioning the STM tip on the central metal atom (black curves) and on the benzene ring (blue curves) are shown in Figure 3.5(a) and (b), respectively. The MnPc center spectrum is dominated by a strong peak near to the Fermi level as shown in the upper panel of Figure 3.5(a), which originates from the Kondo screening channel of the Mn d orbital and will be discussed in the next section. Except for this pronounced peak close to E_F, the dI/dV spectrum taken at the MnPc center is rather featureless within this energy range.
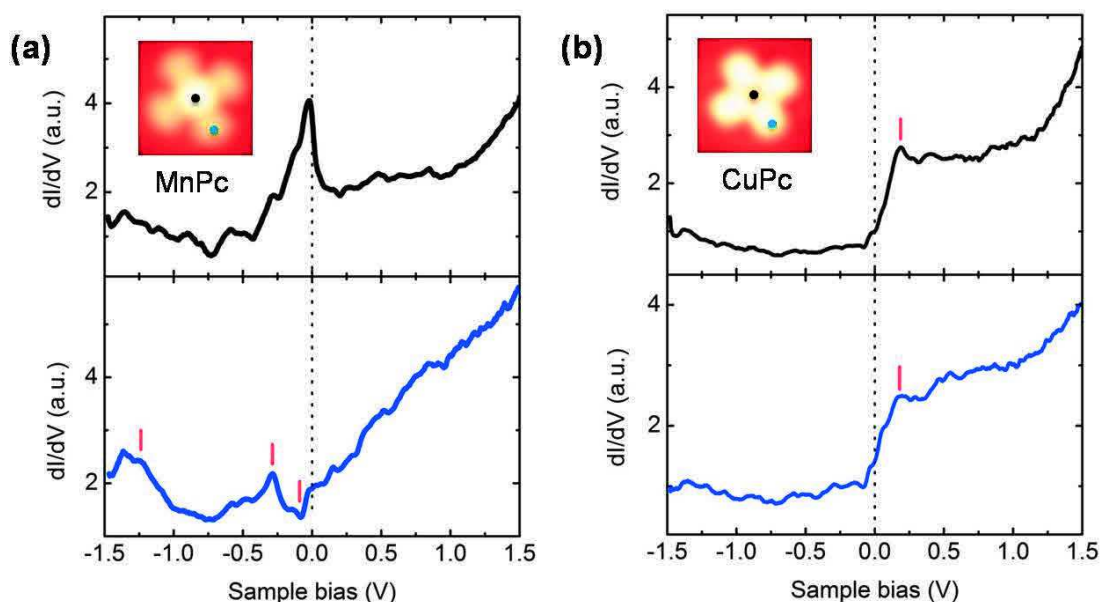

Figure 3.5 dI/dV spectra acquired on the metal center (black, upper) and benzene rings (blue, lower) of (a) MnPc and (b) CuPc molecules adsorbed on Ag(111) surface.

The MnPc ligand spectrum shows a dip-like feature at -0.1 eV, a broader peak at -0.28 eV and a wide feature at about -1.2 eV. The single MnPc molecule spectra of Figure 3.5(a)

are similar to the one for the other MPc molecules on Ag(100) substrate [5]. In contrast to MnPc, the CuPc molecule does not show any clear spectroscopic signatures except for a step-like feature just above the Fermi level. Moreover, the spectrum measured on the metal center and on the organic ligand of the CuPc molecule is essentially same as shown in Figure 3.5(b).

 The conductance mapping allows us to identify the molecular orbital belonging to the peaks. As shown in Figure 3.6(a), the dI/dV map of MnPc molecule recorded at -1.2 eV shows a dominant contribution at the organic ligands of the molecule. We attribute the broad peak feature at -1.2 eV to the spectroscopic signature of the highest occupied molecular orbital (HOMO) of MnPc molecule. The spatial distribution and the energy position of MnPc HOMO orbital is similar to the one found for other meta-phthalocyanine molecules [5], while the dI/dV map at -0.1 eV exhibit a spectral weight both on the metal center and at the organic ligands of MnPc molecule. Indeed, as shown in Figure 3.5(a) the dip-like feature at -0.1 eV in the MnPc benzene spectrum is located in the same energy range where the MnPc center spectrum shows a strong peak. In previous STM studies such a dip for other MPc molecule was related to a Fano line shape originating from a tunneling interference between the occupied state at the metal center and the organic ligand, analogous to the interference occurring between resonance and direct channels [5]. In the present case, the dip at -0.1 eV may originated from a similar tunneling interference mechanism.
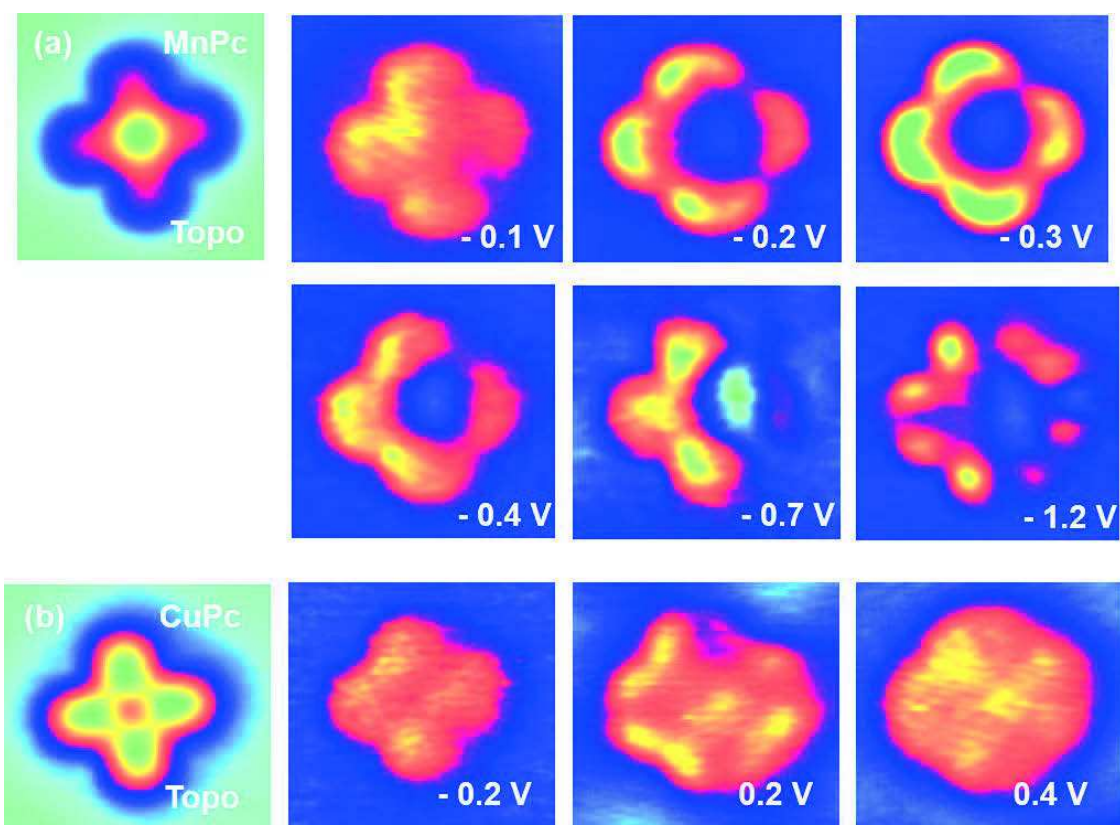
Figure 3.6 Constant-current dI/dV maps of (a) MnPc (b) CuPc at the indicated bias voltages. The topographic image obtained during the acquisition of maps is displayed on the left-hand side.

 The conductance maps of MnPc molecule at bias voltages around the peak at -0.28 V has slightly different intensity and spatial distribution compared with the dI/dV maps taken at -0.1 V and -1.2 V. The spatial distribution and the energy position of this peak is similar to that of the singly occupied molecular orbital (SOMO) with finite metal d state contribution [5]. The fact that, this peak is energetically located just below the Fermi level and spatially distributed over the organic ligand, indicates that this feature is closely related to the partially occupied ligand orbital of the MnPc molecule. Moreover, the ultra-violet photoemission spectrum of the MnPc thin film (~ 3 nm thick) showed a strong peak at a binding energy of 1.3 eV and a broader shoulder peak at 0.6 eV in the valence region close to the Fermi level [8]. The peak at the higher binding energy is the highest occupied molecular orbital (HOMO) state of MnPc molecule with the ligand (π) character in good agreement with our STM observation. The low energy excitation peak at binding energy of about 0.6 eV was attributed to a singly occupied molecular orbital (SOMO) as a hybrid state of Mn 3d and ligand π orbitals [8]. This indicates that the spectral weight and the conductance map signal for the MnPc molecule at a bias voltages between -0.7 V and -0.2 V originate from the singly occupied molecular orbital (SOMO). In addition, the peak at -0.28 V is one of the characteristic peaks of MnPc molecule independent of interaction with substrate, as we will see in the next Chapter such a peak still exists in the 2nd layer

MnPc molecule which is strongly decoupled from the substrate by the first monolayer of MnPc molecules.

In contrast to MnPc, the CuPc molecule conductance maps exhibit a spectral weight almost uniform over the molecule. The conductance map at 0.2 V is similar to the one for the same molecule on Ag(100) [5]. Based on a previous study, we attribute the step-like feature around 0.2 V to the interface state stemming from the hybridization of the unoccupied molecular orbital with the surface state of substrate.

3.4 Magnetic properties of MnPc molecule

The metal phthalocyanine (MPc) molecules exhibit unique functionalities which make them promising candidates for future applications in magnetic data storage or spin−based information processing. A particular attention has been paid to a thorough understanding of the interaction of 3d MPc molecules with metal surfaces and the resulting electronic properties and density of states around the Femi level. Especially the Kondo effect, i.e. the coherent screening of the molecular spin by the conduction electrons of the metal substrate may lead to the formation of a many-body singlet state, which gives rise to a resonant state close to the Fermi level in the energy spectrum of the system, have been intensively studied recently.

The scanning tunneling microscopy and spectroscopy (STM/STS) is a powerful technique to study the Kondo effect with high spatial and energy resolution for a single molecule adsorbed on the metal surface. The signature of the Kondo effect in an STM experiment is the appearance of a zero-bias anomaly in the differential conductance (dI/dV) spectra measured over the magnetic impurity. However, the Kondo resonance is rarely observed as a pure peak in the STM experiments. Indeed, the Kondo peak is detected as a Fano line shape in STS. The origin of the Fano resonance comes from quantum interference between the Kondo resonance and the conduction electron channels for an electron tunneling from the STM tip into the magnetic impurity. The energy width of the Fano resonance is directly related to the characteristic Kondo temperature of the system under the STM investigation.

In this section, we will explore and compare in detail the Kondo effect of MnPc molecule on the two different noble metal substrates like Au(111) and Ag(111) through the analysis of differential conductance (dI/dV) spectra close to zero bias. Firstly, we will present the Kondo effect of MnPc on Au(111) substrate as a reference spectrum for comparison with the STS result observed for MnPc on Ag(111) surface. Then, we will discuss in more detail the Kondo effect of MnPc molecules adsorbed on a Ag(111) substrate as the main topic in this section. These STM results provides us comprehensive understanding of the Kondo behavior of MnPc molecules on surfaces.

3.4.1 Kondo effect of MnPc on Au(111)

We will start our discussion with a well-known Kondo behavior of MnPc on Au(111) substrate. Figure 3.7(b) shows a typical low-temperature STM image of the MnPc molecules on Au(111) substrate at very low surface coverage. As shown in the STM image, the MnPc molecules adsorb face-on, showing a four-lob structure with a bright center on the Au(111) surface. The simulation of STM topographic images of MnPc molecule revealed that the bright protrusion at the center of MnPc is due to the d-orbital character of the Mn ion near the Fermi level [7]. The Kondo behavior of individual MnPc molecules adsorbed on the Au(111) was investigated by means of STS with high spatial/energy resolution, in the ±100 meV range.
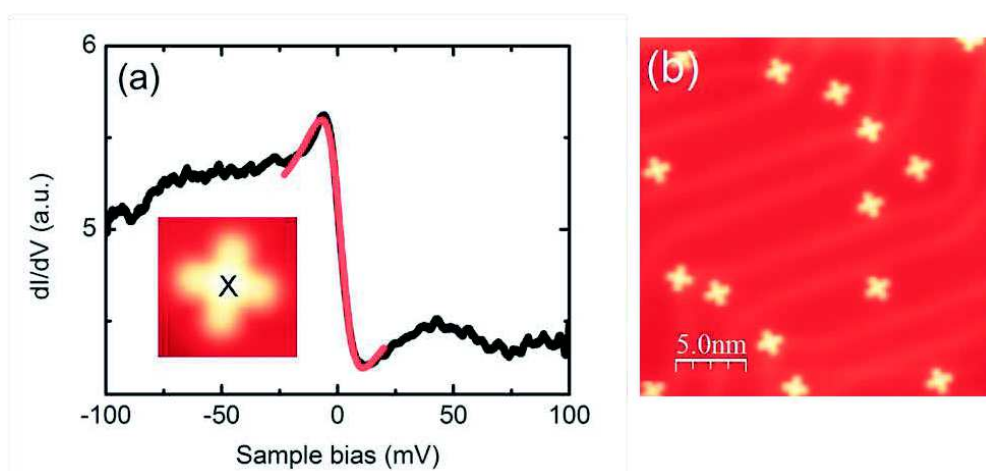

Figure 3.7 (a) dI/dV spectrum of MnPc on Au(111) measured at the position indicated in the inset, and the red line is Fano profile fit. (b) STM image of MnPc molecules on Au(111) surface.

The differential conductance (dI/dV) spectrum acquired over the central bright spot, i.e. corresponding to the central Mn ion, of MnPc on Au(111) consistently shows a pronounced step like feature at the zero-bias as shown in Figure 3.7(a). We observed the same spectroscopic feature for all the MnPc molecules, regardless of the different molecular azimuthal orientations and adsorption positions on the elbow site as well as on the face centered cubic (fcc) and hexagonal close-packed (hcp) regions of the herringbone reconstructed Au(111) surface. While the dI/dV spectrum recorded over the free Au(111) surface is featureless over the voltage ranges of interest here (not shown).

The step like feature in the dI/dV spectrum of MnPc/Au(111) has a very sharp energy width and is located at the Fermi level. In this system, a similar dI/dV spectrum has been reported in previous STM studies [7, 9]. More importantly, this characteristic spectral feature exhibited a linear splitting in the presence of an external magnetic field as well as a temperature dependent behavior. Based on these studies, we can therefore safely attribute the step like feature at E_F in our STS measurement on MnPc/Au(111) to the Kondo resonance due to the exchange interaction between the MnPc molecular spin and the itinerant conduction electrons of Au(111) substrate.

In order to extract the Kondo temperature corresponding to the resonance of the MnPc/Au(111) system, we fit the observed STS spectrum by a Fano function:

$$\frac{dI}{dV}(V) = a + b \cdot \frac{(q+\varepsilon)^2}{1+\varepsilon^2} \tag{3.1}$$

with

$$\varepsilon = \frac{eV - \varepsilon_0}{\Gamma}$$

Here, a is the background offset, b is the amplitude of the Fano function, q is the asymmetry factor of Fano line shape, ε_0 is the center of the Fano profile and reflects the energy location of the resonance. Γ is the half-width at half-maximum of the Fano profile and reflects the characteristic energy width of the Kondo resonance, i.e. $\Delta E = K_B T_K$ where T_K is the Kondo temperature. The relation between them is expressed as $\Gamma \approx k_B T_K$ where $T \ll T_K$. This relation is valid for our experimental temperature of 4.5 K.

The sharp feature observed at E$_F$ for MnPc/Au(111) is well fitted by a single Fano function with $\Gamma = 7.5 \pm 0.5\ \mathrm{meV}$ leading to the corresponding Kondo temperature $T_K = \Gamma/k_B = 85 \pm 5\ K$. This T_K value is in good agreement with previously reported results [7, 9].

3.4.2 Kondo effect of MnPc on Ag(111)

In the following we will discuss in more detail the Kondo behavior of MnPc molecules on Ag(111) as a main topic of this section. As shown in the STM image of Figure 3.8(a), the four-lobe MnPc molecules adsorb on the Ag(111) surface in the planar configuration. They show a bright center similar to the one for the same molecule on Au(111). However, the MnPc molecule exhibit a more complex spectroscopic feature when it adsorbed on the more reactive Ag(111) compared to Au(111) substrate.

The dI/dV spectrum measured over the bright center, corresponds to the central Mn ion, of the MnPc molecule adsorbed on Ag(111) surface. It exhibits a pronounced peak with an asymmetric line shape close to the zero-bias (see the black curve in Figure 3.8(c)). The spectra taken on the bare Ag(111) surface, a few nanometers away from the MnPc molecule, reveals no specific spectral feature except from a step-like increase in the differential conductance at a bias voltages of about -60 mV, characteristic for the onset of Ag(111) surface state. This reference spectrum taken on the bare Ag(111) surface confirms that the zero-bias peak is characteristic of the MnPc molecule on Ag(111) substrate.
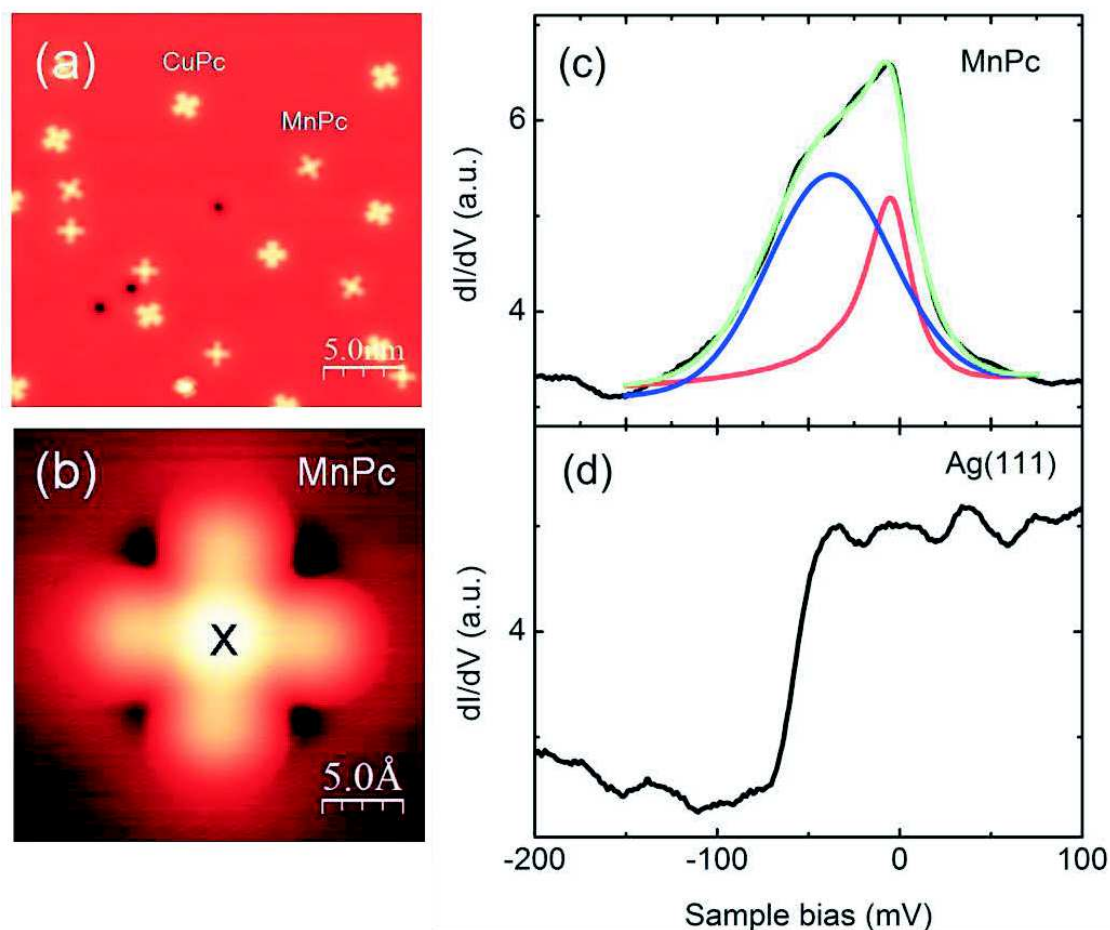
Figure 3.8 (a) STM image of MnPc and CuPc molecules on Ag111) surface. (b) High-resolution STM image of single MnPc molecule. (c) dI/dV spectrum of MnPc molecule measured at the position indicated in (b). The data (black) is fitted by the superposition (green) of a Fano (red) and Gaussian (blue) functions which are representing the Kondo resonance and an orbital state, respectively. (d) dI/dV spectrum taken over the bare Ag(111) surface.

The dI/dV spectrum of MnPc on Ag(111) is asymmetric with respect to the Fermi level and much stronger in intensity. This pronounced peak feature in dI/dV spectrum is so broad that it spans a bias voltages from -150 mV up to 50 mV and has an energy width of about 100 meV at the full-width at half-maximum (FWHM) as seen in Figure 3.8(c). Most importantly, the dominant feature of the spectrum is the sharp edge that drops as the voltage is increased over a width of about 30 mV (i.e. at FWHM) around V = 0, which corresponds to the Fermi level of the MnPc/Ag(111) system. We can consistently reproduce such kind of dI/dV spectrum for all the individual MnPc molecules on Ag(111) in several STM experiments with different metallic probe tips.

The strong peak around E_F in our STM experiment is similar to the one observed for the same molecule adsorbed on Ag(100) which has been reported recently [4]. In this publication, the observed pronounced spectroscopic feature near E_F was identified as a Kondo screening channel of the Mn d_{z^2} orbital. The MnPc molecule on Pb(111) surface

exhibits a characteristic sharp peak at the Fermi level, which was also attributed to the Kondo resonance. In the later system, the Kondo peak width strongly varies with Pb film thickness, which is due to the changes in the substrate's electron density induced by quantum confinement [10].

If we closely look at the zero-bias peak observed for MnPc/Ag(111) system, there are two important spectral features in the spectrum shown in Figure 3.8(c). First, the sharp edge at E_F is most likely related to a zero-bias resonance due to the Kondo effect, as observed in the previous studies for the same molecule on the different variety of metal substrates [4, 9-10]. Second, the spectral peak extends towards to the occupied states. This implies the existence of another molecular orbital spectroscopic feature which is superimposed on the zero-bias Kondo resonance and energetically located just below the Fermi energy.

In order to extract the Kondo resonance, we decomposed the zero-bias broad-peak observed for MnPc/Ag(111) into a narrow Fano profile at E_F and a broader Gaussian profile located just below E_F, which are representing the Kondo resonance and an occupied molecular orbital state, respectively. So that, the experimental spectral line shape is obtained as a sum of Fano and Gaussian functions as shown in Figure 3.8(c).

As shown in Figure 3.8(c), the Gaussian profile (blue) is largely overlapped by the Fano line (red). This agrees with our prediction for the existence of another orbital (i.e. closely related to Mn 3d state) that is superimposed on the Kondo resonance and energetically located just below the Fermi level. Therefore, a pure Kondo resonance peak is no longer discernible and the overall spectral feature of MnPc/Ag(111) system becomes very broad near to the Fermi energy as shown in the dI/dV spectrum in Figure 3.8(c). Indeed similar superposition of transition metal 3d orbital with their Kondo resonance were observed for both, transition metal atoms [11] and transition metal phthalocyanine molecules [12-13] on metal surfaces.

The spectral component described by a narrow Fano profile at E_F in Figure 3.8(c) has an energy width of $\Gamma = 15 \pm 1\,\mathrm{meV}$ at the half-width at half-maximum. The corresponding Kondo temperature is $T_K \approx \Gamma/k_B = 160 \pm 10\,K$. The Kondo resonance originates from the screening of the MnPc molecular spin by the conduction electrons from Ag(111) substrate. This T_K value is considerably higher than the one for MnPc on Au(111) discussed before in this section. However, it reasonably comparable with the experimentally measured and theoretically calculated Kondo temperature of $T_K = 120 \pm 15\,K$ obtained for the MnPc molecule on Ag(100) [4] and Pb(111) [6] substrates. In the last two cases, the Kondo resonance was well reproduced by the calculation of the spectral function of Mn 3d orbitals upon considering the many-body effects at the different temperatures. The calculation reveals a sharp Kondo peak right at the Fermi level for temperatures below 120 K and completely disappears at higher temperatures. This theoretical result strongly supports our interpretation of our own results. Moreover, the orbital-resolved spectral function shows that the Kondo peak originates from the Kondo screening channel of the Mn d_{z^2} orbital, whose hybridization to the substrate is much stronger than for the other d orbital components due to its shape and orientation. Based on this fact, it was emphasized that

the Kondo peak is strongly localized on the Mn ion of the MnPc molecule. In contrast, below we will show that both, the central Mn ion and the organic ligand actively participate in the Kondo effect of the MnPc molecule on Ag(111). Therefore, in this case it is more appropriate to conclude that the Kondo resonance at E_F originates from the screening of a collective molecular spin by the conduction electrons from the substrate.

In Figure 3.8(c), the spectral part corresponding to the broad Gaussian profile is located at about -40 meV below the Fermi level. Its full-width at half-maximum is $2\sigma = 70\ meV$, and likely originates from an occupied molecular orbital just below the Fermi level. It is important to notice that the half-width at half-maximum of the Gaussian profile is the same as its energetic position with respect to the Fermi level, and its high-energy tail is extending above the Fermi level. These characteristics imply that the occupied orbital is coupled strongly to the continuum states of Ag(111) substrate. The significant broadening of this orbital is caused by the strong hybridization with the substrate. This orbital assignment is in accordance with the previously reported experimental and theoretical calculation for the same molecule on Ag(100) substrate [12].

It is important to notice that the asymmetry factor obtained by fitting a Fano function i.e. $q = -5.1$, is very different from the positive value normally obtained for more conventional Kondo system [14]. Although similar negative q values were obtained in previous studies this point was never discussed properly. Here we will give a qualitative explanation for the negative Fano factor q. According to theory [15], the asymmetry factor q is expressed as:

$$q = \frac{V_{kt} + \sum_s V_{st} V_{Ks} P\left(\frac{1}{eV-\varepsilon_s}\right)}{\pi \sum_s V_{st} V_{Ks} \delta(eV-\epsilon_s)} \tag{3.2}$$

where s numbers the hybridized substrate and molecular states, except for the one Kondo state. From the above equation, the change of Fano q factor depends on the variation of the Kondo-orbital/tip matrix element V_{kt} and the substrate/tip matrix element V_{st}. The first addend in the numerator describes the direct tunneling from the tip into the Kondo state and the second addend represents the tunneling into the substrate with subsequent transfer to the Kondo state. In general, the second addend is considerably smaller than the first one. The denominator is determined by the direct tunneling into the substrate. This interpretation for the asymmetry factor is consistent with the low q values for the 3d transition metal atoms adsorbed directly on metal substrates [16]. For the case of low q values, the electrons tunnel predominantly into the continuum of the host metal's conduction band, because of the low extension of the d states of the impurities into the tunneling gap. Higher q values are found for increased tunneling directly into the magnetic atom [17]. One way to increase the accessibility of the d states of the magnetic impurities compared to the states of the supporting metal host is to incorporate the metal atom into an organic ligand [18]. In this way, the magnetic atom is lifted from the surface and the larger coupling between tip and Kondo state V_{kt} relative to V_{st} can explain by itself the large value of q, but not the change of its sign. However, the changing sign of q can be explained by the change of sign of the substrate/tip matrix element V_{st}. The Kondo-orbital/tip matrix element V_{Kt} at the same time changes smoothly, because it is determined

mainly by tunneling to the localized orbital in the central part of the molecule. This conclusion is directly supported by the spatial dependence of Kondo resonance that will be presented below.
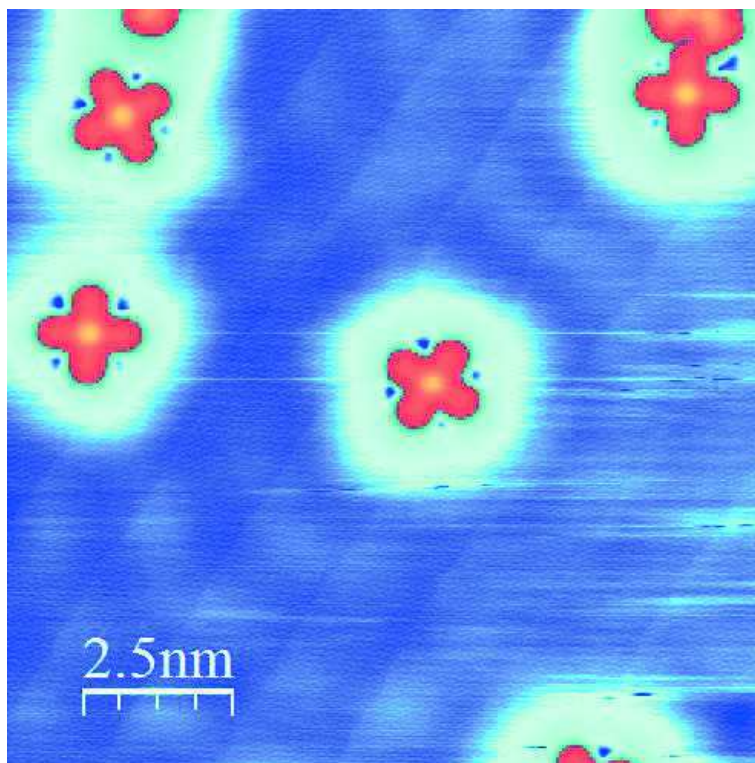

Figure 3.9 STM image MnPc on Ag(111) where an interference pattern around molecule was formed by the scattering of surface state electrons.

As a possible reason for the sign change of V_{st}, Meyer et al was suggested the interference of surface electron states at the molecule [19]. The onset of Ag(111) surface state is measured at the bias voltage of -60 mV, due to changes of the surface electronic properties near the molecular adsorbate, it could be influencing the electronic states of MnPc molecule near the Fermi level. This is evidenced by the interference patterns of surface state free electrons around the molecule (see Figure 3.9). The periodic changes of the surface electronic states on the Ag(111) surface thus influence the sign of q via the substrate/tip matrix element V_{st}. Accordingly, the sign of q would also change by the influence of organic ligand part on magnetic metal center.

A. Temperature dependence of Kondo resonance

Usually the STM measurements for Kondo resonance require a complete characterization of the Kondo peak. The important hallmarks of the Kondo effect are: (i) the splitting of the Kondo resonance under the external magnetic field and (ii) the

characteristic broadening and reduction of the Kondo resonance at increased temperatures. These unique characteristics makes the Kondo resonance totally different from any other source of zero-bias anomaly such as for example a low energy (3-4 meV) vibrational excitation at E_F due to the presence of hydrogen on the substrate [20].

Full characterizations of the Kondo resonance can be achieved by changing experimental parameters such as the magnetic field or the temperature. The magnetic flied dependence of Kondo resonance could be verified using the controllable built-in magnetic field of our STM. However, due to the small Bohr magneton value ($\sim 57.9 \mu eV/T$), a large magnetic field is mandatory to detect the splitting of the Kondo peak. In the case of MnPc/Ag(111) the broad resonance associated with a Kondo temperature of 160 ±10 K requires a magnetic field larger than 100 T to induce a measurable splitting. Therefore, we characterize the Kondo resonance of MnPc/Ag(111) system in terms of the temperature dependent behavior only.

dI/dV spectra were measured over the temperature range of T = 4.5 - 100 K. At each temperature the STM and sample were allowed to thermally equilibrate over several hours, and at least several spectra were acquired and averaged. Only five dI/dV spectra are shown in Figure 3.10, although tens of such spectra taken at different temperatures (see Figure 3.11) have been used to characterize the Kondo resonance in the MnPc/Ag(111) system. As shown in Figure 3.10, the dI/dV spectra measured for MnPc/Ag(111) at indicated temperatures reveal that the overall width of the peak, essentially the sharp edge at E_F, is significantly broadened as the temperature increased from 4.5 up to 100 K.
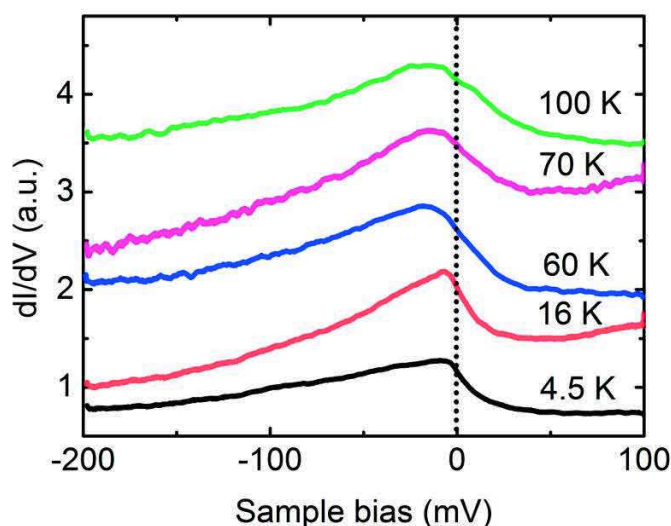
Figure 3.10 dI/dV spectra of MnPc on Ag(111) taken over the molecule center at the indicated temperatures.

We should notice that while the spectral line shapes exhibit a temperature-dependent electronic behavior, the relative overall amplitude between spectra does not reflect and intrinsic molecule properties. It depends on the use of different tips at different temperatures and on the presence of a constant multiplicative offset in dI/dV spectra.
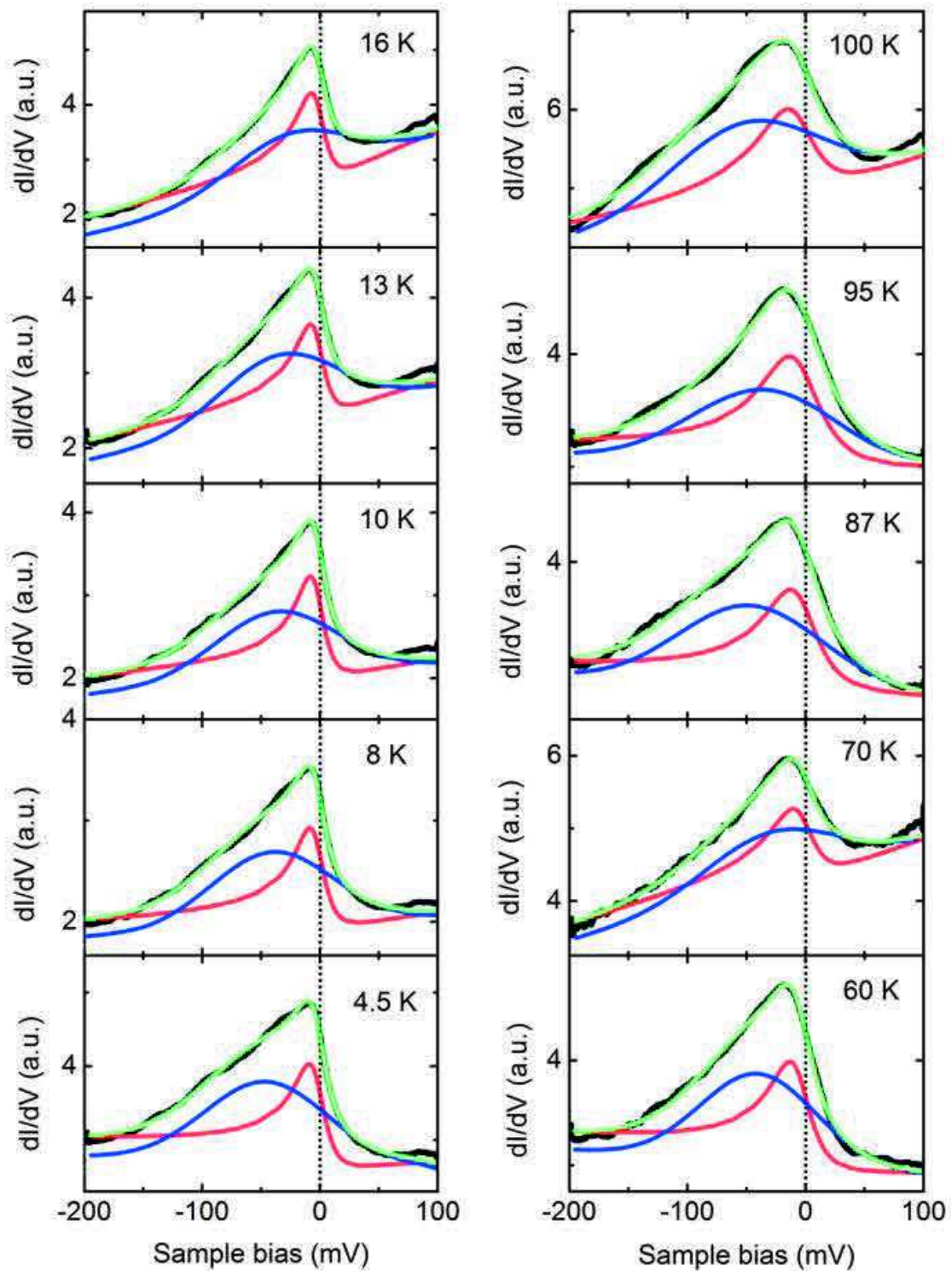
Figure 3.11 The dI/dV spectra of MnPc on Ag(111) at the indicated temperatures. Each dI/dV spectrum (black) is fitted by the superposition (green) of a Fano (red) and Gaussian (blue) functions which are representing the Kondo resonance and an orbital state, respectively.

In order to extract the width of Kondo resonance from the dI/dV spectra measured at different temperatures, a superposition of Fano and Gaussian functions is fitted to each experimental spectrum as shown in Figure 3.11. The Fano profile of the spectral features allows quantitative determination of the temperature dependence of the Kondo width for MnPc molecule adsorbed on Ag(111) surface. The Kondo width (HWHM) for the dI/dV spectrum at each temperature is determined by the Fano profiles (red lines in Figure 3.11). A plot of the HWHM as a function of the temperature from T = 4.5 K up to T = 100 K is shown in Figure 3.12. It can be seen from the data points that the width of the Kondo resonance increases quadratically with the temperature at low temperatures (for example below 50K), but becomes linear in temperature as the temperature is raised above 50 K.
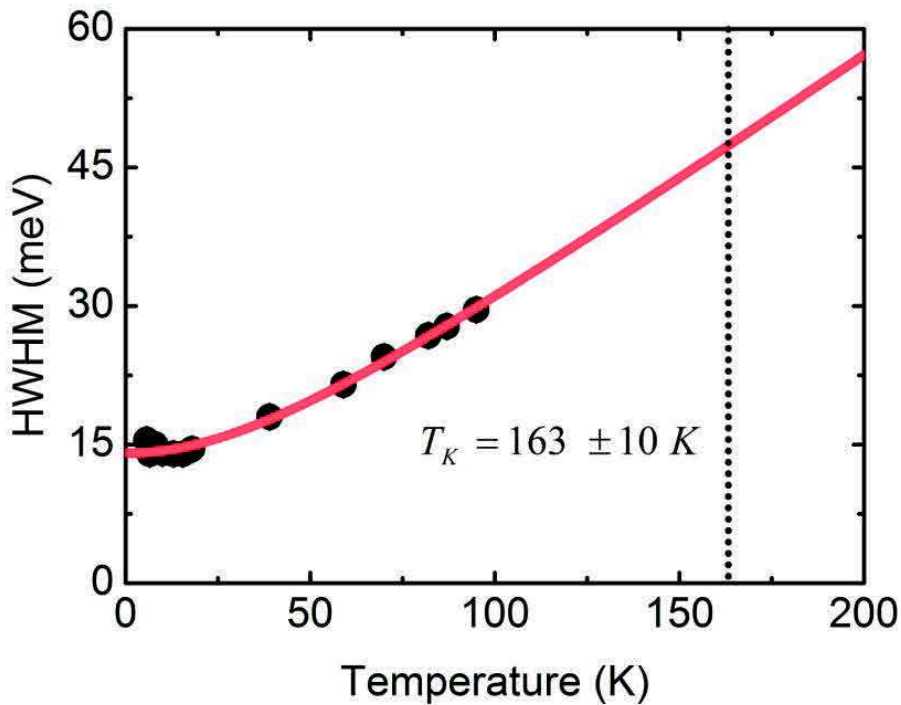
Figure 3.12 Temperature dependence of the half width at half maximum (HWHM) of the Kondo resonance: the black dots show the experimental data. The continuous red line shows the corresponding fits to the Fermi-liquid theory predicted temperature dependence.

Generally speaking, the width of Kondo resonance broadens with the temperature in a way that can be well described by the Fermi liquid behavior of the Kondo impurity [11]. The red line in Figure 3.12 shows a fit to the temperature dependent width of the Kondo resonance using the following equation developed from the Fermi Liquid theory:

$$2\Gamma = \sqrt{(\alpha k_B T)^2 + (2k_B T_K)^2} \qquad (3.3)$$

Here, Γ is the half width at half maximum of the Kondo resonance determined by the Fano profile, which is equal to $k_B T_K$ at $T = 0\ K$. From the theory, the parameter α should be 2π,

which is in good agreement with $\alpha = 6.43$ found here. A good fit gives a Kondo temperature of $T_K = 160 \pm 10\ K$ for MnPc/Ag(111) system. The dotted vertical line in Figure 3.12 indicates the location of T_K on the temperature axis and emphasizes that the measurements on MnPc/Ag(111) are within the Kondo regime.

As a conclusion of this section, it is found that the Fermi-liquid theory explains correctly the basic phenomenology of the temperature dependent Kondo resonance. This result confirms that the spectral feature at E_F is indeed a Kondo resonance which originates from the formation of a correlated many-body state in MnPc/Ag(111) system.

B. Tip-height dependence of Kondo resonance

In order to get a deeper understanding of the physical mechanism behind the Kondo resonance in MnPc/Ag(111), we will characterize the spatial dependence of the zero-bias peak using STM with high spatial resolution at the sub-molecular level. At first we test the basic trend of the zero-bias peak in the vertical spatial direction, to do this we measured the tip-height dependence of the zero-bias peak feature by acquiring dI/dV spectra over the central Mn ion of the MnPc molecule at different tip-sample distance which is finely controlled by varying the tunneling gap resistance. The tip-height dependence of the dI/dV spectra is shown in Figure.3.13. it should be emphasized that the shift in dI/dV is real.
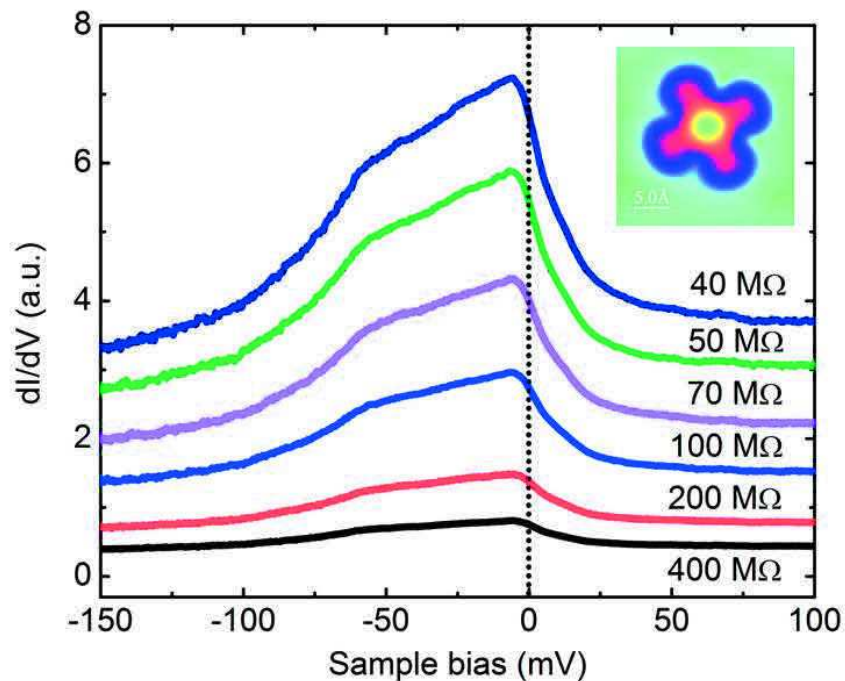

Figure 3.13 dI/dV spectra of MnPc on Ag(111) measured at the center of molecule (see inset) as function of tunneling gap resistance.

It is clear that the zero-bias peak intensity increases with decreasing tunneling gap resistance from 400 to 40 MΩ corresponding to a change in z-position of the STM tip of about $\Delta z = 1\text{Å}$. Despite the dramatic change of the zero-bias peak intensity, the characteristic spectral features and the width of the peaks remain the same for different gap resistance set points, i.e. different tip-molecule height. Fitting the data with a superposition of Fano and Gaussian functions reveals that the position of the orbital state and the Kondo temperature is the same for all the spectra in Figure 3.13. Therefore, the tip-height dependence of the peak features suggests that the STM tip acts as a real probe as expected and has no influence on the spectral characteristics of the system under investigation.

The tip-height dependence of the zero-bias peak at the center of MnPc molecule can be understood by considering the spatial symmetry and relative energy position of the Mn 3d orbitals in the MnPc molecule. Due to their relatively large overlap with the STM tip wave functions, the orbital that most significantly contributes to the peak observed at the molecule center is the out-of plane Mn $d_{\perp}$ orbitals. Furthermore, recent experiments and theoretical calculations showed that the perpendicular transition metal $d_{\perp}$ orbitals are systematically shifted towards the Fermi level as the filling of the 3d shell decreases [4, 12]. For MnPc on Ag(100) surface, it was found that the perpendicular Mn $d_{\perp}$ orbitals are located just below the Fermi level. We have observed a similar phenomenon for MnPc molecules on Ag(111) and the same orbital is also responsible for the bright protrusion at the center of MnPc in the STM topographic image. A similar conclusion was reported in the recent theoretical study of MnPc on Pb(111) [6].

In fact, among the five-3d orbitals of the Mn ion core of the MnPc molecule, the $3d_{xy}$ orbital is energetically the lowest lying one, whereas the $3d_{x^2-y^2}$ orbital is virtually empty and shifted to higher energies [4-6, 12]. The most relevant orbitals for the physics at the Fermi level are the three perpendicular orbitals, i.e. $3d_{z^2}$ and $3d_{yz/xz}$ doublet. The analysis of the hybridization for the Mn 3d orbitals in MnPc molecule adsorbed on Ag(100) substrates provides additional hints. This calculation shows that the three perpendicular orbitals are strongly hybridized around the Fermi level, due to the coupling of the d orbitals with the organic ligand, which, in turn, couple to the substrate. For symmetry reasons, the $3d_{xz}/d_{yz}$ orbitals strongly hybridize with the organic ligands while the direct coupling to the substrate is highly suppressed contrary to the $3d_{z^2}$ orbital. The parallel orbitals, i.e. $3d_{xy}$ and $3d_{x^2-y^2}$, on the contrary show no hybridization with substrate.

C. Spatial dependence of Kondo resonance

By probing the Kondo effect in MnPc using STM with high spatial and energy resolution within a single molecule, we investigated the influence of the organic ligand on the Kondo resonance peak. The lateral spatial distribution of the zero-bias peak feature within a single MnPc molecule was measured by acquiring dI/dV spectra at five different points with separated by a distance of ~2 Å from the molecule center, which corresponds to Mn

ion site, along the molecular axis towards to the molecule lobe, i.e., the benzene ring site (see Figure 3.14(a)). The spatial distribution of the zero-bias peak over the single MnPc along the molecular axe is shown in Figure 3.14(b).

As shown in Figure 3.14(b), the zero-bias peak is unchanged from location No.0 to No.1, which correspond to the central Mn ion and the nearest nitrogen sites, respectively (see Figure 3.14(a)). The latter one is ~2 Å distance away from the molecule center. The STS spectrum measured at the point No.2 shows a peak with weaker amplitude and broader width compared to the peak measured at the central Mn ion site. This peak eventually disappears at points No.3 and No. 4 near the benzene site.
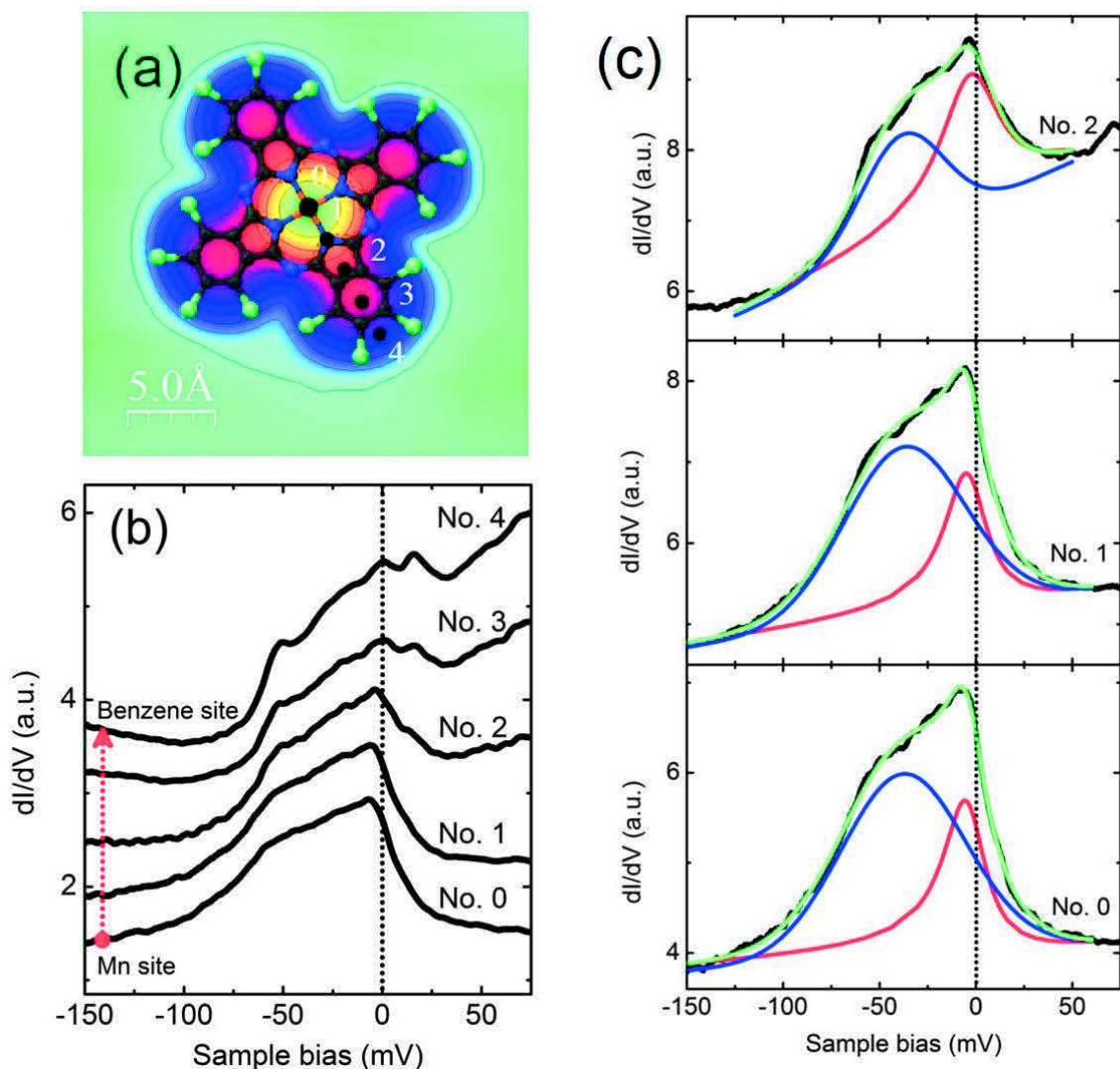
Figure 3.14 (a) STM image of MnPc on Ag(111), the molecule structure is superimposed on the image. The five equidistance points with uniform distance are numbered from 0 to 4 along the molecular axes. (b) STS spectra taken at black points in (a). (c) The curve fitting to the spectra No.0, 1 and 2 by the superposition (green) of Fano (red) and Gaussian (blue) functions which are representing the Kondo resonance and an orbital state, respectively.

As can be seen in Figure 3.14(c), the fitting of those two spectra by a superposition of Fano and Gaussian functions provides Fano line shapes with the same half-width at half-maximum value of $\Gamma = 13.5 \pm 0.2\ meV$. However, a small deviation of the line shape parameter is observed from $q = -7.6$ for the central Mn site to $q = -10.8$ for the pyrrole N site. The Kondo temperature is equal to $T_K = \Gamma/k_B = 160 \pm 10\ K$ on both, the central Mn ion and the nitrogen site in the organic ligand. This experimental result is different from the previous conclusion that the Kondo effect occurs only at the localized spin of the central Mn atom, and indicates that the organic ligand also contribution to the Kondo resonance [4, 6-7, 9].

The STS spectrum measured at the point No.2, corresponding to the carbon atom in the organic ligand, shows a peak with weaker amplitude and broader line shape compared to the one measured at the Mn ion. The fitting provides the following Fano parameters: $\Gamma = 18.8 \pm 0.2\ meV$ and $q = -25.4$ which are significantly different from the ones at the Mn center and on the pyrrole N atoms. The Fano width of this spectrum defines a Kondo temperature of $T_K = \Gamma/k_B = 220 \pm 10\ K$ larger than the one at the Mn ion. The higher Kondo temperature measured on the Pc ligand implies the formation of Kondo state by a strong hybridization of Mn d orbitals with the organic ligand.

Increasing further the distance from the center, the zero-bias peak feature significantly broadens at point No.3 and eventually disappears at point No. 4, which corresponds to the benzene ring of MnPc molecule. In addition, we observed similar spatial distribution over all the other molecular axes as well as over the low symmetry directions which makes an angle of 45° with respect to the molecular axes.

In the previous studies, the Kondo resonance in MPc molecules was generally believed to be localized at the metal center. Such an expectation is based on an assumption that magnetic properties of MPc at the metal surfaces depends almost exclusively on the ground state of the transition metal center, while the organic ligand part is regarded mainly as a mediator controlling the environment of the magnetic atom. Although this argument seems to be true for the case of CoPc on Au(111) where the appearance and disappearance of a Kondo resonance, i.e., the interaction of the magnetic Co ion with the substrate was controlled by chemically changing the organic ligand [21], the above experimental results show that the organic ligand can actively participate in the magnetism of the entire MnPc molecule. Indeed, a growing number of experiments indicate that the organic ligand directly affects the magnetism and transport properties of metal organic as well as purely organic complexes adsorbed on surfaces [5, 22-24].

Our STM experiment show that the Kondo resonance in MnPc/Ag(111) extends to the Pc ring that includes four pyrrole nitrogen atoms and four azamethine nitrogen atoms. The observed spatial extension of the Kondo resonance in MnPc/Ag(111) cannot be explained by the previous models based solely on the Mn 3d orbitals localized mainly at the molecule center. Interestingly this experimental result indicates that the π orbital spin of the organic ligand can actively participate in the formation of the Kondo resonance, and thus contributes to the magnetism of the entire MnPc molecule.

Recently reported synchrotron-based photoelectron spectroscopy measurements revealed that the charge transfer between MnPc and Ag(111) is a reverse transfer processes from the ligand to the substrate taking place at the interface with the substrate [23]. Therefore, the mechanism behind the observed spatial extension of Kondo effect in MnPc/Ag(111) might be different from the previously reported results. Recently, Minamitani et al [24] reported similar experimental results for the same molecule adsorbed on Pb(111) substrate. They found that the Kondo resonance is not just localized on the Mn ion but extends over the pyrrole ring in the Pc ligand and concluded that a "unique spin state" induced by the strong π-d interaction is responsible for the spatially extended Kondo effect.

3.5 Dehydrogenation of MnPc on Ag(111)

To further investigate the superimposed orbital state which is modeled by the Gaussian profile, we employed the dehydrogenation technique, which was introduced by Zhao and co-workers [21]. In their publication the controlled removal of the outer eight hydrogen atoms from CoPc molecules on Au(111) resulted in a systematic manipulation of the charge state of the molecule and eventually to the appearance of a Kondo resonance which is absent in the pristine molecules. To remove a particular hydrogen atom from the molecule, the STM tip is positioned over the corresponding ligand, the feedback loop is opened, the distance to the molecular lobe is increased by roughly 250 pm, and the bias voltage is increased to (3.2–3.6) V. The removal of a hydrogen atom is indicated by a sudden characteristic drop in tunneling current, which has been interpreted as originating from the dehydrogenated lobe bending towards to the surface. The Figure 3.15 shows the dehydrogenation of a single MnPc molecule on Ag(111) surface.
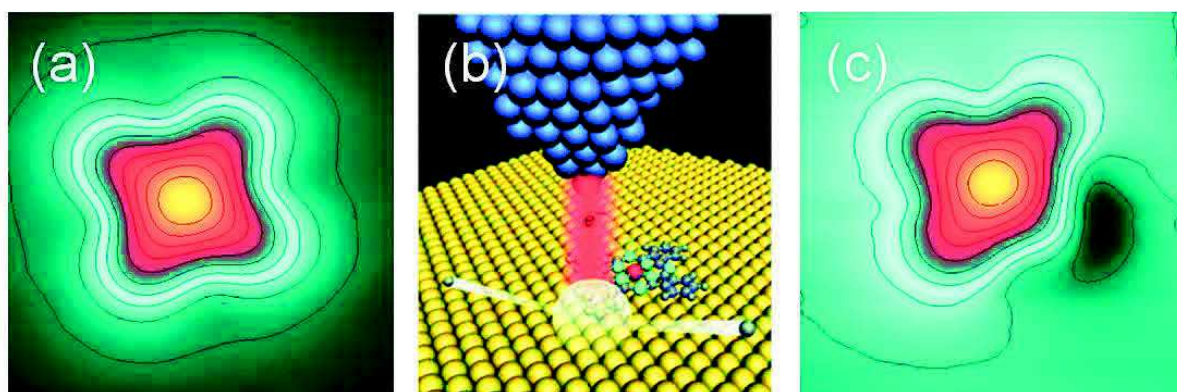

Figure 3.15 (a) STM image of the intact MnPc molecule on Ag(111) surface. (b) Schematic view of STM tip induced dehydrogenation of a single molecule. (c) STM image of the partially dehydrogenated MnPc molecule from which two hydrogen atoms in one lob are dissociated by the hot electrons injected by the STM tip as schematically shown in (b).

Figure 3.16 displays the experimental observations made upon dehydrogenation of MnPc molecule. While a topographic STM image of the intact molecule is shown in Figure 3.16(a), the Figures 3.16(b)-3.16(e) show the molecule after removal of two, four, six and eight hydrogen atoms, respectively (labeled -2H, -4H, -6H and -8H hereafter). The associated tunneling spectra measured above the molecule center are plotted as black lines in Figure 3.16(f).
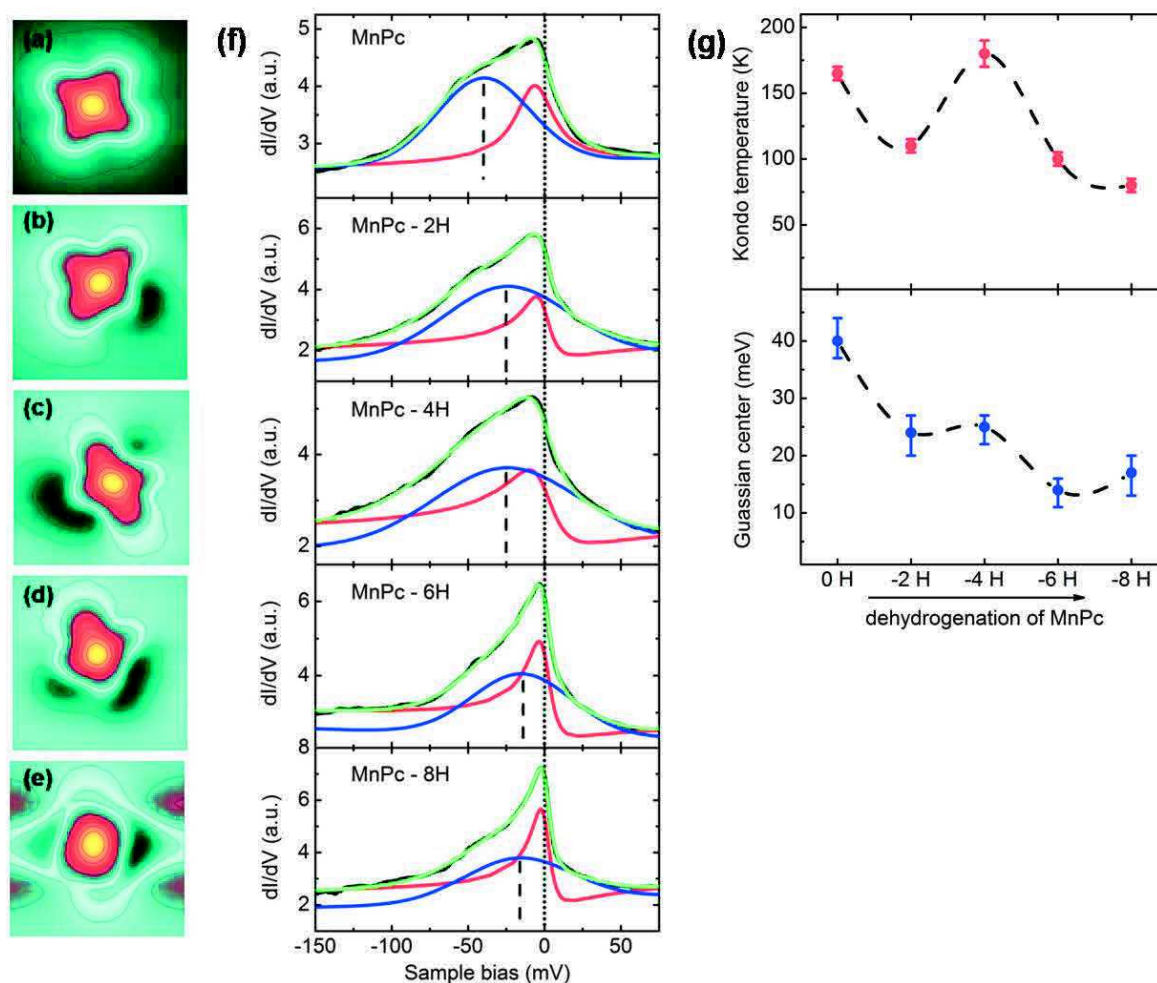
Figure 3.16 (a) STM image of the intact MnPc molecule. (b)-(e) the dehydrogenated series of MnPc molecule after removal of two, four, six and eight hydrogen atoms. (f) The corresponding tunneling spectra (black) measured above the molecule center are fitted by a superposition of (green) of a Gaussian (blue) and a Fano (red) profile that represent the Kondo and the orbital state, respectively. (g) The variations of the Kondo temperature (upper panel) and the Gaussian peak positions with the number of removed hydrogen atoms from MnPc molecule.

We have observed six distinct effects: (i) By looking at the contour lines, which are equally spaced from each other in height, a downwards bending of the dehydrogenated lobes can be recognized. (ii) This bending is accompanied by a depression in the substrate close to the dehydrogenated lobe, which appears as a kidney-shaped dark lobe in the images. This effect allows for the most precise determination of the position of the removed

hydrogen atoms. (iii) As dehydrogenation progresses the apparent height of the central Mn ion increased about ~0.58 Å after the removal of 8 hydrogen atoms compared with the intact molecule. (iv) The series of tunneling spectra obtained during this dehydrogenation series of MnPc reveals that the width of the zero-bias peak decreases very significantly from the intact MnPc molecule (Figure 3.13(a)) all the way to the MnPc − 8H molecule from which eight hydrogen atoms have been removed (Figure 3.13(e)). (v) As the number of removed hydrogen atoms increases we observe a gradual shift of the peak that originates from the molecular orbital state towards the Fermi level. This trend is highlighted by dashed vertical lines in Figure 3.16(f) which reveal a shift of the peak position from $E − E_F = −(40 \pm 5)$ meV for the pristine MnPc molecule to $−(15 \pm 5)$ meV for the MnPc − 8H after the removal of eight hydrogen atoms. The shift of the peak center with the number of removed hydrogen atoms is plotted in the lower panel of Figure 3.16(g). (vi) At the same time, starting from the intact MnPc molecule with $T_K = (165 \pm 10)K$, the Kondo temperature is reduced down to $T_K = (80 \pm 5)K$ for the MnPc − 8H molecule with a total of eight hydrogen atoms removed, while the MnPc - 4H molecule shows a maximum Kondo temperature of $T_K = (180 \pm 10)K$ which is even higher than the one of the intact MnPc molecule. The variation of the Kondo temperature with the number of removed hydrogen atoms is plotted in the upper panel of Figure 3.16(g).

Kugel and coworkers observed similar effects after dehydrogenation of the same MnPc molecule adsorbed on Ag(100) substrate [12]. In this publication the physical origins and consequences of effects (i) and (ii) were explained by the theoretical calculations. The downwards bending of the partly dehydrogenated lobes was nicely reproduced by the structural relaxations within density functional theory (DFT) by comparison of a complete molecule with the molecules from which two, four, or eight outer hydrogen atoms have been removed. They showed this structural relaxation leads to Ag 4s charge redistribution of the substrate atoms that participate in the bond to the molecular arm. It is mainly driven by the stronger hybridization between the Ag 4s and the C sp orbitals. According to their calculations the Ag 4s density of states at the Fermi level drops to about half the value as compared to an equivalent Ag atom placed under a non-dehydrogenated arm of the molecule. These theoretical results can also reasonably well explain our experimental observations of depression formation close to the dehydrogenated arm in Figures 3.16(b)-3.16(e).

Their DFT calculations explained that the increase of apparent height of the central Mn ion was a side effect of the dehydrogenation-induced bending of the molecule. Their theoretical calculation showed an increase of surface-Mn distance of about 0.37 Å for MnPc-8H molecule compared to the intact MnPc. This supports our STM observation of increased apparent height of the central Mn ion of the dehydrogenated molecule. As a consequence of increasing of surface-Mn distance induced by dehydrogenation, the hybridization between the molecular Mn d orbital and the substrate's itinerant conduction electrons reduce significantly and this causes the decreasing width of the zero-bias peak measured above the Mn center of molecule.

More importantly, observations (iii) and (vi) directly suggest that the orbital state and the Kondo resonance are related to the perpendicular Mn $d_\perp$ orbitals of MnPc molecule. This experimental conclusion is in good agreement with the analysis of hybridization function for the Mn 3d orbirals in MnPc molecule adsorbed on Ag(100) and Pb(111) substrates [4, 6, 12]. Particularly, the DFT calculations combined with a five-orbital Anderson impurity model for MnPc/Ag(100) system revealed that the Kondo resonance in MnPc originated from the screening channel of Mn $3d_{z^2}$ orbital [4]. The superimposed orbital close to the Fermi energy again stems from the $3d_{z^2}$ orbital of MnPc itself [6].

With the dehydrogenation process the apparent height of the central Mn ion increases, this leads to the observed reduction of the Kondo temperature from $T_K = (165 \pm 10)K$ for the intact MnPc molecule down to $T_K = (80 \pm 5)K$ for the MnPc – 8H molecule with all the eight hydrogen atoms removed. These experimental observations also corroborate that the Kondo effect originates from the coherent screening of the Mn $3d_{z^2}$ orbital, as showed in theoretical calculations. The maximum Kondo temperature of $T_K = (180 \pm 10)K$ for MnPc - 2H molecule might be result of the special molecular structure and stronger hybridization with the substrate.

In a simple model of the Kondo effect, i.e. the one band case with a flat bath [25], the Kondo temperature T_K is given by the following formula:

$$k_B T_K = \frac{\sqrt{\Delta_d U}}{2} exp \left(\frac{\pi \varepsilon (\varepsilon + U)}{\Delta_d U} \right) \tag{3.4}$$

where U is the Coulomb repulsion energy between singly and doubly occupied states, ε is the energetic level of the singly occupied state, and Δ_d is the substrate-induced broadening of these states.

From the above discussions and Kondo temperature T_K for the simple Kondo model, we can conclude that the significant reduction of the Kondo temperature of the dehydrogenated MnPc molecule is mainly due to the reduced hybridization of the Mn $3d_{z^2}$ orbital with the Ag(111) substrate and is not due to dehydrogenation induced effects.

3.6 Kondo effect of CuPc on Ag(111)

In this section, we will focus on the low energy spectroscopic properties of CuPc molecule with special adsorption configuration. Figure 3.17 shows a large-scale overview STM topographic image of MnPc and CuPc molecules on Ag(111) substrate.

On the flat terrace of Ag(111) substrate, both MnPc and CuPc molecules adsorb with the flat lying configurations, while the CuPc molecule preferentially adsorbed on the monatomic step with the non-planar configuration (see Figure 3.17). In this configuration, the CuPc molecule is anchored with one lobe on the upper terrace, while other three lobes are resting on the lower terrace. Such a CuPc molecule adsorbed at the monatomic step exhibit many characteristic signatures of low energy excitations around the Fermi level, which are absent for the CuPc molecule adsorbed on the flat terrace.
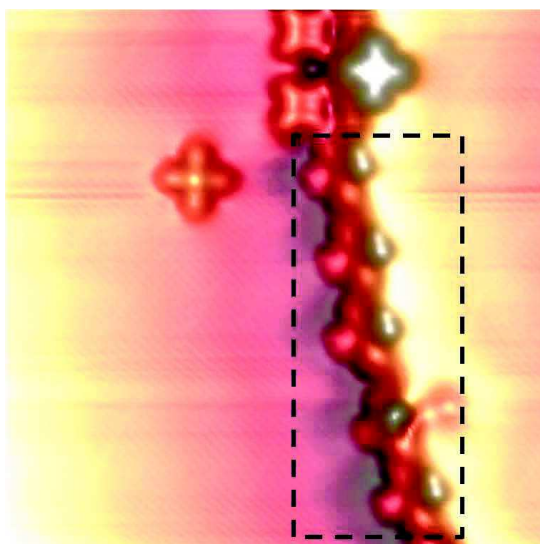

Figure 3.17 STM image of CuPc molecules adsorbed on the monatomic step edge are indicated by the dashed rectangle.

The CuPc molecule adsorbed on the Ag(111) terrace exhibit a flat featureless dI/dV spectrum over the metal center and on the benzene site (see Figure 3.18(a) and (c)). This result indicates that the Kondo interaction between the CuPc molecule and the Ag(111) surface is either absent or too weak to be observed at our experimental temperature of 4.5 K. The flat spectrum was also obtained for the CuPc adsorbed on Au(111) [26], for which it was concluded that the interaction between the localized spin in Cu d state and the substrate is too weak to observe the Kondo effect at 5 K. This interpretation has been supported by the theoretical results showing that the magnetic structure of CuPc is hardly affected by the substrate due to the weak coupling of the d-orbital spin to the metal surface. This interpretation seems to be valid also for the present case of CuPc/Ag(111). Thus we attribute the absence of Kondo peaks for CuPc on Ag(111) to the very weak coupling between the CuPc molecule spin and the substrate.
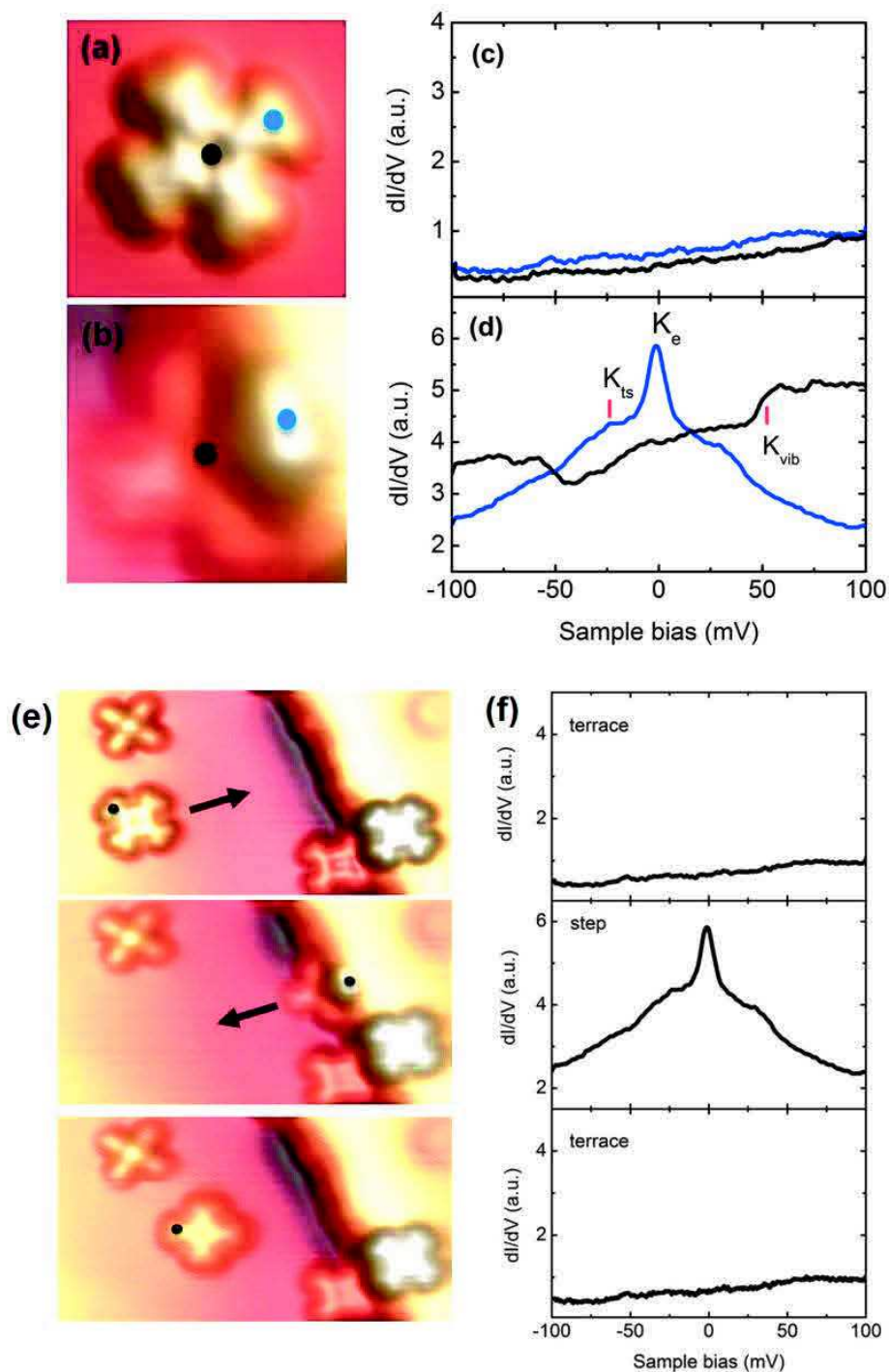
Figure 3.18 STM image of CuPc molecule adsorbed on (a) the flat terrace and (b) the monatomic step of Ag(111) surface. The corresponding dI/dV spectra acquired around E_F on the metal ion (black) and the benzene site of CuPc on (c) the flat terrace and (d) the monatomic step. The zero-bias Kondo resonance, triplet-singlet excitation and inelastic vibrations observed in CuPc are labeled as K_e, K_{ts} and K_{vib}, respectively. (e) The lateral manipulation of a CuPc molecule towards and away from the monatomic step by STM tip. (f) The corresponding dI/dV spectra measured at indicated points during the manipulation process in (e).

 In contrast with the molecule on the flat terrace, the dI/dV spectra for CuPc adsorbed on the monatomic step shows several characteristic signatures of low energy excitations around the Fermi level. The dI/dV spectrum measured over the anchoring lobe reveals a prominent peak located at zero-bias, that can be attributed to an elastic Kondo resonance K_e as identified in previous studies [27]. Such a Kondo resonance peak is absent for other three lobes resting on the lower terrace. Additionally, the Kondo resonance can be switched off/on by moving CuPc molecule away from/towards to a monatomic step by the STM tip as shown in Figure 3.18(e) and 3.18(f). This indicates that the spin moment inducing the Kondo resonance is localized over the molecular lob which is anchored on the upper terrace. The corresponding Kondo temperature of $T_K = 50 \pm 5\,K$ can be estimated from the Kondo resonance width obtained by the curve fitting as shown in Figure 3.19.

 Apart from the elastic Kondo resonance peak observed at zero-bias, the STS spectra of CuPc shows side-peaks and conductance steps at finite energies near the Fermi level (see Figure 3.18(d)). It is well known that inelastic excitations induce step-like increases in the differential conductance spectra symmetrically distributed in energy around E$_F$, very much like the spectra observed on Cu ion in Figure 3.18(d). In the Kondo system, the coupling of the Kondo state to such excitations leads to additional peaks like K_{ts} (triplet-singlet excitation) and K_{vib} (inelastic vibration) that are symmetrically distributed with respect to the Fermi level.
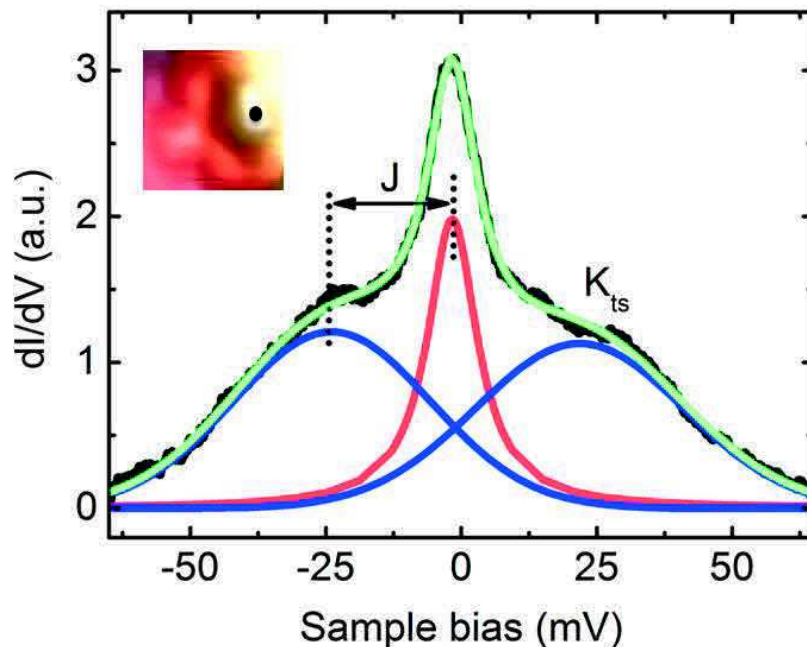

Figure 3.19 dI/dV spectrum of CuPc molecule adsorbed on a Ag(111) monatomic step. The spectrum is fitted by the superposition (green) of a Fano (red) and two Gaussian (blue) functions representing the Kondo resonance and intra-molecule magnetic excitations. The triplet-singlet excitation and intra-molecule exchange coupling in CuPc are labeled as J and K_{ts}, respectively.

Based on the previously reported result [5, 27], we can assign the inelastic step features at about ± 50 and ± 75 meV found over the Cu ion center (see Figure 3.18(d)) to the vibrational excitations that involve distortion of the Cu-N_p bonds. In contrast to the Cu ion, the inelastic excitation at the benzene ring appears as two additional side peaks of the zero-bias Kondo resonance and it must come from the magnetic configuration of the molecule. In this CuPc molecule, the central Cu ion has a magnetic moment which coexists with the ligand spin. Therefore, we assign the side peaks to the intra-molecular magnetic excitations due to the exchange coupling of the ligand π-spin to the Cu d spin to form a singlet (S=0) and a triplet (S=1) state. The energy positions of the two side peaks determine the intra-molecular exchange coupling (J) between the d and π spins. The curve fitting (see Figure 3.19) estimates an intra-molecular exchange coupling of $J = 21 \pm 1\ meV$ in good agreement with previous result [27]. A similar result has been reported for CuPc adsorbed on Ag(100) surface [5]. The strong Kondo peak at zero-bias indicates the triplet S=1 state is the ground state of the CuPc molecule; otherwise no Kondo screening would be possible. Thus, we conclude that the metal and the ligand spins are aligned parallel to each other in the ground state, whereas the excited state is a singlet (S=0) state.

References

[1] O. Bekaroglu, Y. Bian, G. Bottari, X. Cai, U. Hahn, N. Ishikawa, J. Jiang, N. Kobayashi et al, Functional Phthalocyanines Molecular Materials (Springer, Berlin, 2010)

[2] L. Bognani and W. Wernesdorfer, Nature Mater. 7, 179 (2008)

[3] K. Moth-Poulsen and T. Bjornholm, Nat. Naotechnol. 4, 551 (2009)

[4] K.Jens, K. Michael, S. Jacob, H. Pin-Jui et al Nano. Lett. 14, 3895 (2014)

[5] A. Mugarza, R. Robles, C. Krull, N. Lorente, et al Phys. Rev. B 85, 155437 (2012)

[6] D. Jacob, M. Soriano, J. Palacios, Phys. Rev. B 88, 134417 (2013)

[7] Liwei Liu, Kai Yang, Yuhang Jiang, et al, Scientific Reports 3, 01210 (2013)

[8] F. Ruckerl, B. Mahns, E. Dodbiba, et al J. Chem. Phys. 145, 114702 (2016)

[9] Liwei Liu, Kai Yang, Yuhang Jiang, et al Physic. Rev. Lett. 114, 126601 (2015)

[10] Y. S. Fu, S. H. Ji, X. Chen, X. C. Ma, et al. Phys. Rev. Lett. 99, 256601 (2007)

[11] K. Nagaoka, T. Jamneala, et al Phys. Rev. Lett. 88, 077205 (2002)

[12] K.Jens, K. Michael, S. Jacob, H. Pin-Jui, et al Phys. Rev. B 91, 235130 (2015)

[13] S. Kezilebieke, A. Amokrane, M. Abel, et al J. Phys. Chem. Lett. 5, 3175 (2014)

[14] V. Madhavan, W. Chen, T. Jamneala, M. F. Crommie et al Science 280, 567 (1998)

[15] V. Madhavan, W. Chen, T. Jamneala, et al Phys. Rev. B 64, 165412 (2001)

[16] W. Chen, T. Jamneala, V. Madhavan, et al Phys. Rev. B 60, R8529(R) (1999)

[17] A. J. Heinrich, J. A. Gupta, C. P. Lutz, and D. M. Eigler, Science 306, 466 (2004)

[18] M. Ternes, A. J. Heinrich, et al J. Phys.: Condens. Matter 21, 053001 (2009)

[19] Jörg Meyer, Robin Ohmann, Anja Nickel et al. Phys. Rev. B 93, 155118 (2016)

[20] W. A. Hofer, G. Teobaldi, and N. Lorente, Nanotechnology 19, 305701 (2008)

[21] A. Zhao, Q. Li, L. Chen, H. Xiang, W. Wang, S. Pan, et al., Science 309, 1542 (2005)

[22] U. G. E. Perera, H. J. Kulik, V. Iancu, et al, Phys. Rev. Lett. 105, 106601 (2010)

[23] F. Petraki, H. Peisert, F. Latteyer, U. Aygül, et al J. Phys. Chem. C, 115, 21334 (2011)

[24] E. Minamitani, Y. S. Fu, Q. K. Xue, Y. Kim, et al Phys. Rev. B 92, 075144 (2015)

[25] H. Hewson, The Kondo Problem to Heavy Fermions (Cambridge University Press, Cambridge, 1997)

[26] Cornelius Krull, PhD thesis 2012, Universitat Autonoma de Barcelona

[27] A. Mugarza, C. Krull, R. Robles, S. Stepanow, et al *Nat. Commun.* 2, 490 (2011)

Chapter 4

Manganese phthalocyanines bilayer on Ag(111)

For many technological applications, it is necessary to place the molecules on a supporting metallic surface or electrode. However, many interesting intrinsic physical properties, exhibited by the molecules in the bulk state, in a solution or in the gas phase, may be modified by the molecule-substrate interaction. A number of approaches for tuning the molecule-substrate interaction have been reported [1-6]. For example, a thin spacer layer between the metal substrate and the molecule has been used to decouple the molecules from the substrate electronic systems [1-2, 7]. Indeed the electronic decoupling of the molecules from the metal substrate naturally occurs in a bilayer or multilayer thin film of molecules [8-10]. In the multilayer system, the first layer works as a buffer layer to isolate the upper layers electronically from the substrate and then the electronic state of the upper layer molecules might be similar to those in the bulk or gas-phase. From this point of view, the bilayer structure of phthalocyanine molecules on the metal surface is an ideal model system to study the influence of electronic decoupling on the physical properties of the molecules.

In this chapter, we will present the low-temperature scanning tunneling microscopy and spectroscopy (STM/STS) studies on the bilayer MnPc molecules on Ag(111) surface to investigate the influence of electronic decoupling on the adsorption, electronic and magnetic properties of the MnPc molecules in the second layer. Our systematic STM studies on the MnPc molecules in the second layer starting from a single molecule up to the ordered bilayer structures will provides a more comprehensive understanding of the electronic and magnetic properties of the MnPc molecules for the first time.

4.1 Growth of the bilayer MnPc molecules

In this section we will investigate the growth behavior of the bilayer MnPc/Ag(111) system starting from the isolated individual MnPc molecules on the top of the first monolayer structure to the self-assembled second layer molecular islands.

4.1.1 Adsorption of isolated MnPc molecule in the second layer

In order to study the adsorption configuration of the isolated MnPc molecule in the second layer, firstly the MnPc molecules are deposited on Ag(111) substrate at room temperature to form a self-assembled ordered monolayer structure with square lattice pattern. All the

MnPc molecules in the monolayer have the same azimuthal orientation and the molecular axes are aligned along the $[10\bar{1}]$ and $[1\bar{2}1]$ high symmetry directions of the Ag(111) surface (see Figure 4.1(a), (c) and (e)). This ordered monolayer structure covers completely the surface of the sample and acts as a wetting layer for the second layer molecules to isolate them electronically from the Ag(111) substrate. Subsequently, a small number of MnPc molecules were deposited on top of the ordered monolayer while keeping the sample at room temperature. The limited thermal diffusion length of MnPc molecules over the first monolayer prevents the cluster formation and leave these MnPc molecules in its isolated molecular format even at room temperature. Then, the isolated individual second layer MnPc molecules can be investigated by STM.

This method allowed us to investigate the adsorption configurations of isolated individual MnPc molecules in the second layer by the high-resolution scanning tunneling microscopy (STM) measurements at the temperature of 4.5 K. In the STM topographic image the first layer MnPc molecules exhibit a symmetric four-lobe structure with a bright central protrusion. The isolated MnPc molecules in the second layer (Figure 4.1(a) and (c)) look similar to the ones observed in the first monolayer but exhibit enhanced structural contrasts due to the electronic decoupling from the Ag(111) substrate. More interestingly, we found three distinct adsorption configurations for the isolated single MnPc molecules in the second layer: (i) On-top configuration (~20 %), (ii) Shifted configuration (~30 %), and (iii) Bridge configuration (~50 %). This classification of the adsorption configurations is based on the relative position of the second layer single MnPc molecule with respect to the first layer MnPc molecule as shown on the high-resolution STM images of Figure 4.1(a), (c), (e) by means of the superimposed molecular structure. The percentages for finding an adsorption configuration suggest that the MnPc molecule with the bridge configuration is energetically the most stable one. However, it is worth mentioning that alternatively, the three different adsorption configurations can be obtained by manipulation with the STM tip at the experimental temperature of 4.5 K by dragging the molecules out of a second layer island and moving them to a preferential adsorption site of the first monolayer.

In the on-top adsorption configuration, a single MnPc molecule appears as symmetric four-lobe pattern with a bright central protrusion, implying that the second layer single MnPc molecule adsorbs flatly on the first monolayer and thus lies parallel with respect to the Ag(111) substrate. A close examination of the high resolution STM image of Figure 4.1(a) confirms that although the single MnPc molecule in the second layer is vertically aligned with the Mn ion of the first layer MnPc, the second layer MnPc molecule is rotated by 45° around the axis normal to the surface (see Figure 4.1(a) and (b)). The on-top adsorption configuration observed for a single MnPc molecule in the second layer is similar to the on-top configuration that has been observed by Chen et al [11] on the first and second CoPc monolayer adsorbed on Pb(111).

In the shifted configuration, a single MnPc molecule in the second layer also appears as a clearly visible four-lobe pattern with a bright central protrusion, implying again that the

second layer MnPc molecule adsorbs flatly on the first monolayer. In this configuration, a single MnPc molecule in the second layer adsorbed with a configuration where its in-plane molecular axes are aligned parallel to first layer (see Figure 4(c) and (d)). It should be note that the flat adsorption configuration of a single MnPc molecule in the second layer seems to be quite common, since the same conclusion was reported in the recent experimental study of MnPc on [12-13]. In these works the STM measurements show that the molecular plane of a single MnPc in the second layer is parallel to the substrates.
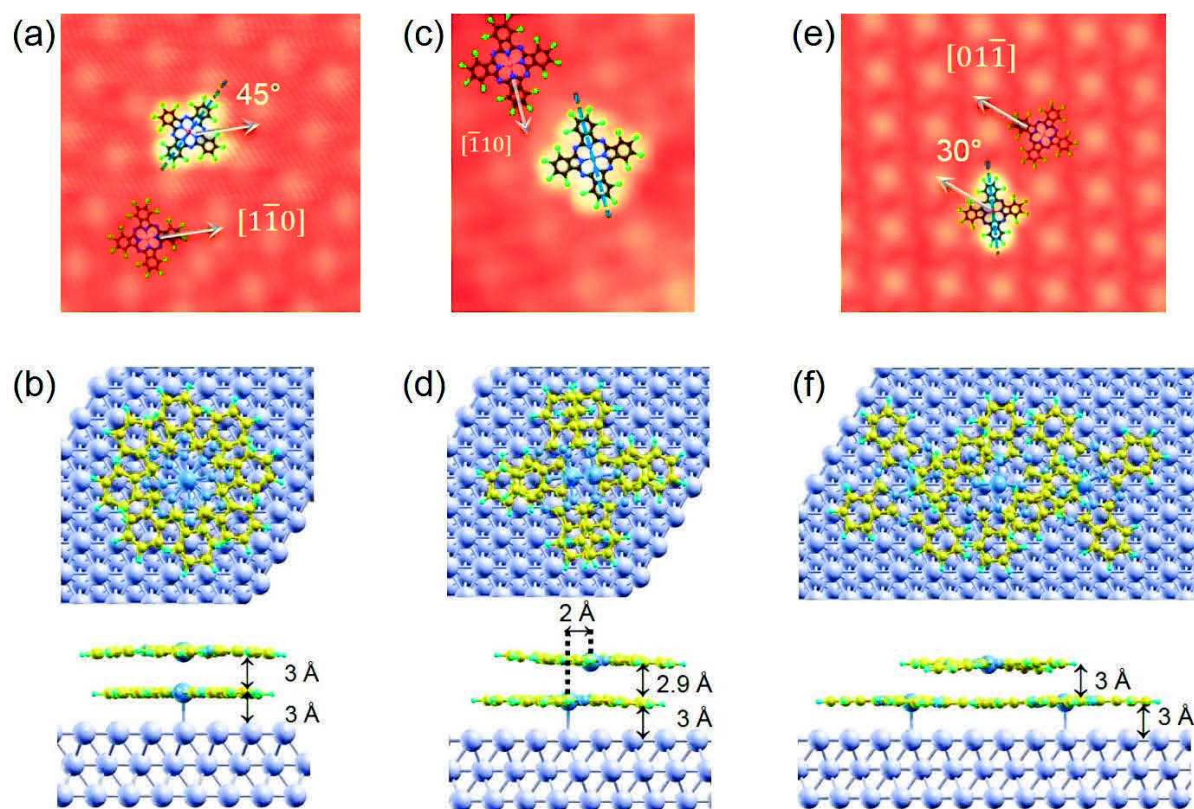

Figure 4.1 STM images and schematic representations (top and side views) of the single MnPc molecule adsorbed with (a, b) the on-top configuration, (c, d) the shifted configuration, and (e, f) the bridge configuration, respectively, on the top of MnPc monolayer on Ag(111).

In the bridge configuration, a single MnPc molecule in the second layer adsorbs between the two neighboring MnPc molecules from the first monolayer thus forming a bridge. In this configuration, a pair of opposite lobes of the phthalocyanine bind with the Mn ions of two neighboring MnPc molecule in the first layer while the two other Pc lobes are free. The Mn ion is lying above the gap between two neighboring first layer MnPc molecules (see Figure 4.1(e) and (f)). In the STM image, the MnPc molecule with bridge configuration appears as two bright-lobes and two dim-lobes with a small depression at the molecule center. Additionally, the in-plane molecular axes are rotated by 30° around the normal axis, compared with the MnPc molecule in the first monolayer. The small depression at the center of the molecule with the bridge configuration is quite in contrast to the central

bright protrusion for the molecules with the on-top and parallel adsorption. This topographic difference at the molecule center implies that the central Mn ion of MnPc with bridge configuration is highly decoupled from the underlying substrate. In addition, the electronic decoupling in the bridge configuration might be much stronger than the one of the on-top and shifted configurations.

4.1.2 Self-assembled islands of MnPc molecules in the second layer

In the previous section, we showed how the isolated single MnPc molecule adsorbs on top of MnPc monolayer. Here we will investigate further the growth behavior of the bilayer MnPc molecules on Ag(111) substrate.

The ultra-thin film of bilayer MnPc molecules can be obtained by sequential deposition of molecules on Ag(111) substrate. Firstly the ordered monolayer of MnPc molecules on Ag(111) was formed by the molecule deposition at the coverages larger than one monolayer, i.e. $\theta \geq 1\,\mathrm{ML}$. This molecular monolayer acts as a wetting layer and completely covers the surface of the Ag(111) substrate. It should be note that there is a repulsive interaction between MnPc molecules on Ag(111), and the self-assembled ordered monolayer structure of MnPc molecules would form only at the molecule coverage $\theta \geq 1\,\mathrm{ML}$.

Upon further increasing the molecule coverage, i.e. $1\,\mathrm{ML} \leq \theta < 2\,\mathrm{ML}$, the formation of the self-assembled second or third layer islands of MnPc molecules on the top of the wetting layer in a Stranski-Krastanov growth mode is observed as shown in Figure 4.2(a). This different growth behavior of the second layer MnPc molecules compared with that of the first layer indicates a remarkably weaker effect of the Ag(111) substrate on the growth of the second molecular layer. Moreover, the formation of the self-assembled second layer molecular islands over the wetting layer suggests an increased molecule-molecule interaction in the second layer at the expense of the reduced molecule-substrate interactions.

In order to determine the relative position of the second layer molecules with respect to the ones in the first layer, a topographic line profile of the MnPc bilayer (see Figure 4.2 (b)) was measured along the dotted arrow in Figure 4.2(a). The blue and red grid lines in the Figure 4.2(b) are representing the molecular lattice in the first- and second-layers, respectively. From the topographic line profile the inter-molecule distance (d) in the first- and second-layers are measured to be same and equal to $d = 13.2 \pm 0.2\,\text{Å}$. Interestingly, MnPc molecules in the second layer shows a small offset of $\Delta = 1.5 \pm 0.2\,\text{Å}$ with respect to the molecules underneath in the first layer as suggested by the line profile analysis in Figure 4.2(b).
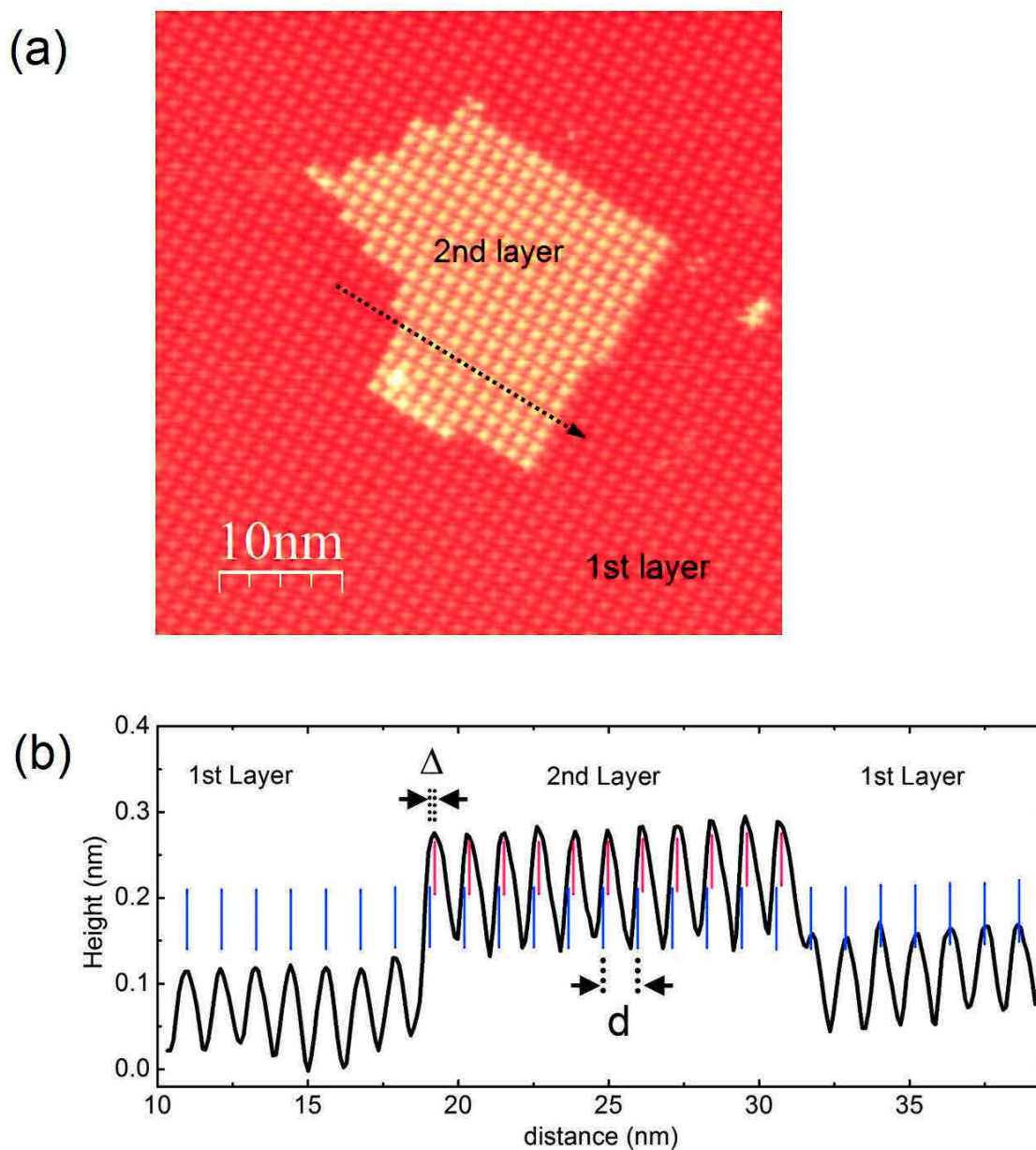
Figure 4.2 (a) STM image of the bilayer MnPc molecule on Ag(111) surface. (b) The topographic line profile measured along the dotted arrow in (a). The blue and red grid lines are representing the first- and second-molecular lattice, respectively.

The situation is completely different after annealing the bilayer MnPc/Ag(111) at temperature about 100 °C where a rearrangement of the 2nd layer molecules occurs. As shown in the high resolution STM images of a bilayer MnPc on Ag(111) in Figure 4.3(a) and (b), the MnPc molecules in the second layer exhibit more structural details than those of the first layer. While the center of each molecule appears as a bright protrusion in the STM images of Figure 4.3(a) and (b), the MnPc molecules in the second layer exhibit an asymmetric feature referring to a non-planar adsorption. It turns out that the MnPc

molecules within the second layer are slightly tilted out of the surface plane indicating a strong lateral inter-molecular interaction.
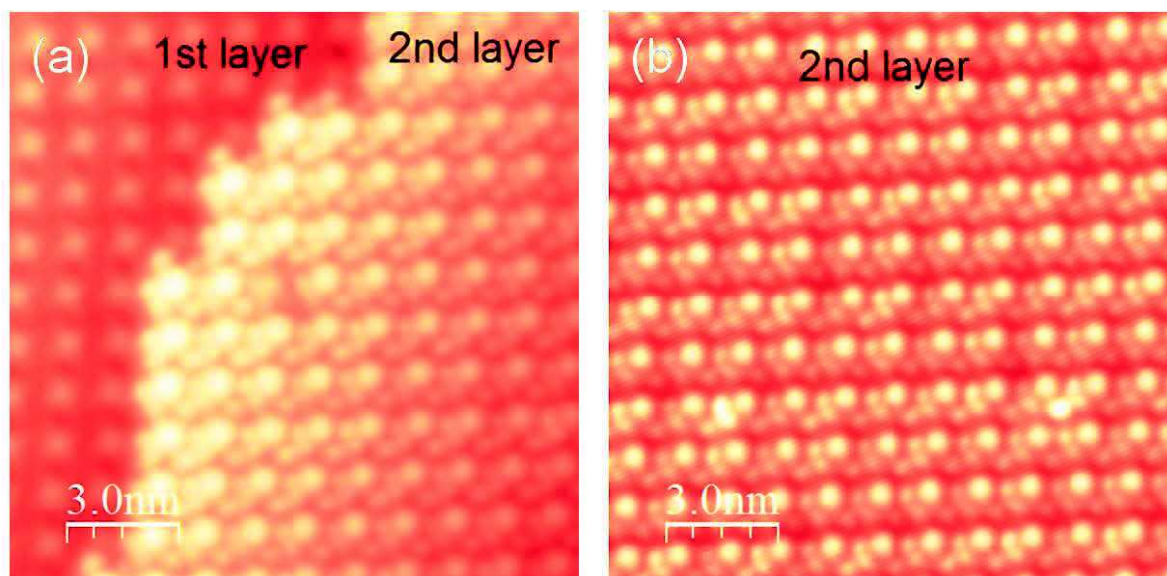

Figure 4.3 The high resolution STM image of (a) the mono- and bi-layer MnPc molecules on Ag(111) and (b) the second layer MnPc molecules.

 A carefully analysis also reveals that the distance between the centers of two adjacent MnPc molecules in the second layer is smaller than the inter-molecule distance in the first monolayer. The fact that the second layer is incommensurate with the first layer together with the tilted adsorption geometry are obviously a result of the molecule-molecule interaction, which becomes stronger in the second layer due to the weaker influence of the substrate-molecule interaction. This point is further analyzed in Section 4.3.2. A similar behavior has been observed in other TMPc bilayers such as FePc/Ag(111) [14], FePc/Cu(111) [15] and CoPc/Au(111) [16].

 In order to identify further the adsorption configuration of MnPc molecules in the second layer island, we performed a manipulation on the second layer MnPc molecules with the STM tip. Thus the adsorption configuration of MnPc molecules within the second layer island can be identified by comparing them with the situation of an isolated MnPc molecule dragged out of the second layer island and moved to a preferential adsorption site over the ordered first monolayer (see Figure 4.4(a) and (b)).

 It is remarkable that the manipulated single MnPc molecule in the second layer, the molecules in the first monolayer and those within the second layer islands all have the same molecule orientation with respect to the underlying Ag (111) substrate (see Figure 4.4(b)). However, the topographic line profile in Figure 4.4(c) shows that the second layer MnPc molecule center is laterally shifted by a distance of 1.75 ± 0.05 Å with respect to that of the underlying molecule in the first layer, and it is indicated by the offset of profile peak positions corresponding to the central Mn ion sites (see the red lines in Figure 4.4(c)). The lateral shift of the second layer molecule is shown schematically in Figure 4.4(d).
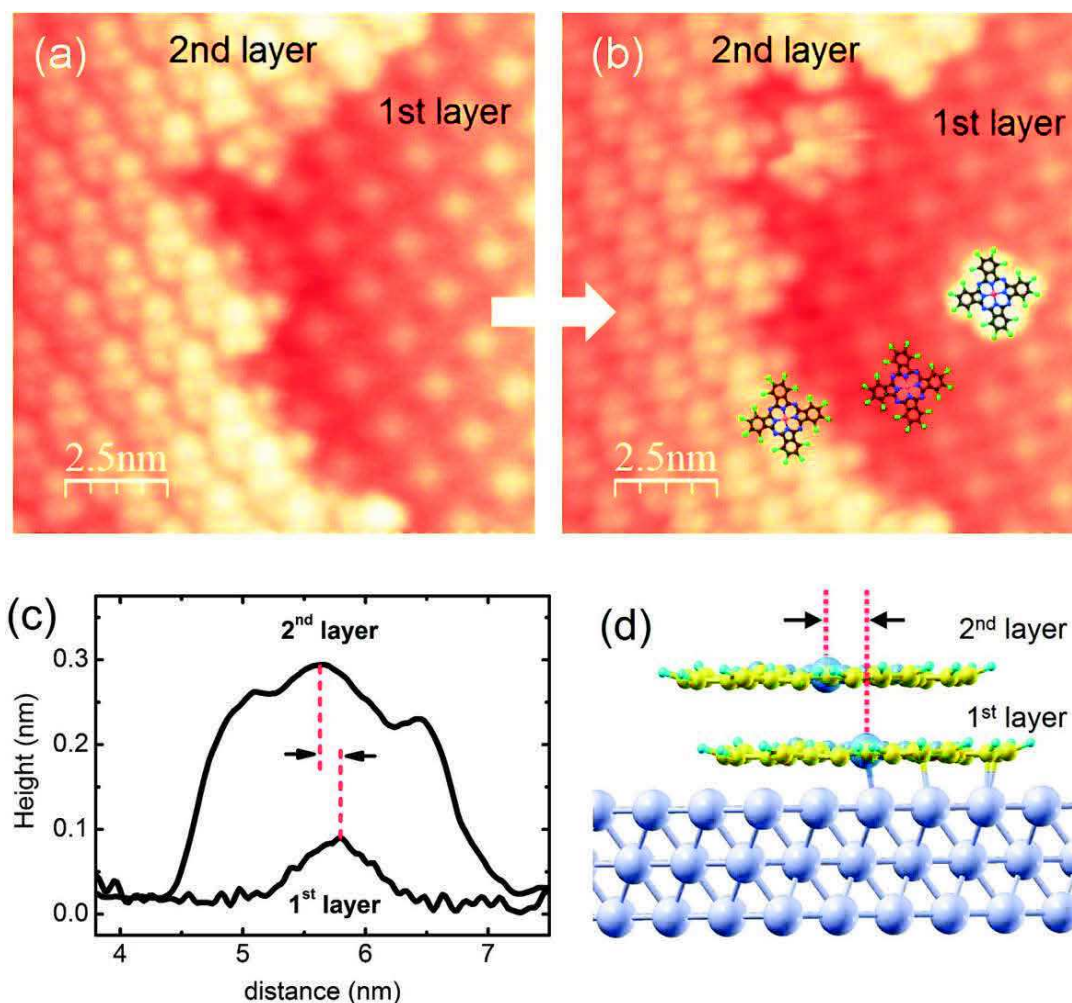
Figure 4.4 (a) and (b) STM manipulation where a single MnPc molecule is dragged out of the second layer island and placed a preferential adsorption site with parallel configuration. The molecular structure is superimposed to clarify the molecule orientations. (c) The topographic line profile of a manipulated second layer single molecule in (b) and the first layer molecule located right beneath of it in (a). (d) Schematic representation of the parallel and shifted adsorption configuration of the manipulated MnPc molecule in (b).

The lateral shifted distance observed in STM experiment is in good agreement with the DFT calculation [17] and x-ray diffraction (XRD) measurement [18] results which are found the Mn-N_{iso} bond length to be 1.95 ± 0.02 Å for MnPc molecule. This indicates that the Mn ion of MnPc in the second layer is located right above a N_{iso} (the N directly bound to Mn) atom of MnPc molecule in the first layer. Such a parallel and shifted adsorption configuration is also a favorable one for the MnPc molecules inside the self-assembled molecular island in the second layer. The observed lateral shift of the second layer MnPc molecules with respect to the ones in the first layer is similar to the shifted adsorption geometry between the second and the third monolayer of CoPc adsorbed on Pb(111) as observed by Chen et al [11].

4.2 Tunneling spectroscopy of the bilayer MnPc molecules

In the Section 3.3, we have discussed that the single MnPc molecules adsorbed directly on Ag(111) strongly interact with the substrate. Such a strong hybridization of the molecule with the substrate leads to a considerable broadening and shifting of the molecular orbital spectral features around the Fermi level. Upon formation of a densely packed ordered monolayer, where the inter-molecular interactions through the ligand orbitals become important, the electronic structure of MnPc molecules is somewhat modified, but still mainly determined by the direct coupling of molecules to the substrate through strongly hybridized d states of the central Mn ion. In this section we will investigate the evolution of the electronic structure of MnPc molecules from the first molecular layer to the second layer in which the molecules are naturally decoupled from the substrate.

In order to investigate the electronic properties, we performed wide-range tunneling spectroscopic measurements on the MnPc bilayer on Ag(111). The dramatic evolution of the electronic structures from the MnPc monolayer to the molecular bilayer can be seen in Figure 4.5 (a) and (b). The dI/dV spectra were recorded by positioning the STM tip above the center (black curves) and above the ligand (blue curves) of individual MnPc molecule in the first and second monolayer. The dI/dV spectrum of the first layer MnPc center is dominated by a sharp peak at the Fermi level as shown in the lower panel of Figure 4.5(a), which originates from the Kondo screening channel of the Mn 3d orbitals by the itinerant conduction electrons from the Ag(111) substrate. In addition the rather weak and broad structures at about + 0.35 eV and + 0.9 eV are observed for the monolayer MnPc molecule center, and they must also have the Mn 3d orbital character because the spectrum is obtained at the central Mn ion site.

In contrast to the spectrum taken at the center of the molecule, the first layer ligand spectrum shows well-resolved molecular orbital features at the energies about -0.28 eV and +0.6 eV. The peak at -0.28 eV is similar to the one observed for the isolated MnPc molecule (see Section 3.2). We attribute this low energy peak at -0.28 eV to the singly occupied molecular orbital (SOMO) that can be considered as a hybrid state of Mn 3d and ligand π orbitals. Similar conclusions were reported for the MnPc thin film characterized by the photoelectron spectroscopy [19].

Compared to the negative bias spectral feature of the molecular ligand, a pronounced peak centered at +0.6 eV together with the small shoulder at + 0.4 eV is observed in the positive sample bias (see blue curve in Figure 4.5(a)) corresponding to the unoccupied states of the molecular Pc ligand. Such a peak was absent in the isolated MnPc molecule on surface (see Section 3.2). This remarkable change upon the formation of the ordered monolayer implies the presence of a strong molecule-molecular interaction in the ordered monolayer structure of MnPc molecules. This inter-molecule interaction is most probably driven by the Pc ligand π-π interactions.
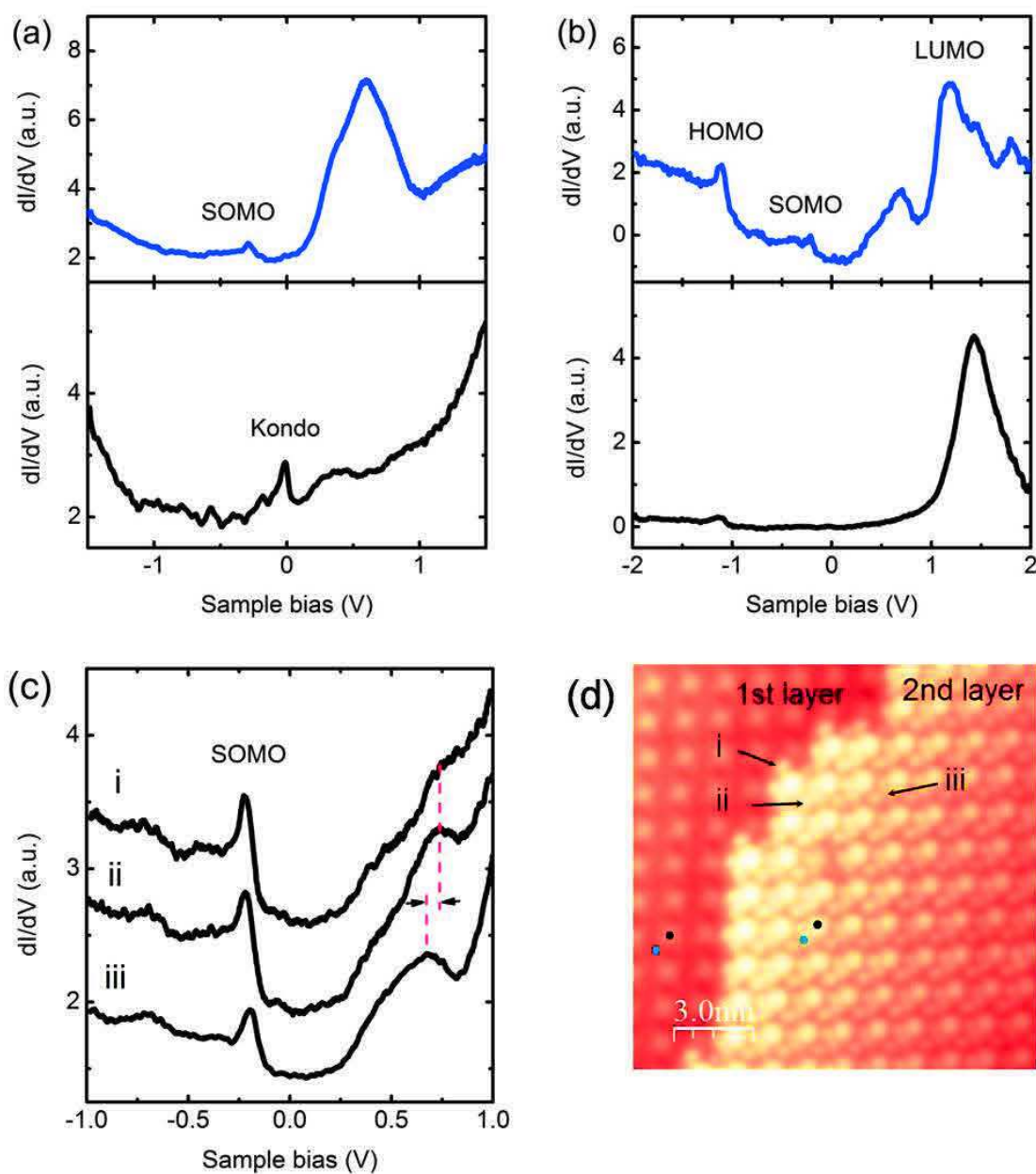
Figure 4.5 (a) and (b) dI/dV spectra acquired on the center (black, lower) and ligand (blue, upper) of the first and second layer MnPc molecules, respectively. (c) dI/dV spectra measured over the MnPc molecule lobes indicated by the three arrows in (d). (d) the MnPc bilayer structure on Ag(111) surface.

As shown in the Figure 4.5(b), the STS spectra taken over the MnPc molecules in the second layer drastically change compared with the monolayer spectra. The second layer MnPc ligand spectrum (see blue curve Figure 4.5(b)) exhibit the characteristic strong peak features at -1.13 eV and +1.2 eV, which are the spectroscopic signatures of the highest occupied molecular orbital (HOMO) and the lowest unoccupied molecular orbital (LUMO) of the MnPc molecules. In addition, the peak at +1.2 eV is overlapped by two other peaks at energies of +1.4 eV and +1.8 eV, respectively. These peak positions give rise to a

HOMO-LUMO energy gap of 2.3 to 2.9 eV which is in reasonably good agreement with the energy gap of 2.9 eV reported for the thick film of MnPc molecules by the optical adsorption spectroscopy [20]. The appearance of the clear electronic structures and evolution of the energy gap around the Fermi level in STS spectra of Figure 4.5(b) evidence the efficient decoupling of the second-layer MnPc molecules from the metallic Ag(111) substrate compared to the first layer MnPc, which interacts strongly with the substrate. Moreover, two relatively weaker features observed inside the HOMO-LUMO gap at -0.22 eV and +0.68 eV around the Fermi level are similar to those observed for MnPc molecules in the first monolayer (see the blue curves in Figure 4.5(a) and (b)). Compared to the first layer counterpart, these two peaks are shifted to the higher energies by almost the same amount (~ 0.1 eV) due to the electronic decupling from the substrate.

From the MnPc ligand spectra (see the blue curves in Figure 4.5(a) and 4.5(b)), it is clear that the first peak at negative bias labeled as SOMO is one of the characteristic features of MnPc molecule and is independent of the environment, i.e. the nearest neighboring molecules and the underlying metal substrate. The intrinsic character of this low energy peak is further supported by its presence in the second layer decoupled molecule. A similar SOMO feature was attributed to a molecular orbital originating from the hybridization of the Mn 3d orbitals with the ligand π orbitals within a MnPc molecule [19, 21]. On the other hand, the broad peak centered at + 0.68 eV originates from the ligand π-π interaction between nearest neighboring MnPc molecules in the second layer similar to the first monolayer situation. As an intermediate conclusion one may state that the weak coupling of the second layer MnPc molecule to the substrate preserves the intrinsic electronic structure of the molecules, in contrast to the MnPc monolayer where the MnPc molecules are directly coupled to the Ag(111) substrate.

The spectrum of the second layer MnPc center revealed a sharp weaker peak at -1.13 eV and a pronounced broad peak at 1.45 eV as shown by the black curve in Figure 4.5(b). These features observed for the electronically decoupled MnPc molecules must have the occupied and unoccupied Mn 3d orbital state characters because the spectrum is obtained at the Mn ion site in the second layer. In addition to these strong Mn 3d orbital features, the dI/dV spectrum in Figure 4.5(b) also has the weaker and broader features, similarly observed for the MnPc molecule in the first monolayer.

To get a deeper insight into the influence of molecule-molecule interaction in the second layer on its spectra, the spectra over the ligand of MnPc molecules in the second layer island was measured as a function of the number of nearest-neighbor molecules as shown in Figure 4.5(c). While the MnPc molecule at the island corner display a very weak feature at 0.73 eV (see spectrum (i) in Figure 4.5(c)) over its non-overlapping lobe indicated by the arrow (i) in Figure 4.5(d), a broad peak is developed at the same energy for the overlapping lobe of this molecule (see spectrum (ii) in Figure 4.5(c)). For the strongly overlapped lobe (marked by arrow (iii)) of MnPc inside island, the unoccupied state peak becomes more evident and shifted to 0.68 eV towards to the Fermi level as shown in Figure 4.5(c). The gradual evolution of pronounced peak at 0.68 eV for the molecule inside the island indicates the existence of a strong inter-molecular interaction within the second

layer. In contrast, the SOMO state depends weakly on the number nearest neighbor molecules and exhibits only a small shift from 0.22 eV for the lobe (i) to 0.20 eV for the lobe (iii).

 It must be emphasized that the isolated bridge like MnPc molecule in the second layer (see Figure 4.6(b)) already shows a signature of the electronic decoupling with very sharp HOMO and LUMO peaks at -1.32 eV and 1.16 eV, respectively. Indeed the multiple peak structures at the positive bias discussed before is already present in a single molecule as shown in Figure 4.6(a). The gap between HOMU-LUMO states is about 2.5 eV and agrees reasonably well with the one for the second layer island. Furthermore, we notice that no other STS spectral features are observed inside the gap except from the zero-bias Kondo peak.
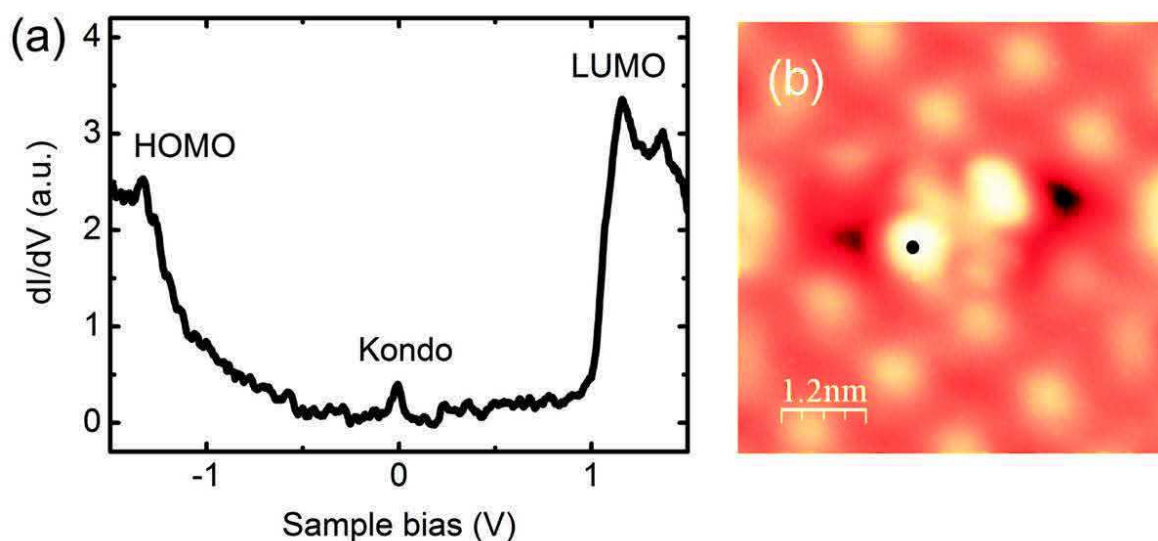

Figure 4.6 (a) dI/dV spectra acquired on the bright lobs of MnPc molecule in the second layer with bridge-like adsorption configuration shown in (b).

4.3 Kondo effect of MnPc in the second layer island

In this section, we will investigate the Kondo behavior of the bilayer MnPc molecules on Ag(111) substrate. The influence of adsorption configurations and inter-molecule interactions (i.e. inter-layer as well as intra-layer interactions) on the Kondo effect of the second layer MnPc molecules will be explored and analyzed by the differential conductance (dI/dV) spectroscopy close to the Fermi level.

Firstly, we will present the Kondo effect of single MnPc molecules in the second layer as a prototypical spectrum for comparison with the STS result observed for the MnPc molecules in extended second layer islands. Then, we will further discuss the Kondo effect of second layer MnPc molecules inside the self-assembled molecular islands by considering the influence of nearest neighboring molecules and position with respect to the edge of molecular islands. These systematic spectroscopic investigations will provide a deeper and more comprehensive understanding of the Kondo behavior of weakly coupled MnPc molecules.

4.3.1 Isolated MnPc molecule in the second layer

We will start our discussion with the relatively simple Kondo behavior of the isolated MnPc molecules on the top of the ordered monolayer. As was discussed in Section 4.1.1, the isolated MnPc molecules in the second layer show three distinct adsorption configurations leading to three different interactions with the first monolayer. In the following, the Kondo behavior of each configuration will be analyzed in detail by STM measurements with the high spatial and energy resolutions.

A. MnPc molecule with bridge configuration

The dI/dV spectrum acquired over the central small depression, i.e. corresponding to the central Mn ion, of the MnPc with the bridge configuration shows a sharp peak at zero-bias as shown by the black curve in Figure 4.7(a). In addition, the two bright lobes which are binding to the Mn ions of two neighboring MnPc molecules in the first monolayer exhibit a prominent peak at zero-bias in STS spectrum (see the black curve in Figure 4.7(b)). This peak feature is somehow broader than the one observed at the molecule center. On the other hand, flat featureless dI/dV spectra (see Figure 4.7(c)) are observed over the two dimmer lobes in the orthogonal direction. Since the bridge position is energetically the most stable configuration for the isolated molecules, we observed the same spectroscopic features for all bridge MnPc molecules measured in the different experiments with different tips.

The peak measured at the bridge molecule center (see Figure 4.7(a)) is narrow and nearly symmetric with respect to the Fermi level. This is in contrast with the asymmetric broad peak observed over the Mn center of the single MnPc molecule (see Section 3.3)

and the molecular monolayer on Ag(111). The sharpening of zero-bias peak is a direct consequence of the electronic decoupling of the second-layer molecule from the underlying substrate, as evidenced by both STM image (see Figure 4.7(d)) and STS spectrum measured over the wider energy range (see Section 4.2).
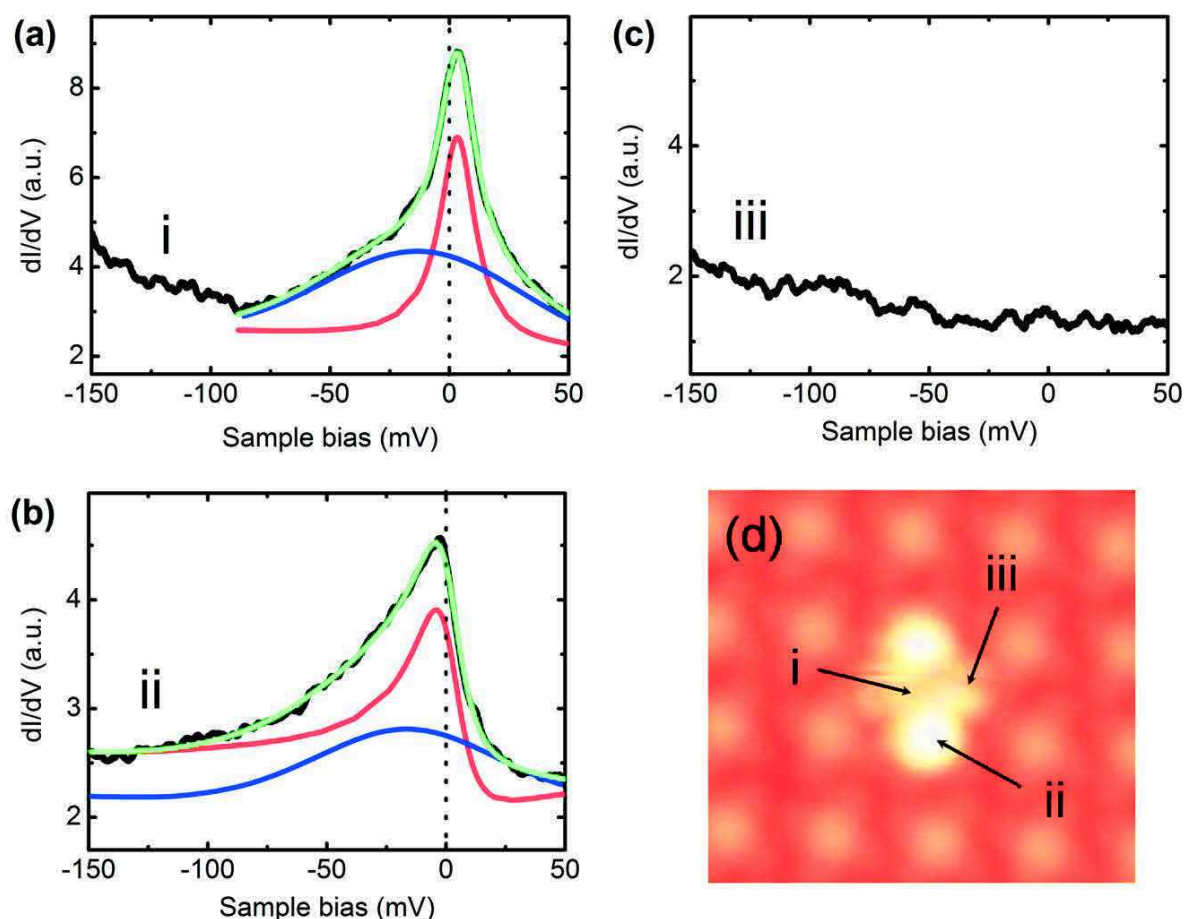

Figure 4.7 dI/dV spectra taken over (a) the central depression, (b) the bright lobs, and (c) the faint lobs of a bridge molecule. (d) STM image of a MnPc molecule adsorbed on top of the first monolayer with the bridge-like configuration. The molecule center, the bright lobs, and the faint lobs are indicated by the arrows i, ii and iii, respectively. Note that the data (black curves) in (a) and (b) are fitted by the superposition (green) of a Fano (red) and Gaussian (blue) functions which are representing the Kondo resonance and an orbital state, respectively.

Interestingly, the asymmetric prominent peak observed at the two bright lobes is very similar to the spectrum obtained over the Mn ion of MnPc molecule directly adsorbed on the Ag(111) substrate. Moreover, this peak completely disappeared on the two orthogonal dimmer lobes as shown in Figure 4.7(c). These experimental facts suggest that the zero-bias peaks on the bright lobes (see Figure 4.7(b)) originate from their interaction with the Mn ions of the molecules in the first layer.

The feature at zero-bias observed above the Mn ion of bridge molecule (Figure 4.7(a)) is fitted by the superposition of a Fano and Gaussian functions and yields a Kondo temperature of $T_K = 105 \pm 2$. The Kondo temperature for this second layer molecule is significantly lower than $T_K = 160 \pm 10\,K$ for the on-surface MnPc molecules.

However, the observed Kondo temperature ($T_K = 105 \pm 2\,K$) for the second layer molecule indicates the presence of a relatively strong Kondo interaction between the local spin moment of MnPc in the second layer and its surrounding. This experimental fact is contrary to the expectation that the Kondo resonance is weakened or suppressed in the second layer due to the weak coupling with the metal substrate. In other words, the coupling of Mn spin moment to the local molecule environment seems to play a crucial role in the second layer molecule rather than the coupling to the underlying substrate. Therefore, while the Kondo resonance observed for MnPc molecules adsorbed directly on Ag(111) is attributed to the exchange interaction between the MnPc molecular spin and the itinerant conduction electrons of the Ag(111) substrate (see Section 3.4), this interpretation is unlikely to be fully valid for the sharp Kondo peak (see Figure 4.7(a)) observed at the center of bridge molecule in the second layer.

The recent studies on TMPc molecules and their derivatives showed that the interaction between the π orbitals of the molecule ligand and the d orbitals of the central metal ion, i.e. the π-d interaction, plays an indispensable role in determining their electronic and magnetic properties [22-25]. A strong π-d interaction in the MnPc molecule was suggested in photoemission [26] and STM [21] experiments, and confirmed further by the density functional theory (DFT) calculations [27-28]. In addition, the numerical renormalization group (NRG) [21] and ab-initio calculations [29] showed that the strong π-d interaction induce an anti-ferromagnetic (AFM) coupling between the ligand π orbitals and the Mn d orbitals inside the MnPc molecule.

Thus, the AFM correlation between the spin localized at Mn d orbital and the delocalized π electron spins from its surrounding environments, which consists of the bridge molecule itself and the first MnPc monolayer, may produce a singlet ground state, similar to the Kondo state in MnPc on a surface (see Section 3.4). Then, this correlated many-body state could lead to an enhanced density of states at the Fermi level as shown in Figure 4.7(a) by the resonance peak at zero-bias. Moreover, recent theoretical findings also evidenced that the Kondo effect can occur in a single molecule [30] or in a quantum dot called "Kondo box" [31-32] where the electrons in a set of discrete states couple to the magnetic impurity. Although the self-contained Kondo effect in a bridge MnPc molecule is not fully confirmed at this stage, such a new screening mechanism in a decoupled second layer molecule is most likely to be fully valid for the origin of the sharp Kondo peak (see Figure 4.7(a)). Such a self-contained Kondo effect in a single molecule has never been observed in previous STM experiments.

In contrast to the spectrum obtained at the Mn center, the asymmetric prominent peak observed at the two bright lobes can be attributed to a Kondo resonance related to the first layer MnPc molecule. Since the bright lobes are binding to the Mn ions of MnPc

molecules from the first layer, the resonance peak in Figure 4.7(b) has a same origin as the Kondo resonance observed for MnPc molecules adsorbed directly on Ag(111). The line shape fitting of the zero-bias peak observed over the bright lobes of the bridge MnPc molecule yields a Kondo temperature of $T_K = 135 \pm 5\ K$, which is reasonably well agrees with $T_K = 160 \pm 10\ K$ for the on-surface molecule. The similar Kondo temperature is further confirming that both peaks have a similar origin.

B. MnPc molecule with shifted and on-top configurations

The dI/dV spectrum measured over the central Mn ion of the shifted MnPc molecule exhibit a pronounced peak at zero bias with nearly symmetric line shape with respect to the Fermi level (see the black curve in Figure 4.8(a)). Importantly, the same spectroscopic feature was reproduced in the different experiments with different tips. This peak feature in dI/dV spectrum (see Figure 4.8(a) is considerably broader than the one observed at the center of MnPc with bridge configuration (see Figure 4.7(a)). Interestingly, it is similar to the Kondo peak observed for the single MnPc molecule and the molecular monolayer on Ag(111).

For the same reason that mentioned above, we can safely attribute the broad peak near the Fermi level in Figure 4.8(a) to the Kondo resonance of the MnPc molecule with shifted configuration. This broad zero-bias peak was decomposed into a narrow Fano profile at the Fermi level and a broader Gaussian profile located just below the Fermi level, representing respectively the Kondo resonance and an occupied molecular orbital as shown in Figure 4.8(a). The spectral component described by a narrow Fano profile at the Fermi level has an energy width of $\Gamma = 12.3 \pm 0.2\ \mathrm{meV}$ and yields a Kondo temperature of $T_K \approx \Gamma/k_B = 140 \pm 5\ K$. This Kondo temperature for the shifted molecule is considerably higher than $T_K = 105 \pm 2K$ the one for the bridge MnPc molecule. This implies that the Kondo interaction between the local spin moment of second layer molecule and its surrounding environments strongly depends on the adsorption configuration of the molecule.

Interestingly, the Kondo temperature of the shifted MnPc molecule in the second layer is comparable with the one for the MnPc molecule directly adsorbed on the Ag(111) substrate. This is surprising since the Mn ions in the first and second layers are subjected to very different electronic environment, and hence may exhibit completely different Kondo behavior. However, our experimental results indicate that the Kondo screening of a single molecule in the second layer is almost as efficient as for the molecule adsorbed directly on the Ag(111) substrate. This is unusual and was not observed in previous experiments. As we discussed above for the bridge MnPc molecule, this experimental result again implies the presence of a strong coupling of Mn spin moment to the local molecule environments.
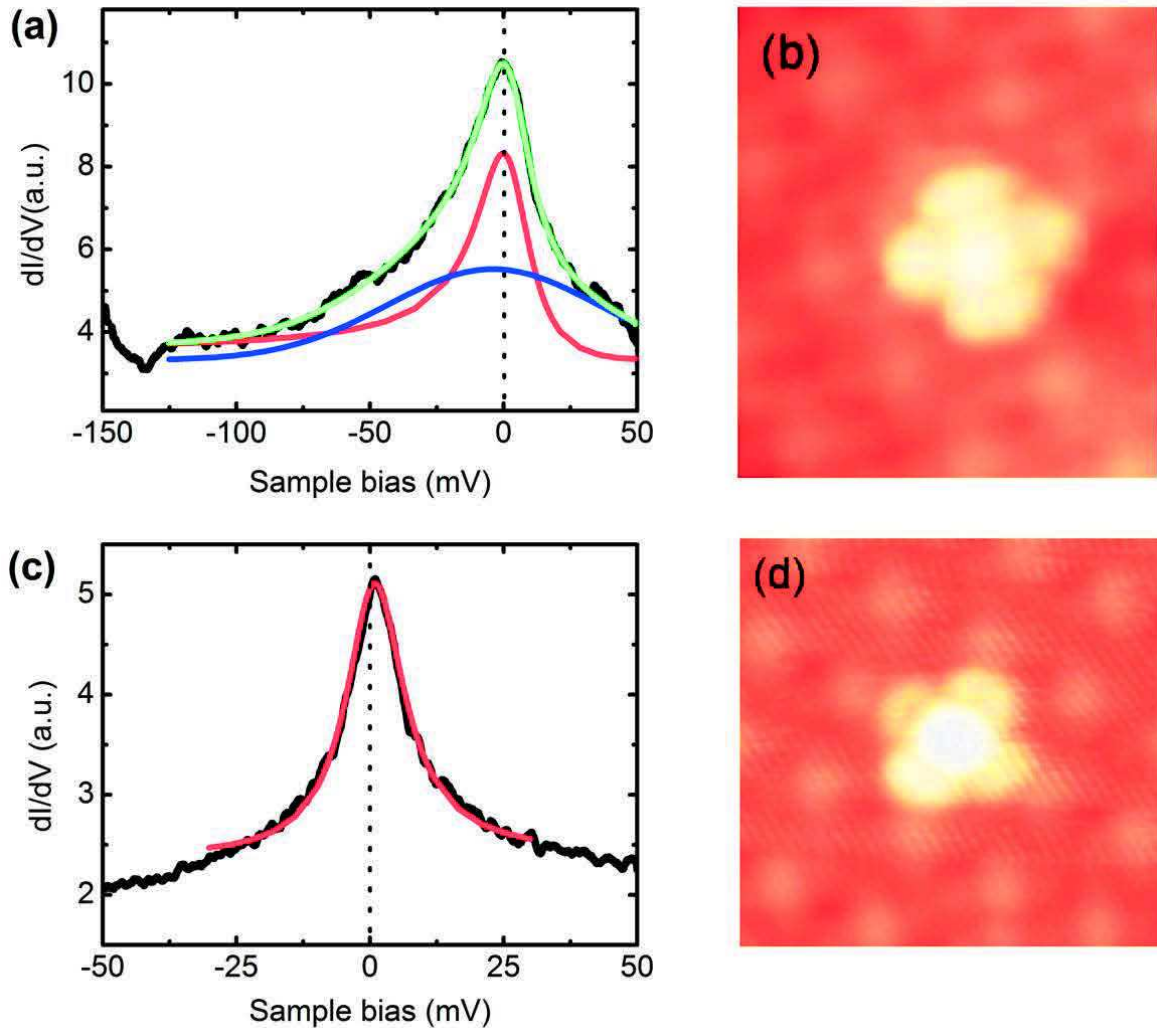
Figure 4.8 (a) dI/dV spectrum (black) taken over the central protrusion of the shifted MnPc in the second layer shown in (b). (c) dI/dV spectrum (black) taken over the central bright spot of the on-top MnPc in the second layer shown in (d). The spectrum in (c) is fitted by a single Fano function, while the one in (a) is fitted by the superposition (green) of a Fano (red) and Gaussian (blue) functions which are representing the Kondo resonance and an orbital state, respectively.

 In contrast to the spectrum obtained for the second layer shifted molecule, the dI/dV spectrum acquired over the bright center, i.e. Mn ion, of the on-top MnPc reveals a sharp peak feature at zero-bias (black curve in Figure 4.8(c)). For such a molecule, the same spectroscopic feature was reproduced in the different experiments with different tips. The peak in the dI/dV spectrum of Figure 4.8(c) is very narrow and symmetric with respect to the Fermi level. This symmetric peak is much sharper than the one observed for isolated molecule with shifted as well as and bridge configurations. In addition, this symmetric sharp peak is in contrast with the asymmetric broad peak observed for the single MnPc molecule and the molecular monolayer on Ag(111). The sharpening of zero-bias peak is a direct consequence of the electronic decoupling of the second-layer molecules.

 Due to the similar reason discussed for the shifted and bridge configurations, we can tentatively attribute the sharp peak feature at the Fermi level shown in Figure 4.8(c) to the Kondo resonance of the on-top MnPc molecule. In order to extract the characteristic Kondo temperature, the sharp peak feature at E_F is fitted by a single Fano function (red curve in Figure 4.8(c)). The curve fitting determines an energy width at half-maximum of $\Gamma = 6.5 \pm 0.2 \, \mathrm{meV}$ corresponding to a Kondo temperature of $T_K = \Gamma/k_B = 75 \pm 2 \, K$.

 The Kondo temperature for the on-top molecule is much lower than the ones for the second layer molecules with bridge and shifted configurations. On the other hand, for an isolated MnPc molecule in the second layer, Kondo temperature varies in a wide range between 75 K and 140 K from on-top configuration to shifted configuration. In addition, the Kondo temperature for the on-top MnPc molecule of second layer is greatly reduced compared with $T_K = 160 \pm 10 \, K$ the one for the on-surface molecule.

 In the previous STM studies [11], a much sharper zero-bias peak in dI/dV spectrum has been reported for the on-top CoPc molecule in the bilayer CoPc/Pb(111) system. This peak was attributed to the Kondo resonance based on the peak response to the variable magnetic field. The origin Kondo resonance was assumed to be a residual coupling between the Pb(111) substrate and the CoPc molecule in the second layer. The corresponding Kondo temperature was found to be only 10 K due to the large molecule-substrate distance of $d \geq 6 \, \text{Å}$.

 In the present experiment, however, the Kondo temperature measured for the on-top MnPc molecule in the bilayer MnPc/Ag(111) is much higher than the one observed for the second layer on-top CoPc molecule in the bilayer CoPc/Pb(111). In addition, the Kondo resonance with $T_K = 75 \pm 2 \, K$ for the on-top MnPc molecule cannot be explained by the residual coupling model proposed in the previous experiment for the bilayer CoPc/Pb(111).

C. Analysis of Kondo behavior

 As we discussed above, the isolated MnPc molecules in the second layer exhibits very interesting Kondo behaviors strongly dependent on the adsorption configurations. The characteristic Kondo temperatures T_K for the first- and second-layer individual MnPc molecules are listed in table below:

MnPc molecule	First-layer	Second-layer		
Configuration	on-surface	shifted	bridge	on-top
T_K (K)	160 ± 10	140 ± 5	105 ± 3	75 ± 2

 The Kondo temperatures for the second layer single molecules are generally lower than the one for the single molecule adsorbed directly on Ag(111) surface. Moreover, we notice that the Kondo temperature of the MnPc molecules in the second layer varies with

adsorption configurations in a considerably large range from 75 K to 140 K associated with a relative change in positions of the central Mn ion of second layer MnPc molecule with respect to that in the first monolayer. It is remarkable that the Kondo temperatures T_K only slightly decreased from 160 ± 10 K for the first layer MnPc molecule to 140 ± 5 K for the second layer MnPc molecule with shifted adsorption configuration in spite of the large increase in molecule-substrate distance. Simultaneously, the Kondo temperature for the second layer MnPc molecules changes significantly, from 140 ± 5 K for the shifted configuration to 105 ± 3 K for the bridge configuration and finally to 75 ± 2 K for the on-top configuration regardless of a similar molecule-substrate distance for all the configurations.

In addition to showing slightly different local spin moments at the Mn centers in the first- and second-layer, the local moments at the Mn centers can be parallel or anti-parallel to each other due to the magnetic exchange interaction. This corresponds to the ferromagnetic (FM) or anti-ferromagnetic (AFM) exchange coupling between the first- and second-layer MnPc molecules.

The magnetic susceptibility and magnetization measurements on the thin film of MnPc molecule (at thickness of 40-monolayer) indicated the existence of a strong intra-chain and weak inter-chain anti-ferromagnetic (AFM) exchange coupling between the magnetic moments at the Mn center of molecules [33]. Moreover, Gruber and colleagues also report an AFM ordering of MnPc molecules that is stabilize even at room temperature by the ferromagnetic cobalt substrate [12]. The ab-initio calculation for this system further confirmed that the AFM coupling is favorable for the MnPc bilayer system with the different configurations considered in their work [12].

In our present STM experiments, the three different adsorption configurations observed for the isolated second layer MnPc molecules suggests the existence of three different possible pathways for the AFM exchange interaction between Mn ions in the first- and second-layer. For the on-top adsorption configuration, this stacking geometry indicates that the most favorable pathway for the magnetic interactions between two Mn centers is the direct exchange coupling due to the effective overlap of d orbitals of central Mn ions in the first- and second-layer. For the shifted adsorption configuration, a possible pathway for the magnetic interaction between two Mn ions must be of the super-exchange type through the N atoms (i.e. N atom directly bound to the Mn ion) in phthalocyanines rings. In the bridge configuration, the magnetic interactions between one Mn ion in the second layer and the two Mn ions from the first layer is most probably of the super-exchange type through the two Pc ligands of the second layer MnPc molecule, which are bound to the two Mn ions in the first layer.

Recent ab-initio calculations [12] showed that the energetically most favorable MnPc molecule stacking geometry for the AFM exchange coupling is the on-top and then the shifted configurations with an energy difference of $E_{FM} - E_{AFM} = 33\ meV$ and $5\ meV$, respectively. From this calculation, the exchange coupling constant J/K_B [34] characteristic for the AFM interaction in the bilayer MnPc/Ag(111) can be estimated as

$J/K_B = (E_{FM} - E_{AFM})/2K_B$ corresponding to a temperature of 191 K and 29 K for the on-top and shifted configurations, respectively. The bridge configuration has not been calculated but is expected to show a J/K_B comprised between these two values due to the special AFM interaction induced by its adsorption configuration (see Section above).

On the other hand, the previous studies on the two-impurity Kondo problem [35-41] have demonstrated that the AFM coupling between impurities competes with the Kondo effect [35]. In the MnPc/Ag(111) bilayer system, the different molecular stacking configurations give rise to distinct AFM coupling between the two local spin moments at Mn ions in the first- and second-layers as indicated by the estimated exchange coupling J/K_B. For example it is predicted that the Kondo effect is suppressed when $J/K_B \gg T_K$, because the AFM interaction tends to bind the two local spins into a singlet state. In contrast, when $J/K_B \ll T_K$, the local spin on each impurity is screened by the surrounding itinerant electrons and thus forms a Kondo singlet state [35]. Recently the STM experiments have suggested that the two impurity Kondo problem depends crucially on the distance between impurities [42-44]. In the bilayer MnPc/Ag(111) system, therefore, the inter-layer separation plays a crucial role in determining the AFM coupling constant J/K_B. It is expected that J/K_B decreases rapidly with the increasing of interlayer separation.

As a remainder, we found above that for the isolated second layer MnPc molecule the Kondo temperature is increasing from T_K = 75 ± 2 K to 105 ± 3 K and 140 ± 5 K when going from the on-top, to the bridge and shifted configurations. Simultaneously, the estimated exchange coupling constant J/K_B follows the inverse law:

$$J_{shifted} < J_{bridge} < J_{on\text{-}top}$$

In coherence with the experimental fact, for the on-top MnPc molecule, the exchange coupling J/K_B dominates the Kondo effect and therefore leads to a reduced Kondo temperature of $T_K = 75 \pm 2\,K$. On the contrary, in the shifted configuration, the Kondo temperature $T_K = 140 \pm 5\,K$ is much larger than the weak AFM super-exchange coupling $J/K_B = 29\,K$ between the Mn ions and therefore the Kondo state is largely preserved. The situation of the bridge configuration is somehow intermediate between the shifted and on-top configuration.

The strong dependence of the Kondo temperature on the adsorption configuration of the MnPc molecules in the second layer indicates that the strength of AFM exchange coupling between Mn ions in the adjacent layer is significantly changed from configuration to configuration. In the on-top configuration, the stronger AFM direct coupling leads to the lower Kondo temperature. When the adsorption geometry changes from the on-top configuration to the shifted configuration, the overlap of the upper Mn d orbitals with that of the lower one moves from the electron-rich Mn atom towards to the N with less dense electron. As a result the AFM coupling changes into a super-exchange type and the coupling becomes weaker compared to the direct coupling in the on-top situation. Thus the weaker AFM coupling leads to a higher Kondo temperature. In the bridge configuration, one Mn ion in upper layer AFM couple to the two Mn ions in the lower layer through the

two bridging ligands, then this super-exchange interaction would be an intermediate strength compared with the exchange coupling for the on-top and shifted configurations. Thus, this intermediate coupling strength gives a Kondo temperature between that for the on-top and parallel configurations.

4.3.2 MnPc molecules inside the second layer island

As shown previously in Section 4.1.2 the MnPc molecules self-assemble into the ordered molecular islands on top of the first monolayer (see Figure 4.3). In this section we will investigate further the spectral evolution of the Kondo resonance of MnPc molecules within the second layer island.

The dI/dV spectrum measured over the central Mn ion of MnPc molecule inside the second layer island exhibits a pronounced zero-bias peak with a weak shoulder just above the Fermi level, which is absent on the second layer isolated molecule and the first layer molecule (see the black curves (i), (ii) and (iii) in Figure 4.9(a)). Compared to the tunneling spectra of the isolated second layer MnPc molecule, especially the one in the shifted configuration (see the black curve (ii) in Figure 4.9(a)), the MnPc molecules inside the second layer island exhibited a much broader and more complex spectroscopic feature, indicating the presence of strong inter-molecular (inter-layer as well as intra-layer) interactions between molecules in the bilayer MnPc/Ag(111) system. The existence of strong inter-molecule interactions within the second layer island was also evidenced by the wide range STS spectra for the second layer molecules with varying the number of nearest neighbors (see Section 4.2).

For a MnPc molecule inside the second layer island, the presence of nearest neighboring molecules as well as the shifted and tilted adsorption geometry hints at the existence of more complex pathways for the super-exchange type magnetic interactions between the Mn ions in the first- and second-layer. Compared to the isolated shifted molecule, each individual MnPc molecule inside second layer island has the possibility to couple anti-ferromagnetically (AFM) with the first layer molecule underneath as well as with its nearest neighboring molecules in the second layer.

Therefore, the possible pathways for the AFM exchange interactions between Mn ions in the bilayer MnPc/Ag(111) system are as follows: (i) a super-exchange interaction between the first- and second-layer molecule through the N atoms (i.e. the one directly bound to the Mn ion) induced by the lateral shift of molecule. (ii) another super-exchange type interaction between Mn ions in the nearest neighbor molecules in the second layer through the overlapped Pc ligands induce by the tilting configuration of molecule. The sum of these super-exchange interactions might be give rise to a strong AFM exchange interaction in the bilayer MnPc/Ag(111) system. This stronger AFM exchange coupling of a molecule inside the second layer island to its neighboring molecules (i.e. including both the first- and second-layer molecules) leads to the splitting of Kondo peak at the Fermi level (see the spectrum (iii) in Figure 4.9(a)).
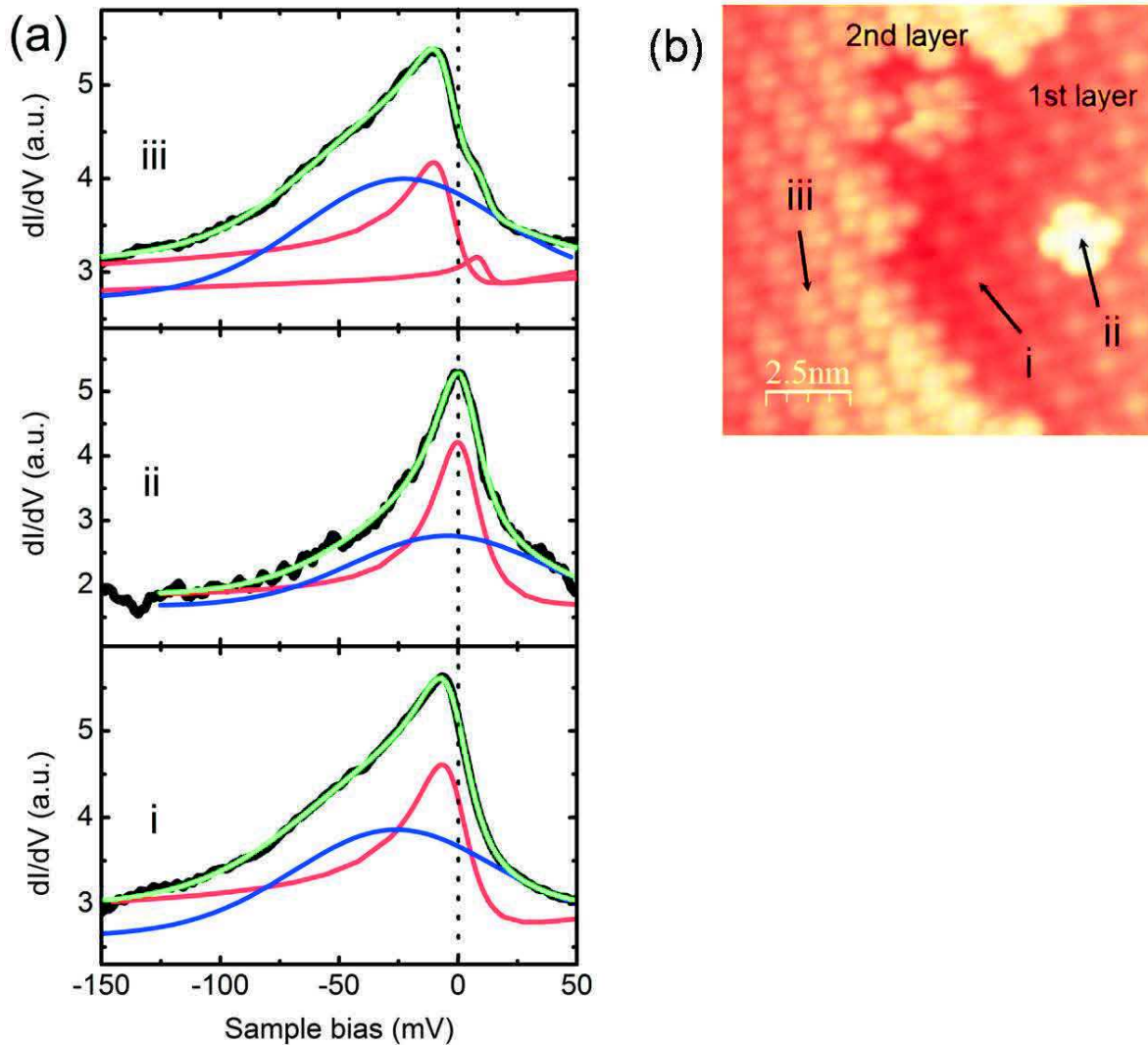
Figure 4.9 (a) dI/dV spectra acquired at the center of (i) MnPc molecule in the first monolayer, (ii) isolated MnPc in the second layer and (iii) MnPc inside the second layer island as indicated by the small arrows in (b). (b) STM image of bilayer MnPc molecules on Ag(111).

Thus the spectrum (iii) in Figure 4.9(a) was fitted by the superposition (green) of two Fano (red) and one Gaussian (blue) functions modeling the splitting of Kondo resonance and an occupied molecular orbital, respectively. The curve fitting determines the energy width at half-maximum of $\Gamma_1 = 11 \pm 0.2\ \mathrm{meV}$ and $\Gamma_2 = 5.1 \pm 0.2\ \mathrm{meV}$ for the Kondo peaks below and above the Fermi level, respectively. While the line shape fitting parameters are the same and equal to $q = -1.97 \pm 0.1$. The corresponding Kondo temperatures are determined to be $T_{k1} = \Gamma_1/k_B = 125 \pm 3\ K$ and $T_{K2} = \Gamma_2/k_B = 60 \pm 3\ K$ for the Kondo resonance below and above the Fermi level, respectively. The Kondo temperature T_{K1} for the MnPc molecule inside island is only slightly lower than $T_K = 140 \pm 5K$ for the isolated single MnPc with parallel configuration, while it is considerably lower than $T_K = 160 \pm 10\ K$ the one for the first layer MnPc molecule (see Figure 4.9(a)).

To get a deeper insight into the influence of nearest-neighboring molecules on the Kondo peak, the zero-bias Kondo feature of the MnPc molecule inside the second layer island was studied as a function of the number of nearest-neighbor (NN) molecules, i.e. N_{nn} as shown in Figure 4.10(a) and (b). While the MnPc molecule at the corner (N_{nn} = 2) display a zero-bias Kondo peak with a very weak shoulder-like feature, the shoulder becomes gradually more evident when the number of nearest neighboring molecules changes from N_{nn} = 2 to N_{nn} = 3 and N_{nn} = 4; at the same time the overall width of peak feature slightly broadens as shown in Figure 4.10(a). To determine the corresponding Kondo temperature, these dI/dV spectra are fitted with the same procedure used to fir the curve (iii) in Figure 4.9(a). The curve fitting results show that the Kondo temperature T_{k1} slightly reduces from $125 \pm 5\,K$ for the MnPc molecule with N_{nn} = 2 to $110 \pm 5\,K$ the one for the molecule with N_{nn} = 4, and simultaneously the Kondo temperature T_{k2} increases from $40 \pm 3\,K$ to $65 \pm 5\,K$. The observed change in the Kondo temperature suggesting that the strength of the AFM exchange interaction changes with the number of the nearest neighboring molecules.

Moreover, we investigated further the spectral dependence on the local position of the molecule within the second layer island. The Figure 4.10(c) shows the dI/dV spectra of the MnPc molecules labeled from 1 to 8 as shown in Figure 4.10(b). An important observation here is that the overall width and intensity of the spectral feature changes from molecule to molecule. The curve fitting results show that the variation of dI/dV spectra in Figure 4.10(c) corresponds to the oscillation of Kondo temperature T_{k1} in a range from 110 K to 130 K as shown in the upper panel of Figure 4.10(d). Simultaneously the Kondo temperature T_{k2} also varies in an oscillatory manner within the range from 40 K to 65 K as shown in the lower panel of Figure 4.10(d). In the second layer MnPc island, indeed, the Kondo temperature are distributed over a wide temperature range, which include the Kondo temperatures for isolated molecule with three different configurations.

As we discussed in Section 4.3.1, in the bilayer MnPc/Ag(111) system the Kondo effect and the AFM exchange coupling are competing with each other. The stronger the exchange coupling the lower the Kondo temperature. In fact, the large variation of the Kondo temperature with the adsorption configuration of second layer molecules is a result of the strong dependence of the AFM exchange coupling on the relative position of Mn ion in the second layer with respect to that in the first layer (see Section 4.3.1). Thus, the observed variation of Kondo temperature for the molecules inside the second layer island (see Figure 4.10(d)) is mainly due to the change in the strength of the AFM exchange coupling rather than other relevant factors.
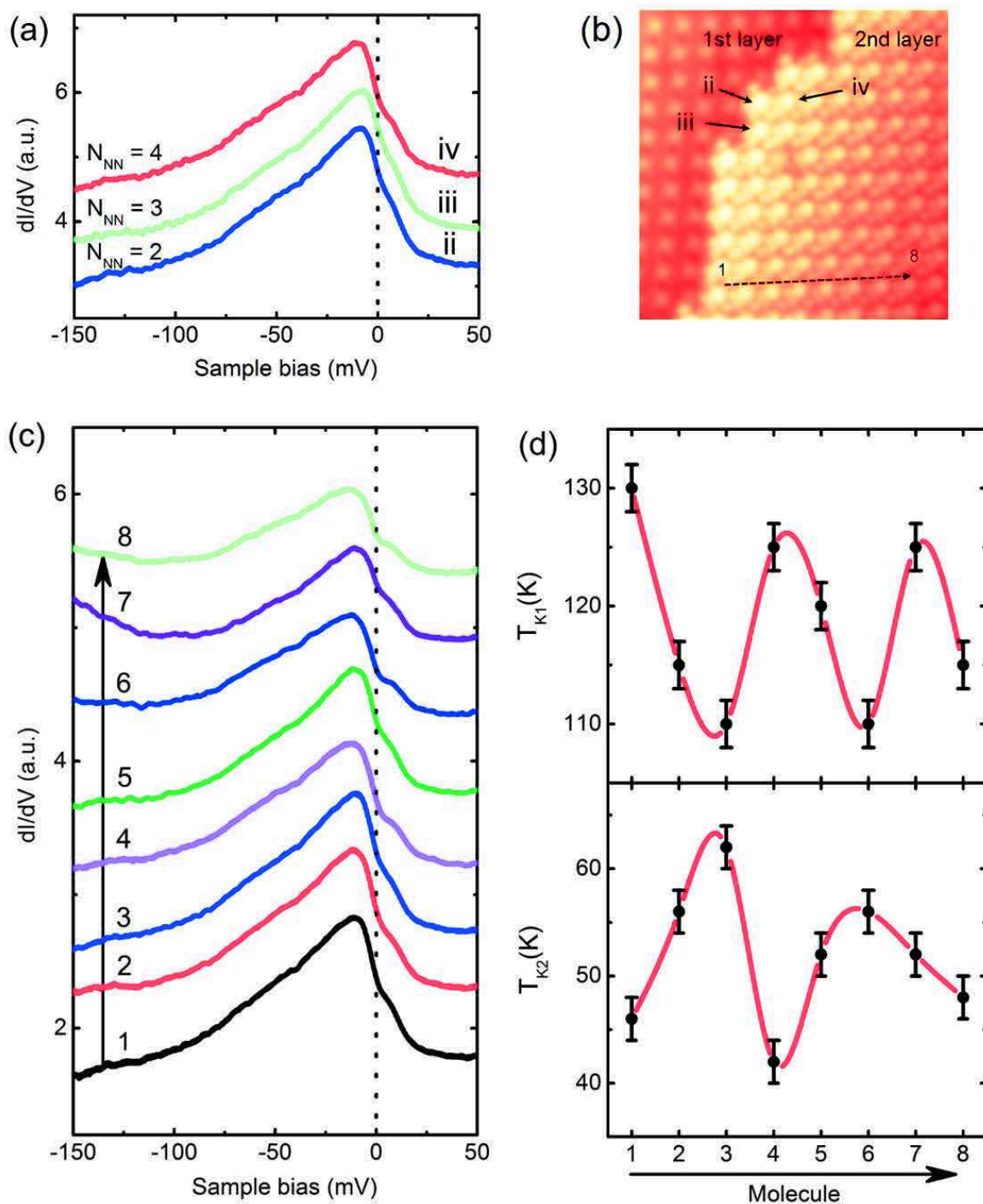
Figure 4.10 (a) dI/dV spectra on the center of MnPc molecules in the second layer with different number of nearest neighbors as indicated by small arrows in (b) STM image of bilayer MnPc molecules on Ag(111). (c) dI/dV spectra and (d) the Kondo temperature on the center of second layer MnPc molecules labeled from 1 to 8 in (b).
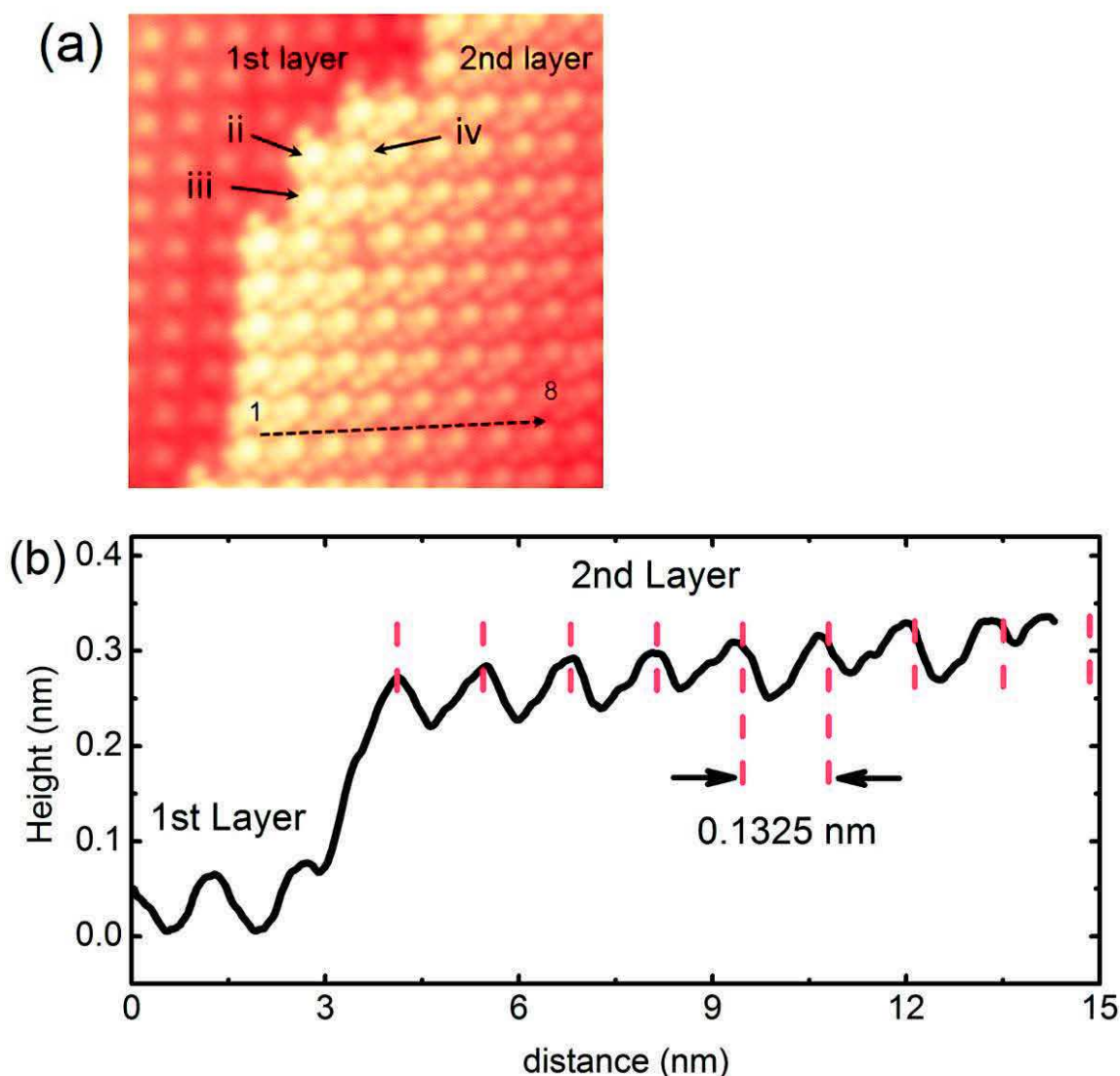
Figure 4.11 (a) STM image of bilayer MnPc molecules on Ag(111). (b) The topographic line profile measured over the MnPc molecules labeled from 1 to 8 in (a) across the molecular bilayer island. The red grid lines are representing the first-layer molecular lattice when imposing a zero offset with the second layer molecular lattice.

On the other hand, the spectral dependence on the local position of molecule within the second layer island (see Figure 4.10(c)) is a direct result of the small deviation in the Mn ion in the second layer respect to that in the first layer as we can know from the topographic line profile shown in Figure 4.11(b). There is a varying phase shift of the second layer molecules with respect to the first layer grid that increases with the distance from the edge of the island (see Figure 4.11(b)). The incommensurate second layer was already discussed in section 4.1.2. Such a deviation in the central ion position leads to large change in the AFM exchange coupling in the bilayer MnPc/Ag(111). Therefore, the variation of the Kondo temperature is mainly due to the change in the AFM coupling in this system.

References

[1] X. H. Qiu, G. V. Nazin, W. Ho, Phys. Rev. Lett. 92, 206102 (2004)

[2] K. J. Franke, G. Schulze, N. Henningsen, et al Phys. Rev. Lett. 2008, 100, 036807

[3] A. J. Heinrich, J. A. Gupta, C. P. Lutz, D. M. Eigler, Science 306, 466(2004)

[4] K. J. Franke, J. I. Pascual, J. Phys.: Condens. Matter 24, 394002 (2012)

[5] F. Matino, G. Schull, F. Köhler et al Proc. Natl. Acad. Sci. U. S. A. 108, 961 (2011)

[6] X. Ge, J. Kuntze, R. Berndt, H. Tang et al Chem. Phys. Lett. 458, 161(2008)

[7] R. Staub, M. Toerker, T. Fritz, F. Sellam, K. Leo, Surf. Sci. 445, 368 (2000)

[8] M. Takada, H. Tada, Chem. Phys. Lett. 392, 265 (2004)

[9] T. G. gopakumar, T. brume, J. Kroger et al J. Phys. Chem. C 115, 12173 (2011)

[10] N. Ohta, R. Arafune, N. Tsukahara et al J. Phys. Chem. C 117, 21832 (2013)

[11] X. Chen, Y.-S. Fu, S.-H. Ji, T. Zhang et al Phys. Rev. Lett. **101**, 197208 (2008)

[12] Gruber, M.; et al. Nat. Mater. 14, 981 (2015)

[13] M. Topyła, N. Néel*, and J. Kröger *Langmui,* 32, 6843 (2016)

[14] T. G. Gopakumar, T. Brumme et al J. Phys. Chem. C **115**, 12173 (2011)

[15] A. Scarfato, S. H. Chang, J. Brede et al Surf. Sci. 602, 677 (2008)

[16] M. Takada, H. Tada, Chem. Phys. Lett. 392, 265 (2004)

[17] I. E. Brumboiu, S. Haldar et al J. Chem. Theory. Comput. 12, 1772 (2016)

[18] R. Mason, G. A. Williams et al J. Chem. Soc., Dalton Trans. 676, (1979)

[19] F. Ruckerl, B. Mahns, E. Dodbiba et al J. Chem. Phys. 145, 114702 (2016)

[20] Rajesh, K.; Mnon, C. S. Eur. Phys. J. B 47, 171 (2005)

[21] E. Minamitani, Y. S. Fu, Q. K. Xue, Y. Kim et al Phys. Rev. B 92, 075144 (2015)

[22] T. Inabe and H. Tajima, Chem. Rev. **104**, 5503 (2004)

[23] N. Hanasaki, H. Tajima, M. Matsuda, et al Phys. Rev. B **62**, 5839 (2000)

[24] D. E. C. Yu, M. Matsuda, H. Tajima et al Mater. Chem. **19**, 718 (2009)

[25] C. Hotta, M. Ogata, and H. Fukuyama, Phys. Rev. Lett. **95**, 216402 (2005)

[26] R. Kraus, M. Grobosch, and M. Knupfer, Chem. Phys. Lett. **469**, 121 (2009)

[27] P. A. Reynolds and B. N. Figgis, Inorg. Chem. **30**, 2294 (1991)

[28] C. Arrigo, F. Andrea, N. M. Buongiorno, Nanotechnology **18**, 424013 (2007)

[29] M. Gruber, F. Ibrahim, S. Boukari, et al *Nano. Lett.* **15**, 7921 (**2015**)

[30] C. H. Booth, M. D. Walter, M. Daniel et al Phys. Rev. Lett. **95**, 267202 (2005)

[31] B. W. Thimm, J. Kroha, J. von. Delft, Phys. Rev. Lett. 82, 2143 (1999)

[32] D. E. Liu, S. Burdin, H. U. Baranger et al Phys. Rev. B 85, 155455 (2012)

[33] H. Yamada, T. Shimada, A. Koma. J. Chem. Phys. 108, 10256 (1998)

[34] A. N. Rudenko, V. V. Mazurenko et al Phys. Rev. B 79, 144418 (2009)

[35] P. Wahl, P. Simon, L. Diekhöner et al Phys. Rev. Lett. 98, 056601 (2007)

[36] A. N. Rudenko, V. V. Mazurenko et al Phys. Rev. B 79, 144418 (2009)

[37] B. A. Jones and C. M. Varma Phys. Rev. Lett. 58, 843 (1987)

[38] B. A. Jones and C. M. Varma Phys. Rev. Lett. 61, 125 (1988)

[39] B. A. Jones and C. M. Varma Phys. Rev. B 40, 324 (1989)

[40] W. Chen, T. Jamneala, V. Madhavan et al Phys. Rev. B 60, R8529(R) (1999)

[41] D. Wegner, Ryan Yamachika Phys. Rev. Lett. 103, 087205 (2009)

[42] N. Neel, R. Berndt, J. Kroger et al Phys. Rev. Lett. 107, 106804 (2011)

[43] J. Bork, Y.-h. Zhang, L. Diekhoner et al Nat. Phys. 7, 901 (2011)

[44] H. Pruser, P. E. Dargel, M. Bouhassoune et al Nat. Commun. 5, 5417 (2014)

Chapter 5

Co doping of MnPc monolayer on Ag(111)

The magnetic properties of metal phthalocyanine (MPc) molecules are strongly influenced by the interaction with the metal substrates [1-7], other molecules [8] and with magnetic atoms [9-10]. Particularly the manipulation of MPc spin state by specific doping with atoms is an attractive method to achieve desirable magnetic properties of the molecules. In this Chapter, we will present the adsorption structures and magnetic properties of the MnPc molecule doped with Co atom, denoted as Co@MnPc hereafter, on Ag(111) by means of low-temperature scanning tunneling microscopy (STM) and scanning tunneling spectroscopy (STS) measurements. More importantly, by probing the Kondo effect using STM, we investigated a number of interesting magnetic properties of the several different Co@MnPc complexes on Ag(111) surface. By monitoring the evolution of Kondo effect, we found that the Co atom adsorption site plays an important role in tuning the exchange coupling between the magnetic moments of the MnPc molecule and the Co atom.

5.1 MnPc monolayer doped with Co atoms

To investigate the doping of the MnPc molecule on Ag(111) with the magnetic Co atom, a MnPc monolayer was first formed by the deposition of molecules on Ag(111) substrate. As shown in Figure 5.1(a), the MnPc molecules completely cover the surface and form a self-assembled ordered monolayer with a square lattice. The individual MnPc molecule (i.e. undoped ones) in the monolayer structure appear as clearly visible four-lobe patterns with a bright protrusion in the center, accounting for flat lying of MnPc molecules. In addition, all the MnPc molecules in the monolayer have the same azimuthal orientation and the molecular axes are aligned with the $[10\bar{1}]$ and $[1\bar{2}1]$ high symmetry directions of the underlying Ag(111) surface as shown by the arrows in the Figure 5.1(a).

Subsequently, we deposited a small amount of Co atoms (~ 0.05 ML) on top of the ordered monolayer while keeping the sample at room temperature. The limited thermal diffusion length of Co atoms over the molecular monolayer structure prevents them to form clusters. More importantly, the spontaneous on-surface reaction of Co atoms with the monolayer of MnPc molecule allows us to obtain individual MnPc molecules doped with a single Co atom under room temperature condition. The interaction of the Co atom with the MnPc molecule leads to several stable Co@MnPc configurations. The most frequent configurations are presented in the STM images shown in Figure 5.1(a) and (c) labeled (i) to (vi). Among them, the configurations from (i) to (iv) exhibit a very bright protrusion on

one of the molecule Pc lobes (see Figure 5.1(a)). Configuration (v) in Figure 5.1(c) shows a dimmer protrusion on the Pc lobe compared to the configuration (i) in Figure 5.1(a). However, the Co@MnPc with configuration (vi) and the one enclosed by the dashed ellipse in Figure 5.1(c) exhibit a bright protrusion at the position between two neighboring MnPc molecules.
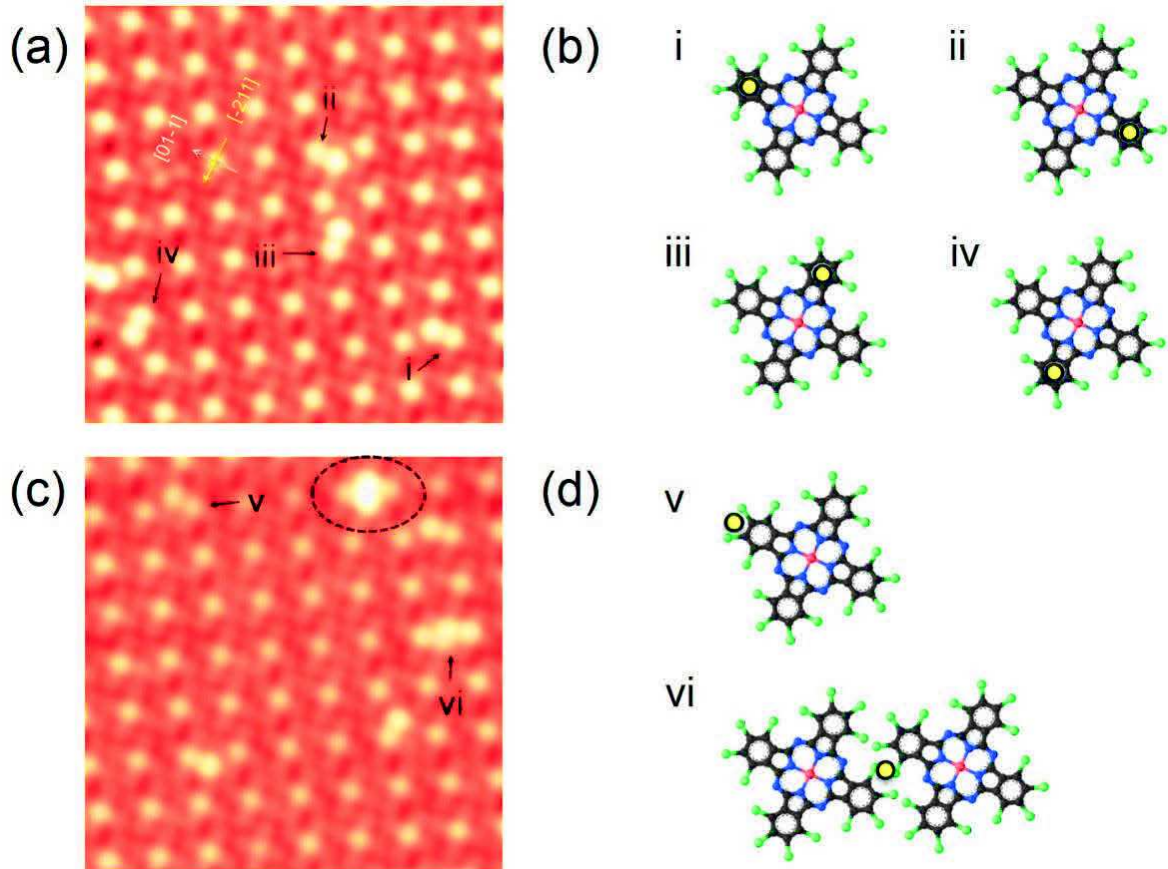

Figure 5.1 (a) and (c) are STM images of MnPc monolayer on Ag(111) surface after doping with Co atoms. (b) and (d) are the proposed geometrical configurations for the different types of Co@MnPc complexes marked from (i) to (vi) in (a) and (c).

 From the high-resolution STM image of Figure 5.1(a), it can be unambiguously conclude that the bright protrusion on the Pc ligand of Co@MnPc complex with configuration (i)-(iv) is due to one Co atom interacting with one of the benzene rings of the MnPc molecule. In the configuration (vi) in Figure 5.1(c), however, the Co atom seem to be interacting with the two benzene rings. When two Co atoms interact with MnPc molecules, a large and bright protrusion is seen between two neighboring molecules as shown by the Co_2@MnPc complex enclosed by the dashed ellipse in Figure 5.1(c). Moreover, the other configurations where the Co clusters (more than two Co atoms) interacting with the two neighboring MnPc molecules are also observed (not shown here).

A closer view into the high-resolution STM image of the most stable Co@MnPc structure with configuration (i)-(iv) in Figure 5.1(a) shows that the location of Co atom seems to be under the benzene ring of MnPc, which is the most stable bonding site for dopant atoms [11]. This adsorption site for the Co atom is also suggested by the topographic signature of bright protrusion on the benzene ring which is different from the circular protrusion for Co atoms on Ag(111) [12]. It should be noted that the doping sites of Co atoms in configurations (i) and (ii) are located on the same molecular axis which is aligned with the $[10\overline{1}]$ high symmetry directions of Ag(111), while for the configurations (iii) and (iv) the Co atoms are adsorbed on the orthogonal molecular axis which is aligned with $[1\overline{2}1]$ direction of the surface (see Figure 5.1(b)). As we will see in the next section the different adsorption site of Co atom plays an important role in tuning the magnetic properties of those Co@MnPc complexes.

For the less stable Co@MnPc with configurations (v) and (vi) in Figure 5.1(c), however, the STM image shows that the Co atom is no longer locates exactly under the benzene ring of MnPc molecule, and seems to deviate from this stable bonding site. In fact, a careful inspection of the STM topography image in Figure 5.1(b) suggests that the Co atom is located slightly away from the benzene ring along the molecule axis in the configuration (v), while for Co@MnPc with configuration (vi) the Co atom is located at the position between two benzene rings of neighboring molecules (see Figure 5.1(d)). These differences in the adsorption site of Co atoms are further supported by the tunneling spectroscopy measurements on the Co@MnPc structures, as we will see later. Moreover, it should be emphasized at this point that the rotational stability of the Co@MnPc within the monolayer structure does not seem to be affected by the doping with Co atom, and hence for all the configurations has no significant deviation from the azimuthal orientation of the undoped MnPc (see Figure 5.1).

5.2 Magnetic properties of Co doped MnPc molecules

In this section, we will investigate the magnetic properties of Co@MnPc complexes on Ag(111) by probing the Kondo effect through the differential conductance (dI/dV) spectroscopy measurements. More importantly, the evolution of the Kondo behavior with Co atom doping allows us to study the influence of Co atom adsorption site on the exchange interaction between the magnetic moments of the MnPc molecule and the Co atom.

In the Figure 5.2, we illustrate the Co@MnPc complexes with configuration from (i) to (vi) together with the corresponding dI/dV spectra taken at the doping site in each configuration. As can be seen in Figure 5.2, the dI/dV spectral feature strongly depends on the adsorption site of Co atom within Co@MnPc complex. Firstly, we will discuss the dI/dV spectra obtained on the configurations (v) and (vi) which are very similar to the prototypical Kondo spectrum observed for Co atom on bare Ag(111) surface [12]. These results are used as a reference spectrum to be compared with the STS results obtained

for the configurations (i)-(iv). Then, we will discuss further the dependence of Kondo behavior on the adsorption site of Co atom in Co@MnPc complexes. These systematic spectroscopic investigations will provide a deeper and more comprehensive understanding of the various spin couplings between the magnetic moments of the MnPc molecule and the one of the Co atom.

 The dI/dV spectra acquired over the doping site of Co@MnPc with configuration (v) and (vi) exhibit a dip-like symmetric zero-bias resonance as shown in Figure 5.2(b) while the dI/dV spectra recorded over the undoped Pc lobes of the same Co@MnPc complex is flat and featureless over the voltage ranges of interest here (not shown). These zero-bias dip-like resonances in Figure 5.2(b) can be attributed to the Kondo effect with Fano line shape, in analog to the case of Kondo resonance for the organo-metallic molecular Kondo system [5, 9,13]. The curve fitting to dI/dV spectra with the Fano function (see Figure 5.3(a)) gives an average Kondo line width of $\Gamma = k_B T_K = 6.5 \pm 0.3 \ meV$ and the line shape factor of $q = 0.003 \pm 0.001$. The line width of Kondo resonance defines a Kondo temperature of $T_K = 75 \pm 5 \ K$, which is very close to the Kondo temperature $T_K = 83 \pm 10 \ K$ observed for the Co atom on a bare Ag(111) surface [12]. This suggesting that the interaction of Co atom with the Pc lobe of MnPc molecule is fairly weak in Co@MnPc complexes with configuration (v) and (vi).

More interestingly, the dI/dV spectra measured over the Co atom in Co@MnPc with configuration (i) and (ii) show a pronounced peak at zero-bias (see Figure 5.2(d)). This resonance can also be attributed to the Kondo effect with a Fano line shape, similar to the case of the Kondo resonance in a molecular system [5, 13, 14]. The curve fitting to these peaks with Fano function (see Figure 5.3 (b)) gives the following value, $\Gamma = k_B T_K = 16 \pm 1 \ meV$ and $q = 3.7 \pm 0.3$. It is noted that the Kondo line width for Co@MnPc with configuration (i) and (ii) defines a Kondo temperature of $T_K = 180 \pm 10 \ K$, which is higher than that of the configuration (v) and (vi) with $T_K = 75 \pm 5 \ K$. At the same time, the Fano line shape factor q increased from 0.003 ± 0.001 for the configuration (v) to 37 ± 2 for configuration (i) corresponding to a change in the Fano line shape from a dip-like to a peak-like resonance, which may be ascribed to the enhanced tunneling from STM tip to the Co dopant atom in the case of configuration (i) due to a new coupling channel via the orbital hybridization between the d orbitals of Co and the π orbitals of molecular Pc ligand in Co@MnPc, which is similar to previous studies on the metal-molecule complexes [9,13,15]. This orbital hybridization might be also responsible for the observed dramatic change in Kondo behavior of Co@MnPc complexes with configuration (i) and (ii).
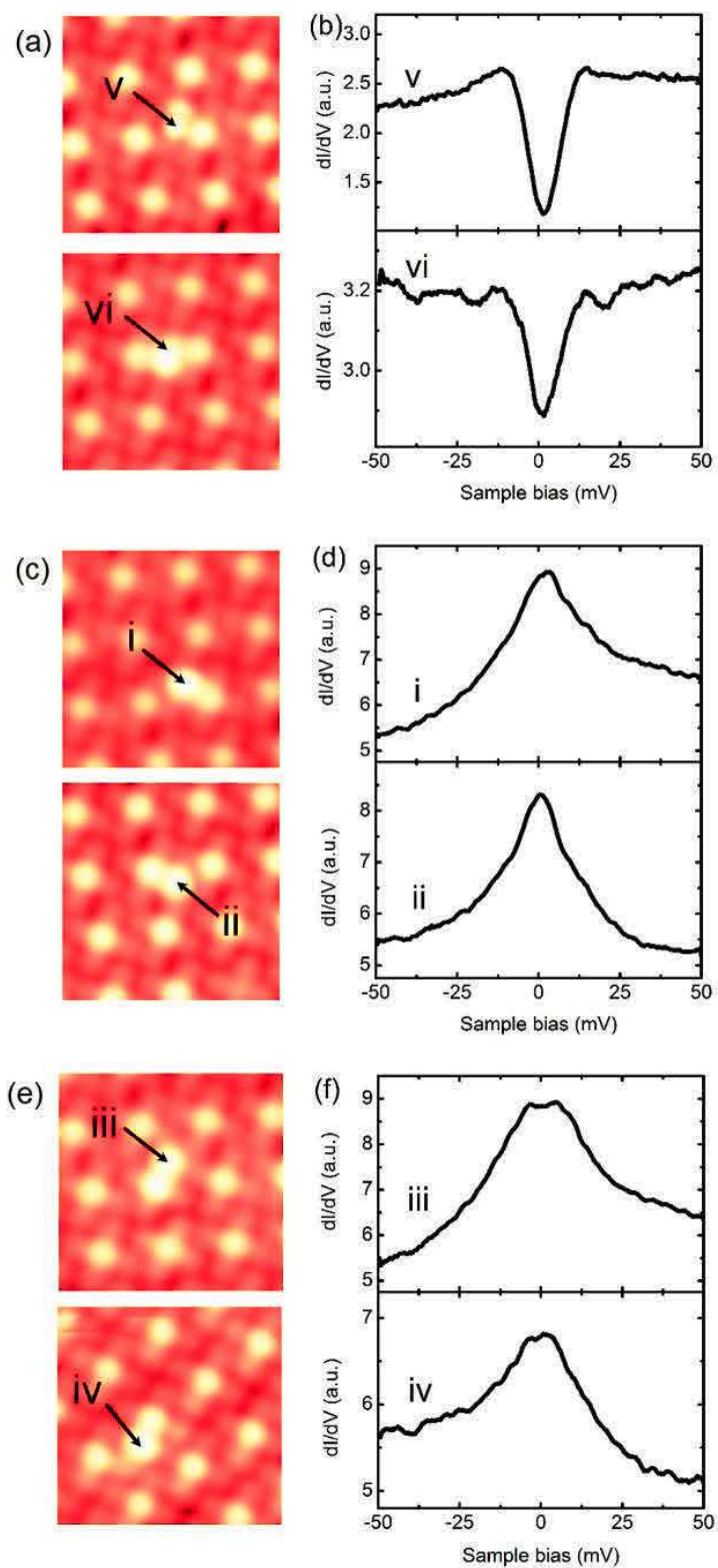
Figure 5.2 (b), (d) and (f) are the dI/dV spectra taken on the Co dopant site of different Co@MnPc configurations from (i) to (vi) as indicated by the arrows in the STM images (a), (c) and (e).

The situation dramatically changes in dI/dV spectra measured over the Co atom in Co@MnPc with configuration (iii) and (iv) where the Co atoms are located beneath the Pc lobes orthogonal to the case in configuration (i) and (ii) as shown in Figure 5.2. The broad peak-like resonances at the Fermi level (see Figure 5.2(f)) show line shapes and line widths quite different from those observed on the other four configurations. By taking a close look at the dI/dV spectra in Figure 5.2(f), we can observe that both resonances have a double-peak structure around the Fermi level and the energy separation between the two peaks is approximately 7 ± 1 meV. This Kondo peak splitting in Co@MnPc with configurations (iii) and (iv) is analogous to the influence of an external magnetic field on the Kondo resonance due to the Zeeman effect [16-17] (see Section 1.4). More importantly, it has been shown that the spin coupling could break the spin symmetry of a Kondo system and split apart its resonance [18-19]. As a result, the observed Kondo peak splitting provides an evidence for the magnetic coupling of Co atom to the MnPc molecule.

By exploiting the Kondo effect in the *dI/dV* spectroscopy a number of interesting studies on the magnetic interaction between impurities has been reported. For example, previous STM experiment reported that the anti-ferromagnetic coupling between Fe atom and a Kondo screened Co atom on Cu_2N leads to a split Kondo resonance [20]. For Co_2 dimers on Au(111), however, the disappearance of the Kondo resonance has been explained by the reduced Kondo coupling between the substrate's conduction electrons and the ferromagnetic cobalt dimers [21]. Based on these previously reported results, we can conclude that the observed zero-field splitting of Kondo resonance in Figure 5.3(b) implies an anti-ferromagnetic (AFM) coupling of the magnetic moment of Co atom to that of Mn ion within Co@MnPc complex with configurations (iii) and (iv). Most importantly, the alteration of the Kondo profile from a dip to a peak and finally its splitting upon changing the doping site in Co@MnPc complexes (see Figure 5.3(b)) may suggest a variation of couplings between the magnetic moments of the Co atom and MnPc molecule.

To quantitatively analyze the zero-field splitting of Kondo resonance in Co@MnPc with configuration (iii), we have fitted the dI/dV spectra by the two Fano functions to describe the Zeeman splitting in the dI/dV spectra. The sum of two Fano functions:

$$\frac{dI}{dV}(V) = A \times F(V) + B \times F\left(V - \frac{\Delta}{e}\right) + C \qquad (5.1)$$

$$F(V) = \frac{(\varepsilon + q)^2}{1 + \varepsilon^2} \qquad (5.2)$$

where $\varepsilon = (eV - \varepsilon_0)/\Gamma$ is the normalized energy (ε_0 is the position of the resonance and Γ is the HWHM of the Kondo peak, which is related to the Kondo temperature T_K as $\Gamma \sim k_B T_K$ at low temperatures). Δ is the Zeeman splitting energy of the Kondo peak, and q is the Fano asymmetry factor. The curve fitting (see the curve (iii) in Figure 5.3(b)) determines $\Gamma = 27 \pm 1\ meV$, $q = 2.9$ and $\Delta = 7.5 \pm 0.5\ meV$. It defines a Kondo temperature of $T_K = 310 \pm 10\ K$. From the exchange splitting expression: $\Delta = 2g\mu_B B$, we estimate an effective magnetic field of 30 T exerted on Co atom due to its magnetic coupling with the Mn ion in the Co@MnPc complex in configuration (iii).
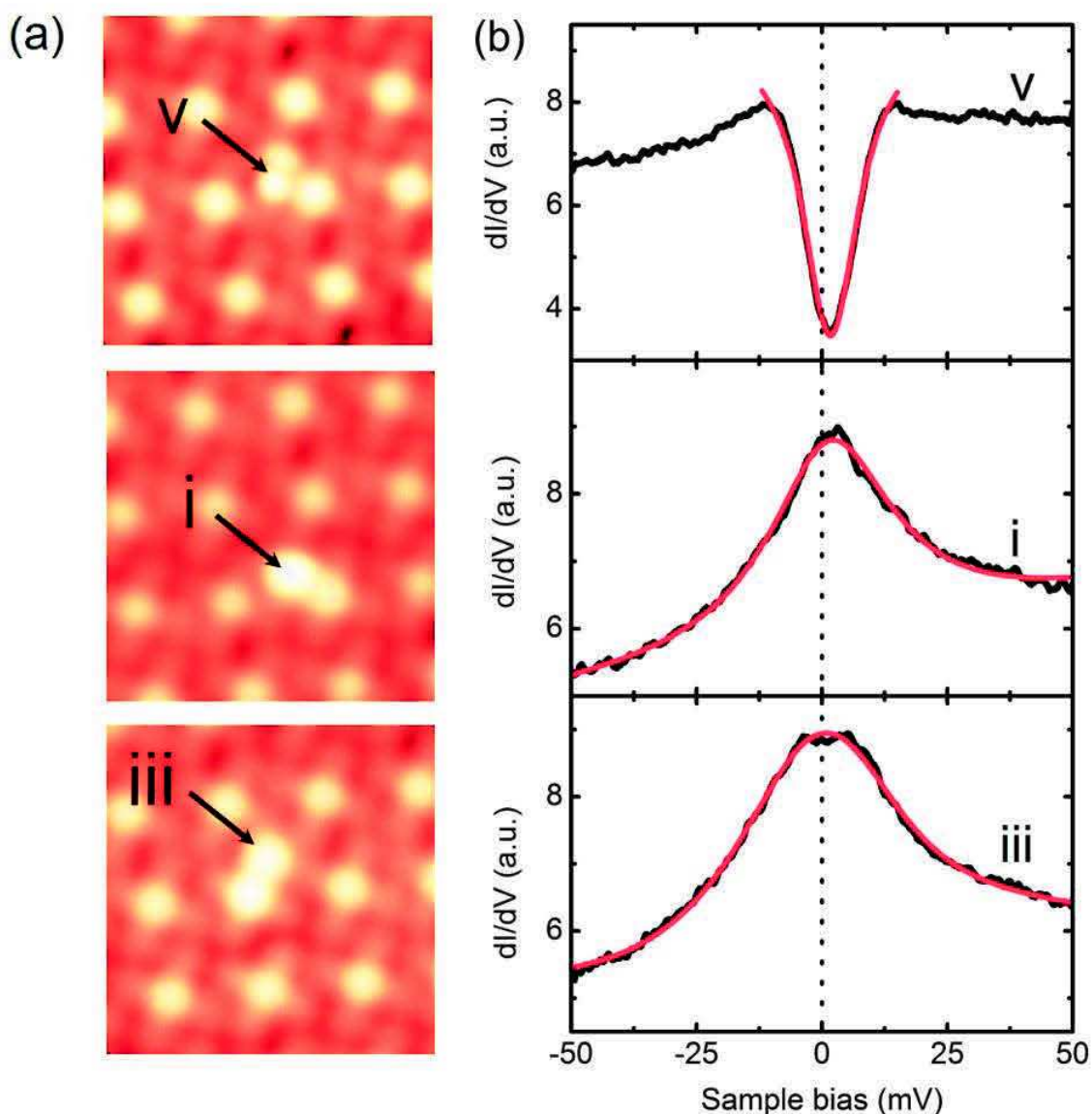
Figure 5.3 (b) the Kondo resonance spectra (black curve) taken on the representative Co@MnPc complexes with configurations (i), (iii) and (v) in STM image (a). The red lines in (b) are the Fano function fit to the spectra.

The adsorption configuration of Co@MnPc complexes (see Figure 5.1) hints the existence of two possible channels for the indirect exchange coupling between the magnetic moments of the Co dopant atom and the Mn ion of these complexes. One channel is via the Pc ligand of molecule, and the other is via the underlying Ag substrate. The former channel is a general indirect super-exchange interaction [22-23], but no explicit and simple rule is available to evaluate the Co atom's adsorption site dependence of this super-exchange interaction since the multiple 3d orbitals of Co and Mn, and the π-orbitals of the Pc ligand are involved in this interaction channels. Previous studies showed that in special cases the distance-dependence of the indirect super-exchange interaction can be

established [24-26]. The latter interaction channel is the case for the well-known Ruderman-Kittle-Kasuya-Yosida (RKKY) interaction, which is oscillating and quickly decays as a function of the distance between the magnetic impurities [27]. In the case of Co@MnPc with configuration (v) (see Figure 5.3), however, a negligible magnetic coupling between the Co atom and the Mn ion is anticipated for this channel, since the Co-Mn distance of $d = 7.5 \pm 0.5\,\text{Å}$ in this configuration is far beyond a strong magnetic coupling regime of the RKKY interaction [28], and thus the Co atom exhibit a Kondo dip, like the Co atom on bare Ag(111) surface. Even though the Co-Mn distance is slightly changed in the configuration (i) (see Figure 5.3), the Co-Mn magnetic coupling strength through the RKKY channel is expected to be still fairly weak or negligible. Although the Kondo temperature is increased for the Co atom, it remained same on the Mn ion in the Co@MnPc with configurations (v) and (i), and we observe no direct evidence of magnetic coupling between the Co and the Mn through the RKKY interaction for these configurations.

On the other hand, the Kondo effect measurements on Co@MnPc with configuration (iii) and (iv) (see Figure 5.2) provide a strong evidence for the considerable change in the magnetic exchange coupling and development of anti-ferromagnetic coupling between the magnetic moments of the Co atom and Mn ion. This result might be a consequence of an indirect super-exchange coupling of the Co atom and Mn ion through the Pc ligand of MnPc molecule, while only a negligibly small contribution from the RKKY interaction via the Ag substrate.

References

[1] Y.-S. Fu, S.-H. Ji, X. Chen, X.-C. Ma, R. Wu, et al Phys. Rev. Lett. 99, 256601 (2007)

[2] Z. Hu, B. Li, A. Zhao, J. Yang, J. G. Hou, J. Phys. Chem. C 112, 13650 (2008)

[3] L. Gao, W. Ji, Y. B. Hu, Z. H. Cheng, et al Phys. Rev. Lett. 99, 106402 (2007)

[4] N. Tsukahara, K. ichi Moto, M. Ohara, et al Phys. Rev. Lett. 102, 167203 (2009)

[5] A. Zhao, Q. Li, L. Chen, H. Xiang, W. Wang, et al Science 309, 1542 (2005)

[6] B. W. Heinrich, C. Iacovita, T. Brumme, D.-J. Choi, et al J. Chem. Lett. 1, 1517 (2010)

[7] C. Iacovita, M. V. Rastei, B. W. Heinrich, et al Phys. Rev. Lett. 101, 116602 (2008)

[8] N. Tsukahara, S. Shiraki, S. Itou, N. Ohta, et al Phys. Rev. Lett. 106, 187201 (2011)

[9] J. Li, B. Li, Y. Wang, A. Zhao, B. Wang, J. Chem. Phys. 143, 034701 (2015)

[10] Cornelius Krull, PhD thesis 2012, Universitat Autonoma de Barcelona

[11] C. Krull, R. Robles, A. Mugarza and P. Gambardella, Nat. Mater. 12, 337 (2013)

[12] L. Limot. R. Berndt Applied Surface Science 237, 576 (2004)

[13] C. Zhou, H. Shan, B. Li, A. Zhao, B. Wang, J. Appl. Phys. Lett. 108, 171601 (2016)

[14] V. Iancu, K. F. Braun, K. Schouteden Phys. Rev. Lett. 113, 106102 (2014)

[15] L. G. G. V. Dias da Silva, M. L. Tiago, et al Phys. Rev. B 80, 155443 (2009)

[16] A. F. Otte, M. Ternes, K. von Bergmann, et al Nature Physics 4, 847 (2008)

[17] Y.-h. Zhang, S. Kahle, T. Herden, C. Stroh, et al Nat. Commun. 4, 2110 (2013)

[18] D.-J. Choi, S. Guissart, M. Ormaza, N. Bachellier, et al Nano. Lett. 16, 6298 (2016)

[19] P. Wahl, P. Simon, L. Diekhoner, et al Phys. Rev. Lett. 98, 056601 (2007)

[20] A. F. Otte, M. Ternes, S. Loth, C. P. Lutz, et al Phys. Rev. Lett. 103, 107203 (2009)

[21] W. Chen, T. Jamneala, V. Madhavan, et al Phys. Rev. B 60, R8529 (1999)

[22] P. W. Anderson, Phys. Rev. 79, 350 (1950)

[23] J. B. Goodenough, Phys. Rev. 117, 1442 (1960)

[24] A. Dilullo, S. Chang, N. Baadji, K. Clark, et al Nano. Lett. 12, 3174 (2012)

[25] E. J. G. Santos, D. Sanchez-portal, et al Phys. Rev. B 81, 125443 (2010)

[26] I. C. Gerber, A. V. Krasheninnikov, et al New J. Phys. 12, 113021 (2010)

[27] B. Fischer and M. W. Klein, Phys. Rev. B 11, 2025 (1975)

[28] P. Wahl, P. Simon, L. Diekhoner, et al Phys. Rev. Lett. 98, 056601 (2007)

Chapter 6

Inelastic spectroscopy of MnPc and rare-earth complex on Au(111)

In addition to probe the local density of state of adsorbate, STM has a capability to detect the excitation of molecular vibration modes by inelastic electron tunneling spectroscopy (IETS). In this Chapter, we will study the vibrational excitation related transport properties of the MnPc molecules as well as the rare-earth complexes adsorbed on Au(111) by combining the local manipulation capabilities of STM with inelastic electron tunneling spectroscopy. In these studies, STM-IETS spectroscopy will be utilized for the chemical identification as a finger print of manipulated objects in the tunneling junction.

In the first part of this Chapter, we will show how the vibration-mediated transport can be activated and controlled for the MnPc molecule on Au(111) by the STM. In the second part, we will investigate the vibration-assisted transport properties of Cerium (Ce) atoms/clusters on Au(111) in the presence of the hydrogen (H_2) molecules by exploiting the local manipulation and IETS spectroscopy capabilities of STM.

6.1 The vibration-mediated transport in a molecular junction

The molecules adsorbed on a surface interacts strongly with the substrate electronic system. Thus the strong molecule-substrate interaction may lead to modification of many intrinsic physical properties exhibited by the molecules in a solution or in the gas phase. On the other hand, the lifting-up a single molecule from the surface with a sharp tip of STM can effectively eliminate the influence of substrate on the molecule. More importantly, the STM has a capability to detect the electron transport properties of the molecule not only adsorbed on a surface, but also the one attached to the probe tip itself [1-4]. Thus the attachment of a single molecule to the probe tip of STM allows us to investigate the intrinsic electron transport through a single molecule suspended between the tip and surface. Furthermore, such a molecular junction in STM can serves as a reliable and controllable model system for studying a single molecule in a way similar to the mechanical break junctions [5-7].

6.1.1 The molecular junction in STM

Although the Kondo effect and the light gas adsorption behaviors of the MnPc molecules adsorbed on Au(111) surface has been studied by STM [8-10], the electron transport

properties of a single MnPc molecule suspended in a tunneling junction of STM has not been studied yet. Below, we will discuss a new fascinating electron transport behavior of the MnPc molecular junction. Here the MnPc molecule is suspended in the vacuum gap between a sharp tip and flat surface. It is made by the lifting-up a single MnPc molecule from Au(111) with a sharp tip of STM and stabilize it in the tunneling junction.

 The Figure 6.1(a) shows a topographic STM image of MnPc molecules on Au(111) taken with the Au covered W tip. As seen clearly from the STM image, the MnPc molecules adsorb face-on. The bright protrusion at the center of MnPc is due to the Mn d-orbital states near the Fermi level [8]. By approaching the STM tip towards a molecule on the Au(111) surface, it is possible to transfer a single MnPc molecule from the surface to the tip apex of the STM. Then the presence of molecule on the tip can be directly confirmed by the reverse transfer process through applying a voltage pulse on the tip or scanning a clean surface area with this molecule terminated-tip to drop the MnPc molecule from STM tip back to the surface. Since the voltage pulse applied on a phthalocyanines molecule have possibility to induce a chemical modification on the molecule through dehydrogenation process [9, 11-12], the second method is used in this work.
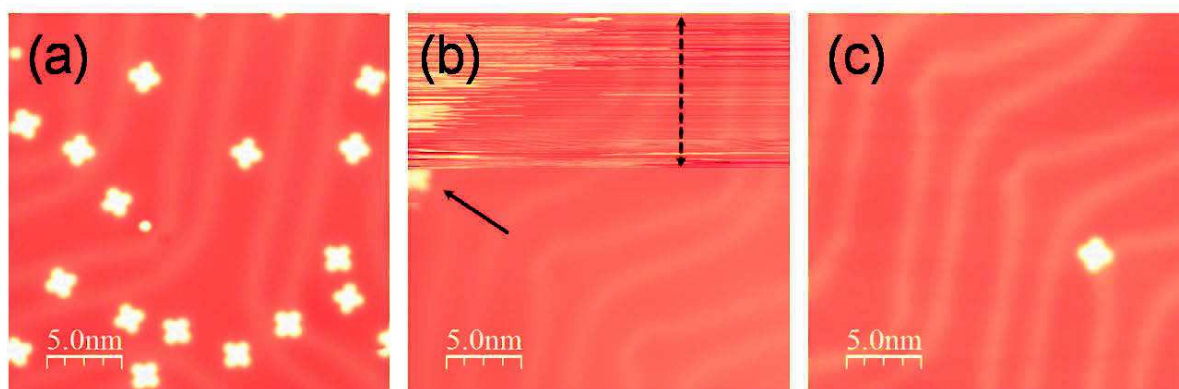

Figure 6.1 (a) STM image of MnPc molecules on Au(111) surface. (b) STM image of the bare Au(111) surface taken by the STM tip with and without MnPc molecule. A single MnPc molecule was dropped from the tip during the scanning process and adsorbed at the position indicated by the arrow. (c) STM image of MnPc molecule in (b) and the molecule found to be adsorbed at the elbow dislocation site of Au(111).

 Figure 6.1(b) shows a clean A(111) surface imaged by a STM tip with (upper part) and without (lower part) MnPc molecule. When the MnPc-terminated-tip scan over the bare Au(111) surface at a higher scanning speed, the surface looks very noisy due to the flexible and unstable motion of the molecule over the surface (see the upper part of Figure 6.1(b)). After the molecule dropped at the elbow dislocation site on Au(111) (see the molecule indicated by the arrow in Figure 6.1(b)), however, the STM image is dramatically improved and the surface reconstruction of Au(111) is clearly visible. It should be note that only one molecule is dropped from STM tip to the surface as shown in the Figure 6.1(c). Most importantly, the dropped MnPc molecule from the STM tip to the surface (see Figure 6.1(c)) exhibits the characteristic topographic and spectroscopic features of MnPc adsorbed on Au(111) surface. This implies that a single MnPc molecule was initially transferred to the tip apex of STM without inducing any destruction for the molecule.

Furthermore the reversible molecule transfer process between the tip and the surface indicates that a single MnPc molecule is attached to the STM tip apex rather than any other position on the tip. Thus it forms a molecular junction where a single MnPc molecule suspended in the tunneling junction between the sharp tip and the flat surface. As we will see in the next section, the formation of MnPc molecule junction is further verified by STM-IETS taken by the MnPc-terminated tip over the clean Au(111) surface.

6.1.2 The vibration-mediated transport in MnPc molecular junction

The different environment for MnPc on the tip hints a very different electronic behavior compared to the on-surface molecule. Therefore, we investigated the electron transport properties of MnPc molecule attached to the tip apex of STM by probing the differential conductance around the Fermi level. First, the STS spectrum of a MnPc molecule on Au(111) is taken with a bare metallic tip and used it as a reference spectrum to be compared with the STS result obtained by a MnPc-terminated tip. Then, we will discuss in more detail the IETS spectroscopic properties of MnPc molecules attached to the tip apex of STM.

The differential conductance spectrum acquired by positioning the tip over the Mn ion site of MnPc on Au(111) exhibits a pronounced step shaped feature at zero-bias (see Figure 6.2(b)). Before functionalizing with the MnPc molecule, the bare metallic tip is characterized on clean Au(111) from both topographic and spectroscopic point of view. After the attachment of a single MnPc molecule to the tip apex (see the schematic view in Figure 6.2(f)), the STM image and STS spectrum taken over the bare Au(111) surface is dramatically changed due to the presence of molecule on the tip.

As a first signature of the presence of MnPc on the tip, a bright vertical stripe, about 1.5 nm wide forms on the left-hand side of the STM image of Figure 6.2(d), the width of this stripe corresponds to the size of a single MnPc molecule. Moreover, the atomic resolution of Au(111) is obtained by dragging the MnPc molecule on the surface as can be seen on the right-hand side of Figure 6.2(d). The formation of such a topographic feature can be understood in the context of flexible motion of the molecule that follows the tip during the scanning process. Since the scan for each horizontal line is started from the left-hand side of the image, the scanning of a bare surface by the tip terminated with a flexible molecule leads to a formation of the bright stripe at the left-hand side of the STM image (see Figure 6.2(d)).
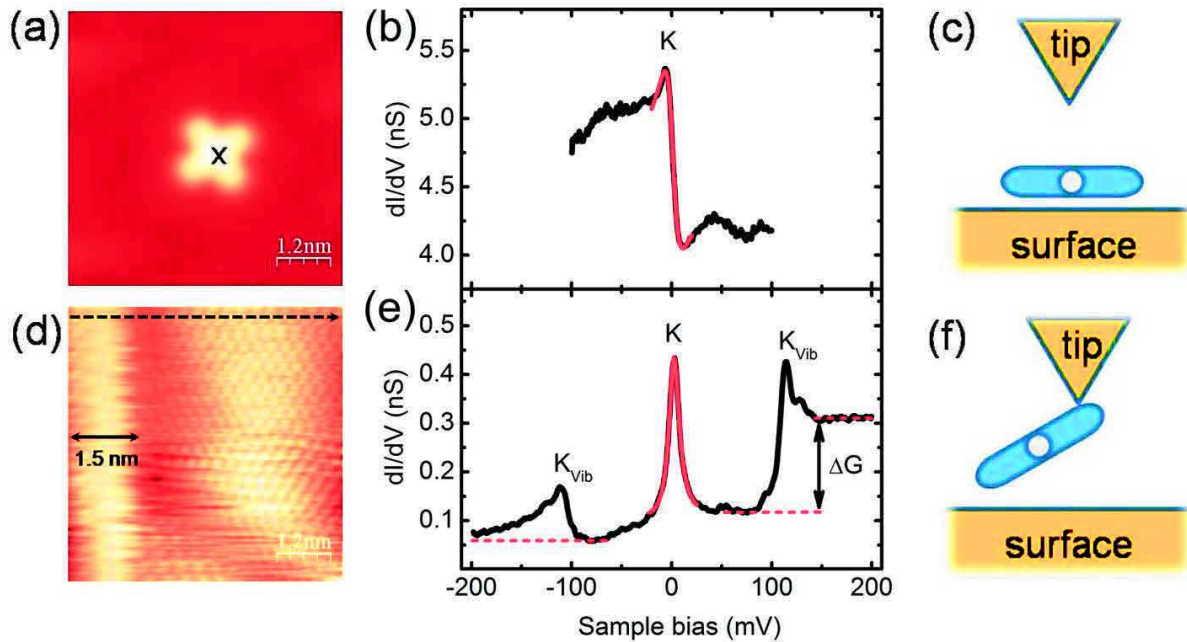
Figure 6.2 (a) STM image and (b) dI/dV spectrum of a MnPc molecule on Au(111) surface. The Kondo resonance is labeled with K. (c) Schematic view of STM junction for (a) and (b). (d) STM image and (e) dI/dV spectrum obtained with the MnPc-terminated tip over the bare Au(111) surface. The dashed black arrow and double arrow in (d) indicate the scan direction and the width of bright vertical stripe. The zero-bias Kondo resonance, vibration-mediated Kondo resonances and inelastic step in (e) are labeled as K, K_{vib} and ΔG, respectively. (f) Schematic view of the STM junction for (d) and (e), where a single molecule is attached to the tip apex.

The electron transport through a single MnPc molecule attached to the tip apex of an STM is further investigated by measuring the high-resolution inelastic electron tunneling spectroscopy (IETS) close to the Fermi level. The differential conductance (dI/dV) spectrum measured at any location over the bare Au(111) surface with a MnPc-terminated tip revealed a prominent sharp peak close to zero-bias voltage and two characteristic side peaks at the finite bias voltages of -110 ± 2 mV and 115 ± 2 mV, respectively (see Figure 6.2(e)). Another clear feature in the spectrum is a step-like increase in the dI/dV signal (labeled ΔG) at positive bias voltages. This is typical signature for an inelastic electron tunneling process involving the excitation of molecular vibration mode [13-14]. More importantly, the observed inelastic electron tunneling spectrum provides further evidence for the presence of MnPc molecule on the probe tip and hence the formation of a molecular junction [15] due to the insertion of a single MnPc molecule in the tunneling gap between the probe tip and flat surface.

Compared with the spectrum of MnPc on Au(111), there are dramatic changes in the dI/dV spectrum of the MnPc molecule attached to the tip apex of STM. As it can be seen from spectra in Figure 6.2(b) and (e), the differential conductance signal intensity is reduced by one order of magnitude for the MnPc molecule on the tip apex compared to that of the on-surface MnPc molecule. This dramatic reduction in the conductance signal might be a direct consequence of the electron transport mainly through the MnPc molecule

suspended between the probe tip and flat surface, rather than the vacuum tunneling. A similar change in the conductance signals has been observed for the CuPc molecule after introducing it into the silver break junction [16].

Interestingly, the step shaped zero-bias feature in STS spectrum of the on-surface MnPc molecule is changed into a sharp peak for the MnPc molecule attached to the tip apex (see Figure 6.2(b) and (e)). More importantly, the two side peaks and the conductance step feature observed for MnPc on the tip are completely absent for the MnPc molecule on Au(111) surface. These significant changes in dI/dV spectrum of Figure 6.2(e) must be originate from the interaction of the injected electrons with the various molecule electronic states during the tunneling process which is facilitated in the case where the MnPc molecule is suspended in the gap between the tip and the surface (see Figure 6.2(f)).

Based on the discussion in Section 3.3, the step-like feature at the Fermi level in the spectrum of the on-surface MnPc molecule (Figure 6.2(b)) can be attributed to the Kondo resonance arising from the exchange interaction between the MnPc molecular spin and the itinerant conduction electrons of Au(111) substrate. The red curve in Figure 6.2(b) is a fit to the step-like feature at E_F obtained by a single Fano function with a negative asymmetry factor $q = -1.2$ and an energy width of $\Gamma = 7.5 \pm 0.5\ \mathrm{meV}$, and yields a Kondo temperature of $T_K = \Gamma/k_B = 85 \pm 5\ K$. This value is consistent with the Kondo temperature reported in the previous STM experiments for this system [8-9].

For a single MnPc molecule attached to the probe tip (see Figure 6.2(f)), the dI/dV spectrum shows a sharp peak at the Fermi level, where a Kondo resonance is found for the on-surface MnPc molecule (see Figure 6.2(b) and (e)). Since the MnPc molecule is attached to the Au covered tip of STM, the molecule can preserve its spin moment at the Mn ion center similar to the MnPc on Au(111) surface [8-9], and then the localized spin moment of the molecule might be anti-ferromagnetically screened by the itinerant conduction electrons of the Au tip. This correlated many-body state would lead to an enhanced density of states at the Fermi level, which manifests itself as a zero-bias peak in the conductance. Thus the Kondo effect is a most possible source for the observed zero-bias sharp peak in the dI/dV spectrum of the MnPc molecule attached to the tip.

In order to extract the characteristic Kondo temperature, the sharp peak feature at E_F is fitted by a single Fano function (see the red curve in Figure 6.2(e)) having a positive asymmetry factor $q = 22.8$ and an energy width of $\Gamma = 6.1 \pm 0.2\ \mathrm{meV}$, corresponding to a Kondo temperature of $T_K = \Gamma/k_B = 70 \pm 2\ K$. Interestingly, the Kondo temperature of MnPc molecule on the tip is only slightly lower than the one for the on-surface MnPc molecules.

Even though both the tip and the surface are chemically identical, the MnPc molecules on the tip is subjected to very different electronic states compared to the on-surface molecule, and hence we expect that the MnPc on a sharp tip may exhibit different Kondo behavior. However, the similar Kondo temperatures observed in the present experiment indicates that the Kondo screening of a single MnPc molecule on the atomically sharp tip

is almost as efficient as that for the molecule adsorbed directly on the bulk Au(111) substrate. Such a similar Kondo screening of the MnPc molecule by the two different electronic systems, i.e. a bulk Au(111) substrate and a sharp Au tip, is an unusual phenomenon and was not observed in the previous experiments. On the other hand, our experimental result in Figure 6.2(e) may strongly speak in favor of a self-contained Kondo screening [17-19] in the MnPc molecule with small influence of the sharp Au tip of STM.

The increasing in the Fano factor q from -1.2 for the on-surface molecule to 22.8 for the molecule on the tip can be understood by considering the change in electron tunneling. Since the molecule is attached to the tip, the probability of electron tunneling from the STM tip into the molecule greatly increased, while tunneling into the bulk continuum states is decreased, yielding an increase of the q value [20].

For MnPc molecule on the probe tip, the two side peaks at finite bias accompanied with the zero-bias Kondo peak (see Figure 6.2(e)) can be ascribed to the vibration-assisted Kondo resonance for which the excess energy of the electrons due to a finite voltage is compensated by activating a vibration mode [16, 21-23]. In addition, based on the comparison with the previously reported STM-IETS of FePc/Ag(111) [24] and theoretically calculated vibration modes of transition-metal phthalocyanines [25-26], the two side peaks at 110 ± 2 meV and 115 ± 2 meV are easily assigned to the excitation of vibration mode that involve stretching of the Mn-N_{iso} bonds of MnPc molecule.

The conductance step ΔG at the positive bias voltages above threshold voltage of 115 ± 2 mV (see Figure 6.2(e)) corresponds to an increase in the junction conductance of ~200 %. Such a large conductance increment supports the strong electron-vibration interaction in the MnPc molecule suspended between the sharp tip and surface, similar effect has been observed for CO_2 molecule in the platinum break junction [27]. Furthermore, the spectrum of the MnPc junction shows a strong asymmetry with the polarity. At the positive bias the effect of inelastic tunneling is very large, whereas at the negative bias the vibration assisted Kondo resonance become broader and the contribution of inelastic tunneling is very weak. This asymmetry in spectrum may suggest that two different vibration assisted electron transfer processes apparently compete here, one involving a vibration-mediated Kondo effect and, the other, an inelastic tunneling through excitation of molecule vibration mode [23, 28].

6.1.3 The parameter dependence of transport in MnPc molecular junction

In order to get a better understanding of the underlying physical mechanism behind the zero-bias peak and the two satellite peaks at finite bias, we analyzed the influence of the sample temperature on the dI/dV spectrum of MnPc molecule on the tip. Figure 6.3(a) presents the dI/dV spectra measured with the MnPc molecular tip over the bare Au(111) surface when the substrate is warmed up from 4.5 K, its base temperature, to 11.5 K. These data points are presented in Figure 6.3(b)-(d). To minimize the effect background

signal, both the central zero-bias central peak and the finite-bias side peaks were normalized by their background conductance for all the spectra at each temperature.
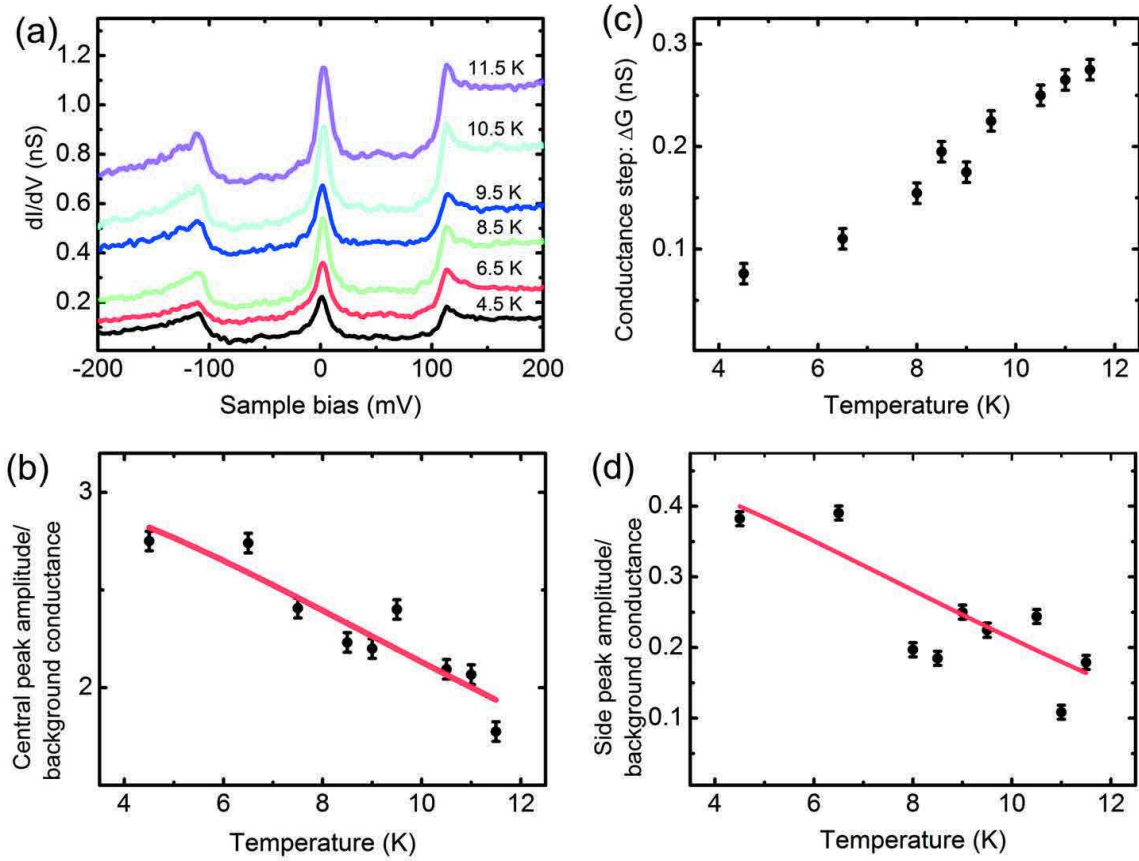

Figure 6.3 (a) dI/dV spectra taken over a bare Au(111) with a MnPc-terminated tip at the indicated temperatures. (b) The normalized conductance of the zero-bias peak and (c) the conductance step at the positive bias and (d) the normalized conductance of the positive bias peak as a function of temperature. The black dots show the experimental data. The continuous red line shows the corresponding fits to Eq(6.1).

Remarkably, the normalized conductance of both central and positive bias peaks reduces linearly as a function of sample temperature (see Figure 6.3(b) and (d)), in accordance with predictions for the Kondo effect [29]. Since the conductance data points for the negative bias peak over this temperature range shown more scattering, they are not exploited here.

The red line in Figure 6.3(b) and (d), is a linear conductance fit by means of an expression [29] :

$$G(T) = \bar{G}\left[1 + \left(\frac{T}{T_K}\right)^2 \left(2^{1/s} - 1\right)\right]^{-s} + C \tag{6.1}$$

using $s = 0.22$, and leaving T_K, $\bar{G}$ and C are free parameters.

Our experimental data are reasonably well described by this expression, and a Kondo temperature $T_K = 55 \pm 5\,K$ for the central peak and $T_K = 45 \pm 5\,K$ for the positive bias peak are extracted. Based on this fitting, the extracted Kondo temperature for the central peak is slightly lower than the one obtained from the Fano fit (see above section). This minor discrepancy might be due to the use of the oversimplified universal constant $s \cong 0.22$ which is for the spin-1/2 Kondo effect. Indeed, the MnPc molecule on the Au has a net spin higher than the spin $S = 1/2$ [8-9, 30], and hence the parameter s has a slightly different value. Nerveless, the normalized conductance of the zero-bias and satellite peaks decrease in a manner described by Eq.(6.1) which clearly indicates that the Kondo resonance is the source of the zero-bias peak. It furthermore provides a clear indication that the side peaks are related to the Kondo effect.

In order to investigate further the relation between the zero-bias peak and the satellite peaks, we focused on the evolution of differential conductance spectra as a function of tunneling gap resistance, i.e. tip-sample distance. Figure 6.4(a) and (b) presents a dI/dV spectra as a function of gap resistance.
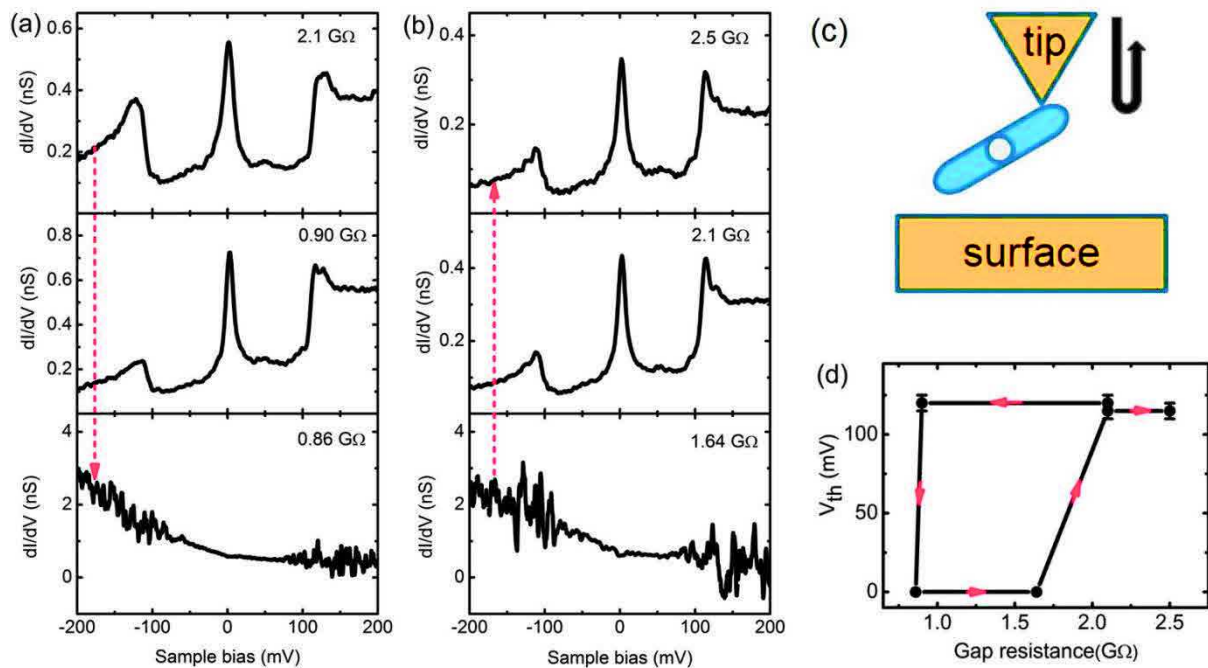

Figure 6.4 dI/dV spectrum obtained with the MnPc-terminated tip over the bare Au(111) surface when the gap resistance (a) decreased from 2.1 GΩ to 0.86 GΩ, then (b) increased from 1.64 GΩ to 2.5Ω. (c) Schematic view of the STM junction for (a) and (b), where a single molecule is attached to the tip apex. The arrow represents the changing of gap resistance. (d) The variation of satellite peak threshold voltage as a function of gap resistance in (a) and (b).

As can be seen in Figure 6.4(a), when the gap resistance is decreased from $2.1\,G\Omega$ to $0.9\,G\Omega$, the negative bias side peak is shifted from -125 mV to -115 mV and its intensity decreases significantly. This shift towards lower negative value can be ascribed to a

weakening of the molecule-tip binding. At the same time, this leads to a sharper Kondo peak by reducing the coupling of the molecular spin to the tip. On the other hand, this implies a good coupling between the Mn-N$_{iso}$ stretching mode in the MnPc molecule and the Mn d-orbital which bears the unpaired spin.

In contrast, the positive bias peak position remains the same at +125 mV and its intensity increased dramatically. Interesting, both the zero-bias and side peaks are completely and simultaneously quenched when the gap resistance is slightly decreased from $0.9\ G\Omega$ to $0.86\ G\Omega$. The disappearance of Kondo and side peaks is most probably due to a change in the configuration of MnPc molecule in the junction between the tip and surface. Simultaneously, a telegraphic noise appears in the dI/dV spectrum at bias voltages higher than the side peak threshold, which is often regarded as the signature of an unstable tunneling junction. Surprisingly both, the zero-bias Kondo peak and two side peaks appear simultaneously again when the resistance is increased to $1.64\ G\Omega$. Moreover, the two side peaks slightly shift towards lower values and located at -110 mV and 115 mV, respectively. Upon further increasing the gap resistance, both the zero-bias Kondo peak and the side peaks are relatively insensitive to the gap resistance.

As we can learn from the evolution of dI/dV spectra in Figure 6.4(a) and (b), the side peaks always appear as satellite peaks of the zero-bias Kondo peak and could not be detected in its absence. Additionally, the shift in the side peak voltage also leads to the variation of the zero-bias Kondo peak which further supports the idea that the side peaks are related to both, vibration activation and Kondo transport.

6.2 The vibration-assisted transport in rare-earth complex

 Voltage-controlled functionalities are the key features of molecular and atomic devices operating at nanometer scales. In particular, controllable hysteresis and reversible switching of the conductance in a molecular junction have been subjects of intense research efforts in molecular electronics. A number of situations, leading to switching behavior, have been evidenced by means of scanning tunneling microscope (STM)- and break-junctions (for a review see Refs. [31-32]). Well-identified mechanisms mostly deal with conformational changes induced by an electric field [33–35], charge states of molecules [36–38], and those based on proton transfer [39], while a number of other examples rely on purely interfacial phenomena. Compared to the rich work concerned with molecules, relatively few examples are available where metal atoms or ensembles of atoms are involved [40, 41].

 In this section, a tunnel junction formed by Cerium (Ce) atoms/clusters exposed to hydrogen (H_2) and enclosed between a Au(111) substrate and the Au covered W tip of the STM are investigated in ultra-high vacuum (UHV). Ce has interesting properties due to its deep 4f and outer 5d electrons that are responsible for magnetism and bonding, respectively. Its propensity to form compounds is exploited in magnetism, optics, and catalysis [42, 43]. Ce is known to form small clusters when deposited on Au(111) at room temperature, eventually forming surface alloys with Au under thermal activation [44]. However, under low temperature deposition in UHV, only isolated Ce atoms are found on the Ag(111) surface [45]. A large amount of work led to the major conclusion that the STS of clean Ce atoms on noble metal surfaces are featureless in the range ± 1 V around the Fermi level [46, 47]. Since Ce atoms are much more reactive towards residual gases, mainly H_2, than Au atoms [48], Ce atom clustering and H_2 localization is supposed to strongly compete with Ce-Au surface alloying. In situ controlling of the atomic cluster assembling by STM manipulation, therefore, opens a way for direct on-surface synthesis of objects that can serve as model systems for fundamental studies and potential technological applications.

6.2.1 Spectroscopy of Cerium atom and clusters

 To study the electronic properties of the Ce atoms by STM, a small amount of Ce was deposited from a crucible evaporator on the Au(111) surface kept at 4.6 K. Due to the low temperature deposition, the thermal diffusion of the Ce atoms was hampered, and resulted mostly in isolated atoms on the surface. As shown in the STM image of Figure 6.5 (a), the Ce atoms on Au(111) appear as protrusions with a topographical height of 1.0 Å.

 One step further, the Ce clusters (see Figure 6.5(a)–(c)) are constructed by atomic manipulation just after Ce atom deposition. The dimer is built by merging two atoms, the trimer is built from the dimer by adding a third atom to the dimer, etc. The cluster units form robust and stable entities that show a well-defined topography in the STM images

(see Figure 6.5(a)–1(c)). Spots, like the one in the upper right of Figure 6.5(a) and (b), are common on noble metal surfaces; they are due to strongly pinned defects. These defects are immobile during imaging and manipulation of Ce atoms at 4.6 K, and can play the role of a reference mark. A first set of the differential conductance (dI/dV) spectra (see Figure 6.5(d)) were collected on Ce atoms and clusters on Au(111) at 4.6 K. The dI/dV data show flat and featureless spectra over the range analyzed here (± 200 meV). This result is in agreement with previous data of Ce atoms on Ag(100) [46] and is the signature of clean Ce atoms.
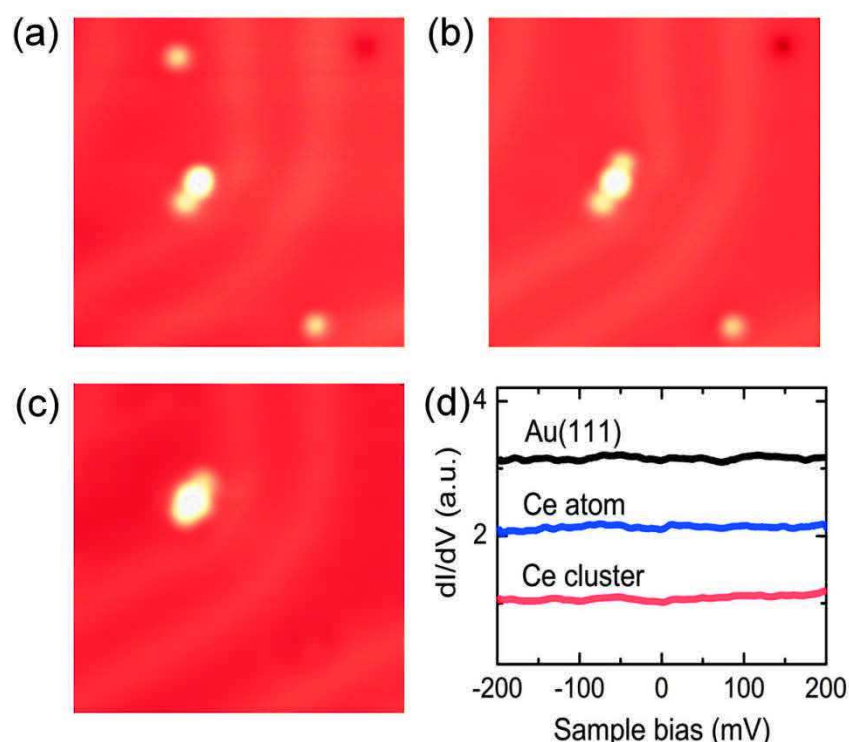
Figure 6.5 (a)–(c) STM images of the step-by-step assembling of Ce clusters by manipulation of single Ce atoms on Au(111) at 4.6 K just after Ce atom deposition, in the absence of H_2. (d) dI/dV spectra taken above the bare Au(111) surface, on a Ce atom and on top of the Ce cluster in (c).

6.2.2 Spectroscopy of Ce atoms/clusters in the H_2 environment

In the following, the natural propensity of the residual gas, mainly Hydrogen, to adsorb from the UHV vessels at low sample temperatures, was exploited. Even though our technique identifies the local fingerprint of H_2 molecules by inelastic electron tunneling spectroscopy (IETS), we cannot fully exclude the presence of other molecular species. However, H_2O and O_2 are unlikely since the system was baked at a temperature above 400 K and the sample was sputter-annealed before performing the experiment. The diffusion of light gases such as H_2 towards the object of interest—atom or defect—is further facilitated by the electric field gradient produced by the STM tip. the dI/dV spectra

recorded over the Ce atoms in the residual gas environment (Figure 6.6(c)) show mirror symmetric IETS features with a step-like increase or decrease in the conductance at a specific threshold voltage $|V_{th}| \approx 50$ mV. The spectra of Figure 6.6(c) look similar to those observed previously on various surfaces and in break junction experiments in the presence of H_2 [49–56], in which the spectroscopic features have been interpreted in terms of various inelastic effects such as vibrational and rotational excitations of the molecule on crystalline substrates [49, 53–56], sometimes leading to negative differential conductance and heating at the threshold bias [52]. In our case, the different interpretations may not be exclusive of each other since the Ce atom plays a key role in the modification of the physisorption potential between the tip and sample [57]. The dI/dV spectra taken on the Au(111) surface a few nanometers away from the atoms (see Figure 6.6(b)) are characteristic of H_2 molecules inside the tunnel junction [46, 49, 53]. In particular, it shows a threshold value V_{th}, very close to the values obtained for molecular H_2 on various surfaces including Au(111) [53], clearly validating the presence of H_2. The negative differential conductance (see Figure 6.6(b)) caused by vibrationally induced fluctuations of the H_2 molecules between two configurations in the tunneling junction is noteworthy.
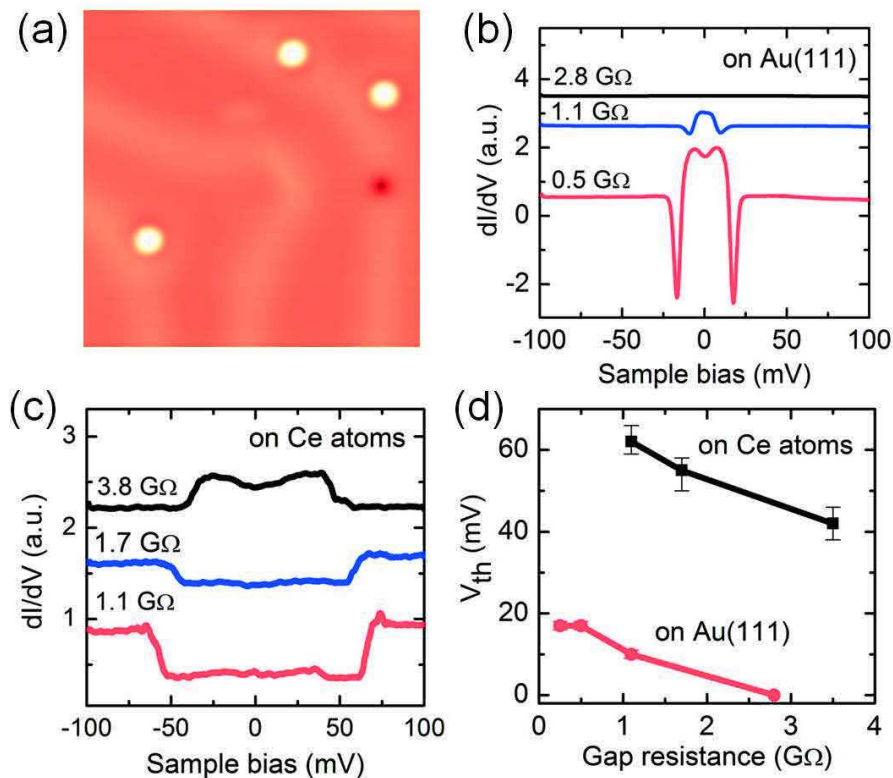

Figure 6.6 (a) STM image of Ce atoms two and three days after deposition in the presence of H_2. Each atom has a height of 1.0 Å. (b) Differential conductance spectra recorded by positioning the STM tip above the Au surface (average of ten) showing the presence of H_2 on the Au(111) surface. (c) dI/dV spectra measured above a single Ce atom with a scanning rate of 40 mV/s at different set point gap resistances (spectra vertically shifted for clarity). (d) V_{th} as a function of the gap resistance measured above the Ce atoms and on the Au surface for comparison. Error bars correspond to the scattering V_{th} over a set of different spectra.

As shown in Figure 6.6(c), single Ce atoms on Au(111) exhibit a change in the spectral features with increasing tunneling gap-resistance from 1 to 4 GΩ at a constant sample voltage, showing that the spectral details clearly depend on the tip-sample distance. The decrease of $|V_{th}|$ as a function of the gap-resistance is a significant trend as shown in Figure 6.6(d). Similar changes as a function of tip-sample distance have been repeatedly described [55]. For some atoms, a shallow upwards step is observed for positive voltages that becomes a downward step when the gap resistance is increased, clearly showing that both situations can be observed on the same atom depending on the gap resistance. As an example, Figure 6.6(c) shows the spectrum with a decrease of the conductance at $|V_{th}| \approx 50$ mV, very similar to the phonon spectra observed in the case of Au–H nanojunctions [50, 52], although the conductance values are orders of magnitude smaller than in the nanojunctions. It should be noted that no significant differences could be drawn between spectra taken for Ce atoms on hcp and fcc domains of the Au(111) surface. It is found that the spectra remain unchanged for sweeping speeds between 40 and 80 mV/s.

In the following, a further step is made by building clusters from such clearly identified Ce atoms in the presence of H_2 on Au(111), and by comparing them with clusters built from "clean" atoms (Figure 6.5). As an example, Figure 6.7 depicts the formation of a Ce dimer and trimer. Typical conditions for the lateral manipulation of atoms are a bias voltage of 0.1 V and currents up to 13 nA. Figures 6.7(a)–(c) show the different steps of the atomic manipulation leading to the formation of a compact Ce trimer. During the manipulation process, single Ce atoms closely follow the lateral motion of the STM tip. Figure 6.7(d) shows that Ce atoms keep their identity after manipulation. The corresponding topographic profiles along M and N in Figures 6.7(g) and (h), clearly show that separate atoms have a height of 1.0 Å and a lateral extension of 7.1 Å (half-width at half-maximum). The lateral manipulation of a single Ce atom in Figure 6.7(d) leads to a dimer with a slightly elongate shape (see Figure 6.7(e)). Due to the overlap of atomic orbitals, no atomic resolution of the dimer is expected. The topographic height of the dimer is 1.0 Å, and its lateral dimension (along K) corresponds to two atoms side by side separated by a distance of 2.4 ± 0.2 Å. This value is in good agreement with the nearest neighbor distance between atoms calculated for the dimer [58, 59], while the profile along the orthogonal J-direction in Figure 6.7(i) corresponds to the profile of a single atom.
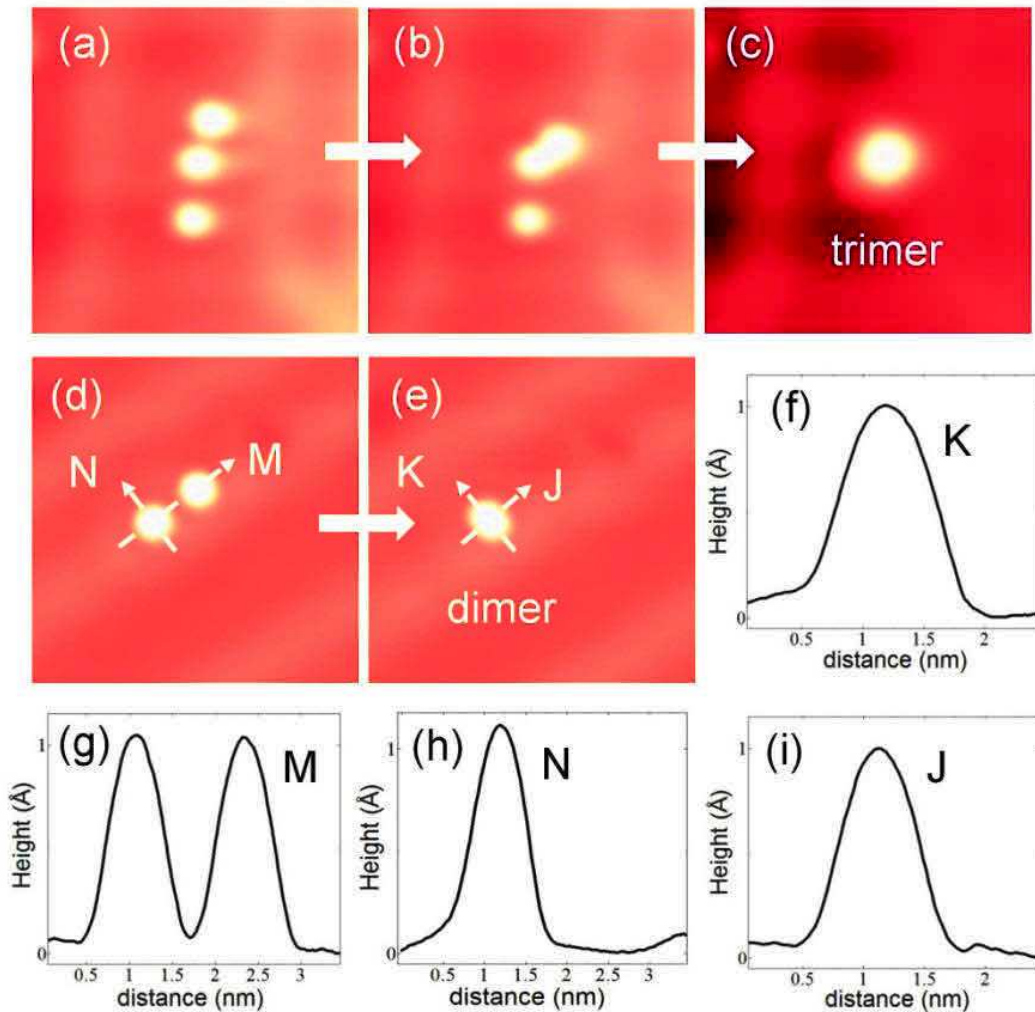
Figure 6.7 Formation of Ce clusters by atomic manipulation in the presence of H_2 on Au(111). (a)–(c) Sequence of STM images showing the formation of a Ce trimer. (d) and (e) Formation of a Ce dimer. Topographic profiles are shown for two isolated atoms: (g) along M and (h) along N. Topographic profiles are shown for the dimer, (f) along K, and (i) along J.

As shown in Figure 6.8(a) and (b), the dI/dV spectra measured above the Ce_2 and Ce_3 clusters exhibit a conductance hysteresis, accompanied by a stepwise increase or decrease of the conductance, not observed before. This hysteresis is more pronounced when the gap resistance is decreased, most probably due to effects related to charging. In the forward scan, while ramping the bias voltage up (see the black curves in Figure 6.8), a sudden drop in the conductance occurs at positive bias (~140 meV), while in the backward scan (see the blue curves), another sudden drop occurs at a negative bias (−140 meV) and the cluster is switched back to its original state. Repeated scanning always leads to the same switching voltage $|V_{th}|$, which only depends slightly on the sweeping rate. Additionally, the fine structures in Figure 6.8 are fully reproducible.

It is worth noting that the threshold voltage increases from ~50 mV for the Ce atom (see Figure 6.6(c)) to ~140 mV in Ce_2 (see Figure 6.8(a)), but remains almost the same for Ce_2

and Ce3. In all cases, the positive and negative threshold voltages are slightly asymmetric with respect to the Fermi level of the Au(111) substrate and these values slightly shift to lower voltages when the gap resistance is decreased. Submitting the clusters to voltage pulses between –1.0 and 1.0 V for 50 ms does not change the threshold value.
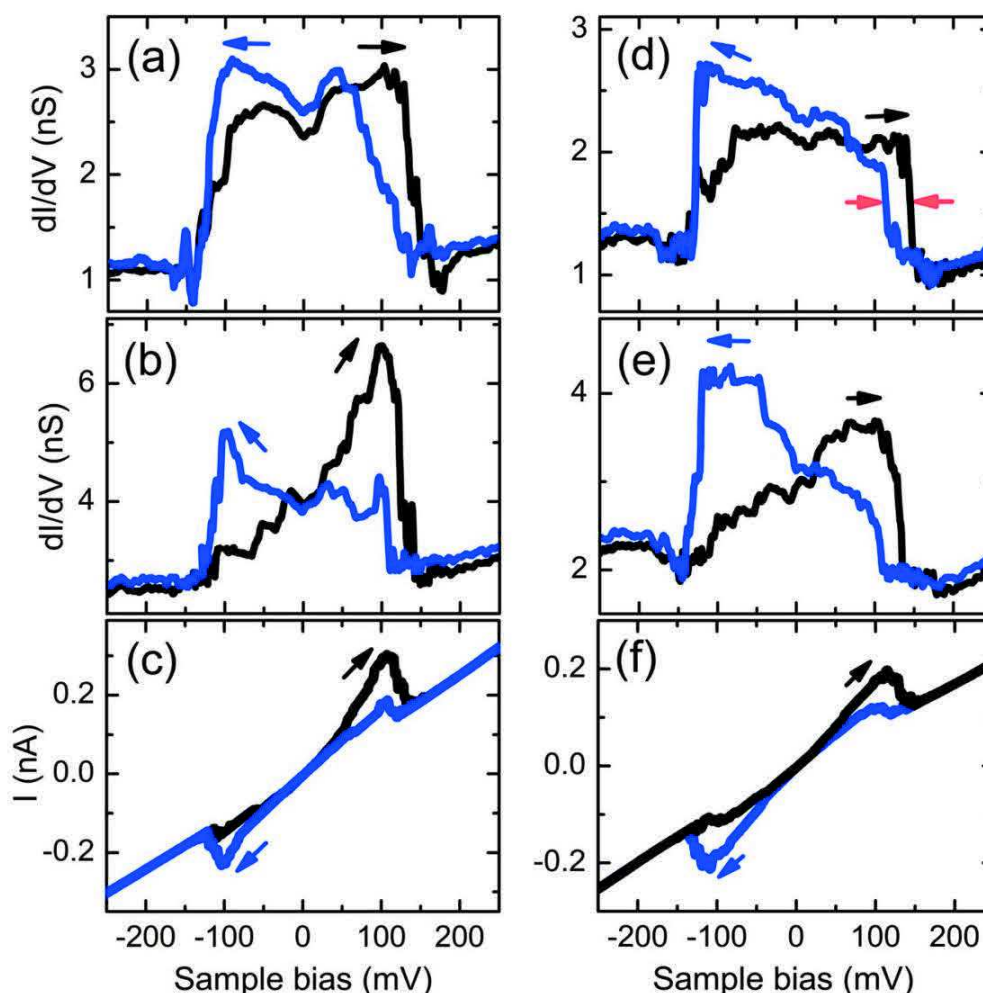

Figure 6.8 dI/dV spectra measured over the (a) and (b) Ce dimer and (d) and (e) Ce trimer formed by atomic manipulation in the presence of adsorbed H on Au(111) with different set-point gap-resistances (a) 1.5, (b) 0.7, (d) 1.7, and (e) 1 GΩ. Forward scans are indicated by the black spectra (black arrows) and backward scans are indicated by blue spectra (blue arrows). The red arrows in (d) indicate the charging energy E_{ch}. (c) and (f) are corresponding I–V curves of the dimer and the trimer, respectively. The scanning rate for all spectra is 160 mV/s. The threshold voltage at which the switching takes place, V_{th}= 140 mV, is determined by a specific inelastic mode of the pinned H2.

 In contrast, the tunneling spectra taken on the bare Au(111) surface adjacent to the Ce2 and Ce3 clusters only show the usual H2 spectra without any hysteresis. On closer inspection, the hysteresis of Figure 6.8 reveals that the onset of differential conductance at the positive bias is shifted down by about 30 mV in the backward scan (blue curve) compared to the forward scan (black curve), referring to charging effects. Even after repeated cycling, the threshold voltages remain the same to within a few meV for a given

scan speed. The conductance hysteresis indicates that both the Ce dimer and trimer switch electronically from one state to the other in the forward scan and switch back to their original state in the backward scan.

 The formation of the dimer and trimer leads to the simultaneous observation of a stiffer mode, i.e. $|V_{th}| \approx 140$ meV, in the IETS of Figure 6.8. This value, however, is much larger than the vibrational constant of a Ce dimer (in the range 26–30 meV [58, 59]), and could not explain the fact that the same value is experimentally observed for both Ce dimers and trimers. Therefore, based on the H_2 interpretation, the increase in V_{th} may be due to: (i) a confinement of the H_2 molecules by the clusters, compared with the situation of the atom, thus leading to different initial and final configurations, (ii) an increase of H_2 density on the surface as described in Ref. [49] that leads to the quenching of low frequency modes for more compact structures, and (iii) a stiffening of the phonon mode due to subsurface atomic H resulting from a molecular dissociation as observed by STS in the case of Pd substrates [60].

 Although rare-earth hydrides exhibit interesting semiconducting properties [61, 62] that could explain the charging, the third explanation must be ruled out because the splitting of the H_2 molecules needs much higher energies than the ones involved here [63]. In other words, the heating provided by inelastic electron tunneling through the H_2 molecules surrounding the junction is not sufficient to provide the necessary energy for molecular splitting (for an estimate of the heating effects see [52]). Furthermore, no evidence for subsurface H_2 has been obtained by repeated spectroscopic investigation of the Au right beside the Ce-cluster. The new features that appear in the dI/dV after cluster formation are clearly correlated to the particular status of the Ce clusters because no such behavior is observed for Ce atoms residing on the surface in the presence of H_2. Due to the strong affinity of Ce clusters for H_2, it is believed that the first two explanations hold in our case, namely an increasing H_2 surface density when approaching a Ce cluster. A similar tendency has been observed for H_2 molecules adsorbed in the vicinity of a phthalocyanine molecule on Au(111) [56]. Possible configurations of H_2 molecules closest to the Ce atoms are shown in Figure 6.9. A strengthened bonding of the molecules to the clusters is then responsible for the increased vibrational energy. Notice the compact shape for the trimer in accordance with the trimer configuration in Figure 6.7(c).
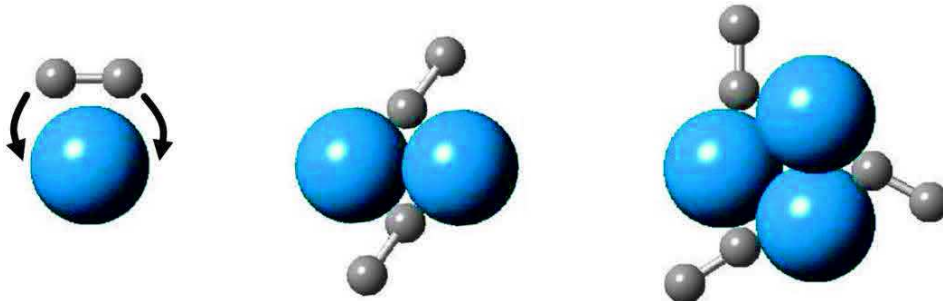

Figure 6.9 Ce atom and clusters (blue). The H_2 molecule (grey) can move freely around a Ce atom, but is pinned in a dimer and trimer.

 In addition, the large amount of H_2 molecules that can be caught per Ce atom [48] may form a cushion that decouples the clusters from the substrate. The hysteresis behavior observed in the dI/dV spectra of Figure 6.8 may then be explained by the charging of Ce clusters. This interpretation is coherent with the fact that the hysteresis associated with charging depends on the sweeping rate (see Figure 6.10). A sizable effect only appears for a sweeping rate larger than 80 mV/s. The shift between the two curves indicated by a red arrow in Figure 6.8(d) may then be an estimate for the charging energy E_{ch} = 30 meV. In this respect, the observed effect is similar to the multiple charging effect of an atom [38] or a molecule [64] deposited on an insulating layer. As a result, two combined effects drive the conductance: While the threshold value V_{th} is related to the inelastic excitation of H_2 adsorbed on Ce, the appearance of the hysteresis between the forward and the backward scan clearly refers to charging of the partly isolated Ce cluster.
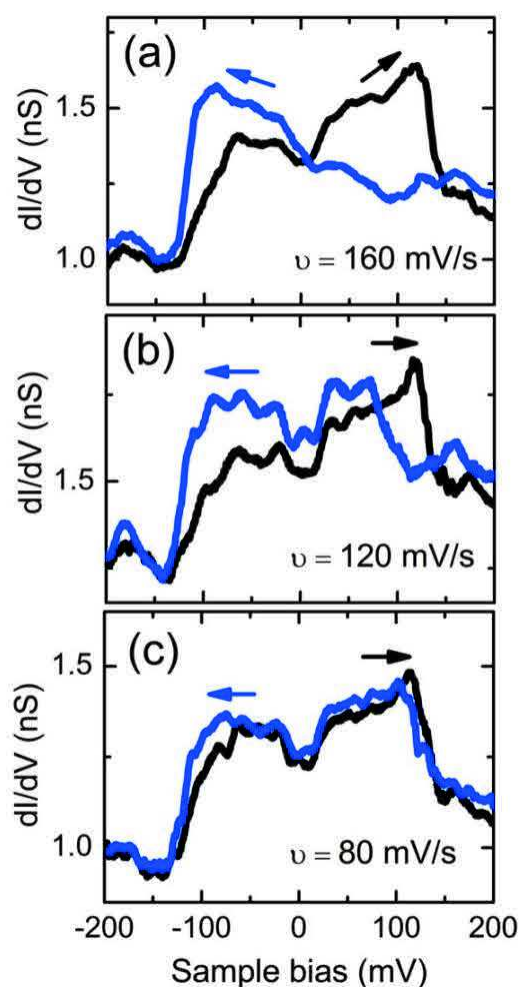

Figure 6.10 dI/dV spectra measured at a Ce dimer formed by atomic manipulation in the presence of adsorbed hydrogen on Au(111) (set-point gap-resistances 1.6 GΩ). The hysteresis is clearly visible in (a) and (b). Forward scans are indicated by the black arrows and backward scans by the blue arrows. The scanning rate decreases from (a) to (c); at 80 mV/s the forward and the backward scans almost overlap.

In conclusion, we have evidenced reproducible conductance hysteresis and voltage controlled switching of a junction made of a Ce cluster on a Au surface located directly opposite the Au tip of an STM. We demonstrated that Ce clusters can efficiently collect and pin H_2 molecules. Such H_2 decorated Ce_2 and Ce_3 clusters form new objects that behave differently from both H_2 molecules and bare Ce clusters. The conductance of the resulting objects within the STM junction is then ruled by a charging and switching determined by the specific inelastic mode of the pinned H_2. Characteristic electronic properties of an STM junction can thus be engineered in a simple way by *in situ* adjusting—by means of the STM tip—the H_2 pinning at an atomic cluster. This work can be considered as a proof-of-concept for the direct STM-assisted, on-surface manipulation and modification of objects that can serve as model systems for fundamental studies in nano-electronics.

References

[1] C.-L. Chiang, C. Xu, Z. Han and W. Ho, Science 344, 885 (2014)

[2] K. Iwata, S. Yamazaki, P. Mutombo, P. Hapala, et al Nat. Commun. 6, 7766 (2015)

[3] P. Hapala, R. Temirov, P. Jelinek, Phys. Rev. Lett. 113, 226101 (2014)

[4] P. Hapala, G. Kichin, R. Temirov, P. Jelinek, Phys. Rev. B 90, 085421 (2014)

[5] J. Park, A. N. Pasupathy, J. I. Goldsmith, C. Chang, et al. Nature. 417, 722 (2002)

[6] E. A. Osorio, K. O'Neill, M. Wegewijs, N. Stuhr-Hansen, et al. Nano. Lett. 7, 3336 (2007)

[7] L. H. Yu, Z. K. Keane, J. W. Ciszek, et al. Phys. Rev. Lett. 95, 256803 (2005)

[8] Liwei Liu, Kai Yang, Yuhang Jiang, et al Scientific Reports 3, 01210 (2013)

[9] Liwei Liu, Kai Yang, Yuhang Jiang, et al Physic. Rev. Lett. 114, 126601 (2015)

[10] Yang, K., Xiao, W., Liu, L. et al. Nano Res. 7, 79 (2014)

[11] A. Zhao, Q. Li, L. Chen, H. Xiang, W. Wang, et al. Science 309, 1542 (2005)

[12] K. Jens, K. Michael, S. Jacob, H. Pin-Jui, et al Phys. Rev. B 91, 235130 (2015)

[13] B. C. Stipe, M. A. Rezaei, W. Ho, Science 280, 1732 (1998)

[14] R. C. Jaklevic, and Lambe, Phys. Rev. Lett. 17, 1139 (1966)

[15] D. Djukic, K. S. Thygesen, K. W. Jacobsen et al Physic. Rev. B 71, 161402 (2005)

[16] D. Rakhamilevitch. R. Korytar, A. Bagrets, et al Phys. Rev. Lett. 113, 236603 (2014)

[17] C. H. Booth, M. D. Walter, M. Daniel, et al Phys. Rev. Lett. 95, 267202 (2005)

[18] B. W. Thimm, J. Kroha, J. von. Delft, Phys. Rev. Lett. 82, 2143 (1999)

[19] D. E. Liu, S. Burdin, H. U. Baranger, and D. Ullmo, Phys. Rev. B 85, 155455 (2012)

[20] M. Ternes, A. J. Heinrich, et al J. Physic. Condens. Matter 21, 053001 (2009)

[21] L. H. Yu et al Phys. Rev. Lett. 93, 266802 (2004)

[22] J. J. Parks, et al Phys. Rev. Lett. 99, 026601 (2007)

[23] I. Fernandez-Torrente, K. J. Franke, J. I. Pascual, Phys. Rev. Lett. 101, 217203 (2008)

[24] N. ohta, R. Arafune, N. Tsukahara, et al J. Phys. Chem. C 117, 21832 (2013)

[25] I. E. Brumboiu, S. Haldar, J. Luder, et al J. Chem. Theory. Comput. 12, 1772 (2016)

[26] Z. Liu. X. Zhang, Y. Zhang, J. Jiang Spectroc. Acta. Part A, 67, 1232 (2007)

[27] R. Ben-Zvi, R. Vardimon, et al ACS Nano 7, 11147 (2013)

[28] J. Paaske, K. Flensberg, Phys. Rev. Lett. 94, 176801 (2005)

[29] D. Goldhaber-Gordon, et al Phys. Rev. Lett. 81, 5225 (1998)

[30] E. Minamitani, Y. S. Fu, Q. K. Xue, Y. Kim, et al Phys. Rev. B 92, 075144 (2015).

[31] A. Troisi, M. A. Ratner, Small 2, 172 (2006)

[32] J. L. Zhang, J. Q. Zhong, J. D. Lin, W. P. Hu, et al Chem. Soc. Rev. 44, 2998 (2015).

[33] Y. F. Wang, J. Kröger, R. Berndt, W. A. Hofer, J. Am. Chem. Soc. 131, 3639 (2009).

[34] S. Weight, C. Busse, L. Petersen, E. Rauls, et al Nat. Mater. 5, 112 (2006).

[35] X. H. Qui, G. V. Nazin, W. Ho, Phys. Rev. Lett. 93, 196806 (2004).

[36] T. Leoni, O. Guillermet, H. Walch, et al Phys. Rev. Lett. 106, 216103 (2011).

[37] T. G. Gopakumar, F. Matino, et al Angew. Chem., Int. Ed. 51, 6262 (2012).

[38] S. W. Wu, N. Ogawa, G. V. Nazin, W. Ho, J. Phys. Chem. C 112, 5241 (2008).

[39] W. Auwärter, K. Seufert, F. Bischoff, D. Ecija, et al Nat. Nanotechnol. 7, 41 (2012).

[40] D. M. Eigler, C. P. Lutz, W. E. Rudge, Nature 352, 600 (1991).

[41] J. Repp, G. Meyer, F. E. Olsson, M. Person, Science 305, 493 (2004).

[42] G. F. Wang, Q. Peng, Y. D. Li, Acc. Chem. Res. 44, 322 (2011).

[43] J. A. Rodriguez, S. Ma, P. Liu, J. Hrbek, J. Evans, et al. Science 318, 1757 (2007).

[44] S. Ma, X. Zhao, J. A. Rodriguez, J. Hrbek, J. Phys. Chem. C 111, 3685 (2007).

[45] J. T. Li, W. D. Schneider, R. Berndt, B. Delley, Phys. Rev. Lett. 80, 2893 (1998).

[46] M. Pivetta, M. Ternes, F. Patthey, et al Phys. Rev. Lett. 99, 126104 (2007).

[47] W. A. Hofer, G. Teobaldi, N. Lorente, Nanotechnology 19, 305701 (2008).

[48] Z. W. Zhang, W. T. Zheng, Q. Jiang, Int. J. Hydrogen Energy 37, 5090 (2012).

[49] J. A. Gupta, C. P. Lutz, A. J. Heinrich, D. M. Eigler, Phys. Rev. B 71, 115416 (2005).

[50] W. H. A. Thijssen, D. Djukic, A. F. Otte, et al Phys. Rev. Lett. 97, 226806 (2006).

[51] O. Tal, M. Krieger, B. Leerink, et al Phys. Rev. Lett. 100, 196804 (2008).

[52] M. L. Trouwborst, E. H. Huisman, et al Phys. Rev. B 80, 081407 (2009).

[53] S. W. Li, A. Yu, F. Toledo, Z. M. Han, et al Phys. Rev. Lett. 111, 146102 (2013).

[54] F. D. Natterer, F. Patthey, H. Brune, Phys. Rev. Lett. 111, 175303 (2013).

[55] C. Lotze, M. Corso, K. J. Franke, F. von Oppen, et al <u>Science 338, 779 (2012)</u>.

[56] K. Yang, W. D. Xiao, L. W. Liu, X. M. Fei, H. Chen, et al <u>Nano Res. 7, 79 (2014)</u>.

[57] M. Stocker, S. Röger, B. Koslowski, The hydrogen molecule in a vice. 2015, arXiv:1503.07702. arXiv.org e-Print archive. http://arxiv.org/abs/1503.07702 (accessed Apr 20, 2016).

[58] X. Y. Cao, M. Dolg, <u>Mol. Phys. 101, 1967 (2003)</u>.

[59] B. O. Roos, R. Lindh, P. A. Malmqvist, et al <u>J. Phys. Chem. A 112, 11431 (2008)</u>.

[60] L. C. Fernández-Torres, E. C. H. Sykes, et al <u>J. Phys. Chem. B 110, 7380 (2006)</u>.

[61] F. J. A. den Broeder, S. J. van der Molen, M. Kremers, et al. <u>Nature 394, 656 (1998)</u>.

[62] B. R. Mehta, I. Aruna, L. K. Malhotra, Rare earth gadolinium nanoparticles for hydrogen induce. In Nano-scale Materials; Sahu, S. N.; Choudhury, R. K.; Jena, P., Eds.; Nova Science Publishers: Hauppauge, N.Y., 2006; pp 25–34.

[63] S. J. Blanksby, G. B. Ellison, <u>Acc. Chem. Res. 36, 255 (2003)</u>.

[64] F. E. Olson, S. Paavilainen, M. Persson, et al <u>Phys. Rev. Lett. 98, 176803 (2007)</u>.

Conclusion

For many technological applications, it is necessary to place the molecules on a supporting metallic surface or electrode. However, many interesting intrinsic physical properties, exhibited by the molecules in the bulk state, in a solution or in the gas phase, may be modified by the molecule-substrate interaction. Therefore, understanding the interaction of molecules with metal substrates as well as with other molecules is crucial to controlling the physical properties of molecules, and tailoring the novel functionality towards organic molecular electronic devices.

The results presented in this thesis work provide a comprehensive overview of the influence of molecule-substrate and molecule-molecule interactions on the electronic and magnetic properties of the metal phthalocyanine molecules, i.e. the metal-organic complexes consisting of an organic ligand and a central transition metal ion, adsorbed on metal substrates. The model systems what we investigated here are the manganese-phthalocyanine (MnPc) and copper-phthalocyanine (CuPc) molecules adsorbed on Ag(111) and Au(111) surfaces. The scanning tunneling microscopy and spectroscopy (STM/STS) investigations on these systems allowed us to understand the effect of substrate reactivity, molecule-substrate and molecule-molecule interactions on the electronic, magnetic and vibrational properties of the molecule.

In the Chapter 3, we demonstrated the adsorption configurations, the electronic and magnetic properties of MnPc and CuPc molecules adsorbed on Ag(111) by means of the high spatial and energy resolution STM/STS measurements. In the first part we showed that both MnPc and CuPc molecules adsorb with the molecular plane parallel to the surface and their molecular axes are aligned along $[10\bar{1}]$ and $[1\bar{2}1]$ surface directions of the Ag(111) substrate. In particular, the high spatial resolution STM measurements allowed us to identify precisely the adsorption site of molecules: Mn ion of MnPc molecule reside on top site, while the Cu ion of CuPc is located on a hollow site of the Ag(111) surface. The observed adsorption configuration of MnPc on Ag(111) was fully confirmed with the density functional theory (DFT) calculations by our collaborators. In the second part, we demonstrated that the Kondo resonance is localized over the central Mn ion in MnPc, whereas in CuPc at monoatomic step the Kondo resonance is shown on the Pc ligand of molecule. Thus, their Kondo behavior allowed us to draw a conclusion that the magnetism in MnPc arises from a localized spin in the Mn 3d-orbital, whereas the magnetism in CuPc arising from the delocalized spin in the π-orbital of Pc ligands. Additionally, we showed that the presence of magnetic spin moments in the Pc ligand as well as in the central Cu ion of CuPc leads to the creation of a triplet (S=1) ground state through an intra-molecular exchange coupling of the ligand π-spin with the d-spin of Cu ion.

In the Chapter 4 we presented a detailed investigation for the growth mechanism of bilayer MnPc molecules on Ag(111) substrate, and we studied systematically the influence

of molecule-substrate and molecule-molecule interactions on the electronic and magnetic properties of MnPc molecules as the first-time observation in experiment.

In the first part, we showed the three distinct adsorption configurations for the isolated MnPc molecules in the second layer, i.e. the on-top, shifted and bridge-like configurations, by the high spatial resolution STM topography measurements. The on-top configuration is characterized by the adsorption of a second-layer MnPc molecule on top of the first layer MnPc and rotated by 45° relative to the first layer. In the shifted case, the second layer MnPc is laterally shifted and its central Mn ion is sitting above the nitrogen atom of a first layer MnPc. In the bridge configuration, the second layer MnPc molecule adsorbed at a site between two molecules in the first layer and thus formed a bridge. While the in-plane molecular axes are rotated by 30° relative to the first layer MnPc molecule. Furthermore we showed that the growth mechanism of second layer self-assembled islands of MnPc molecules are dominated by the molecule-molecule interactions, as the interaction with underlying Ag(111) substrate becomes screened by the first monolayer. This mechanism is further evidenced by a complex evolution of the electronic structure towards the semiconducting behavior. The inter-molecule interactions lead to formation of a metastable self-assembled islands of second layer MnPc molecules with the parallel adsorption configuration. While a subsequent thermal annealing at temperature of about 100°C leads to formation of a more stable second layer island with the non-planar molecular adsorption and a varying phase shift of the second layer molecules with respect to the first layer. The tilted and phase modulated adsorption configuration of MnPc molecules inside the second layer island is a direct consequence of the temperature induced enhancement of inter-molecule interactions.

In the second part, by probing the Kondo effect using STM with high spatial/energy resolution, the influence of the molecule adsorption site on the Kondo resonance was investigated: the Kondo temperature increased from T_K = 75 ± 2 K to 105 ± 3 K and 140 ± 5 K when going from the on-top, to the bridge and shifted configurations for the isolated MnPc molecules in the second layer. More importantly, the trend in the variation of Kondo temperature in agreement with the previously calculated anti-ferromagnetic (AFM) exchange coupling constants for the bilayer MnPc molecules : $J_{on\text{-}top} > J_{bridge} > J_{shifted}$ which follows the inverse law. One of the central findings in this thesis work is that the Kondo effect and the inter-layer AFM exchange coupling are competing with each other in the bilayer MnPc/Ag(111) system: the stronger the exchange coupling the lower the Kondo temperature.

The studies on the influence of molecule-molecule interaction on the Kondo behavior was second topic in the Chapter 4. For the MnPc molecules inside second layer island we found that the Kondo behavior is strongly affected by neighboring molecules, as evidenced by a complex evolution of the zero-bias Kondo peak. In contrast to the isolated MnPc, the inter-layer as well as intra-layer molecule-molecule magnetic interactions led to a change in the Kondo resonance of MnPc molecule inside the second layer island. Thus we found an oscillating behavior of the Kondo temperature for the MnPc molecules

inside the second layer island as a result of a changing of the AFM exchange coupling strength induced by the phase modulation.

In the Chapter 5 we explored the possibilities of manipulating the magnetism of MnPc molecule by doping with Co atom. We observed that the interaction of Co atom with MnPc molecules smoothly modify its local environment and tune the Kondo behavior. More importantly, we observed an evidence of the AFM exchange coupling between the magnetic moments of the Co atom and MnPc molecule.

In the Chapter 6 we studied the vibrational excitations of MnPc molecule as well as the rare-earth complex on Au(111) by exploiting the local manipulation and the inelastic electron tunneling spectroscopy (IETS) capabilities of STM. In these studies, the STM-IETS spectra were utilized for the chemical identification as a finger print of molecules inside the tunneling junction. In the first part, using STM-IETS spectroscopy we demonstrated that both zero-bias Kondo resonance and vibration-mediated Kondo resonance at finite bias were became active for the MnPc molecule trapped in a STM tunnel junction. This observation is quite in contrast to the case of MnPc on Au(111) where the zero-bias Kondo channel is only active one. In the second part, we observed that the Cerium (Ce) clusters on Au(111) can efficiently collects and pins the hydrogen (H_2) molecules by using STM-IETS spectroscopy. In particular we demonstrated the conductance of resulting rare-earth complexes was ruled by a charging and switching which is crucially determined by the specific inelastic mode of the pinned hydrogen (H_2) molecules.

Overall, these findings in this thesis work could be an important step in understanding the electronic, magnetic and vibrational structures of the metal-phthalocyanine molecules on metal surfaces. Particularly the systematic step by step investigation of MnPc from a single molecule up to the ordered bilayer structure allowed us to shed light on the evolution of its electronic and magnetic structures. In addition the locally manipulated metal-organic complexes on surface allowed us to control the junction conductance by simply changing the gap resistance. This type of control could be a step ahead for the future applications metal-organic complexes in the nano-electronic devices.

Acknowledgement

Tuerhong ROUZHAJI

**Effet de l'environnement sur les propriétés
électroniques et magnétiques de complexes de métaux
de transition et de terres rares**

ECOLE DOCTORALE
pcp

UNIVERSITÉ DE STRASBOURG

Résumé

Cette thèse présente les résultats de mesures expérimentales effectués à basse température par les techniques de microscopie tunnel à balayage et de spectroscopie par tunnel à balayage (STS) sur les métaux de transitions phthalocyanines déposées sur les surfaces de métaux nobles. Les mesures STM/STS ont été effectuées pour les molécules MnPc et CuPc adsorbées sur les surfaces Ag (111) et Au (111) à la température expérimentale de travail de 4,5 K. Ces deux types de molécules présentent une différence substantielle de configurations d'adsorption, des comportements électroniques et magnétiques et des structures vibratoires moléculaire. Les études STM/STS ont principalement porté sur les propriétés magnétiques de ces molécules à travers l'effet Kondo et une attention particulière a été accordée à la molécule de MnPc en raison de son comportement magnétique plus intéressant issu de l'atome Mn central. Particulièrement, nous avons étudié l'évolution spectrale des structures électroniques et magnétiques du MnPc partant d'une molécule unique jusqu'à la structure bicouche ordonnée sur la surface Ag (111). En outre, les études STM/STS ont montré une preuve de couplage magnétique entre les moments magnétiques de l'atome de Co et de la molécule de MnPc ainsi que sa forte dépendance vis-à-vis du site d'adsorption de l'atome de Co. Ces études STM/STS sur ce système nous ont permis de comprendre l'effet des interactions molécule-substrat, molécule-molécule et molécules-atome sur les propriétés électroniques et magnétiques des molécules de MnPc.

Mots clés : Effet Kondo, métaux de transitions phthalocyanines, microscopie tunnel à balayage et spectroscopie tunnel, couplage magnétique

Résumé en anglais

This thesis presents the results of low-temperature scanning tunneling microscopy (STM) and scanning tunneling spectroscopy (STS) studies on transition-metal phthalocyanines molecules on the noble metal surfaces. The STM/STS measurements have been performed for MnPc and CuPc molecules adsorbed on Ag(111) and Au(111) surfaces at the experimental working temperature of 4.5 K. These two types of molecules exhibit substantially different adsorption configurations, the electronic and magnetic behaviors and the molecule vibrational structures. The STM/STS studies have focused mainly on the magnetic properties of these molecules by means of Kondo effect, and special attention has been paid to MnPc molecule due to its more interesting magnetic behavior arising from the central Mn atom. Particularly we investigated the spectral evolution of electronic and magnetic structures of MnPc starting from a single molecule up to the ordered bilayer structures on Ag(111) surface. In addition, the STM/STS investigations showed an evidence of magnetic coupling between the magnetic moments of the Co atom and MnPc molecule and its strong dependence on the adsorption site of Co atom. These STM/STS investigations on this system allowed us to understand the effect of molecule-substrate, molecule-molecule and molecule-atom interactions on the electronic and magnetic properties of MnPc molecules.

Keywords : Kondo effect, transition metal phthalocyanines, scanning tunneling microscopy and spectroscopy, magnetic coupling